

EFFECTS OF STRETCHING ON FLEXIBLE ORGANIC ELECTRONIC STRUCTURES

OYEWOLE OLUWASEUN KEHINDE

A THESIS SUBMITTED

FOR THE DEGREE OF MASTER OF SCIENCE

DEPARTMENT OF THEORETICAL PHYSICS

AFRICAN UNIVERSITY OF SCIENCE AND TECHNOLOGY, ABUJA

DECEMBER, 2011

ACKNOWLEDGEMENTS

May all glory, honour, and adoration be unto God, the creator of the universe. My acknowledgements to God is not only because He granted me favour to be admitted to AUST but also stood by me till the point of writing M Sc thesis. He is the beginning and the ending of my programme here at AUST. When things were too tough, He fought for me that I might stay till the end of the programme. Who am I not to give thanks unto Him for unmerited blessings He has endowed me. May He reigns forever in my life.

I would like to express my deepest appreciation to my supervisor, Prof. Wole Soboyejo, for his enthusiastic supervision of my thesis. He is the Angel that God has sent to me to make my dream comes true. He made everything possible for me to do experimental work in spite that my programme is theoretical. May Almighty God continue to be with you and your family.

My unending gratitude goes to my Late father, Mr. Samuel O. Oyewole and my sweet mother, Mrs. Mary A. Oyewole, for their care, advice, and prayers in my life. I would also like to appreciate my siblings: Dele, Tope, Gbemi, Kemi, Taiwo-my twin sister, Idowu, and Alaba, for their support.

I am indebted to Dr. M. G. Zebaze Kana, and the entire staff of Advanced Physics Laboratory, Sheda Science and Technology Complex, for giving me an opportunity to work with them in their Laboratory. I would also like to say a million thanks to Dr. Sola Odusanya of Advanced Biotechnology Laboratory,

Sheda Science and Technology Complex for his advice. I cannot but say thanks to Engineer Gadu of gamma Irradiation Facilities, NAEC, for his support. My mind will not be at rest if I failed to thank Tiffany Tong, Princeton University, for ensuring that I have results of adhesion tests that are relevant to my work. May God richly bless you.

My stay in AUST community would not be great without friends, AUST staff, and AUST professors. You guys have blessed me throughout of my stay in AUST. May Almighty God bless all of you in return. My special acknowledgements go to all my class mates: Juliet, Musty, Bayo, Isaiah, Emaka, Timothy, Gabin, Yahaya, Speed, Edmond, and my class and room mate, Joseph. I cannot forget your immense contributions to my life. I would also like to show my gratitude to members of my prayer group: Niyi, Buchi, Tunde, Johnson, and Chinedu, for their spiritual support.

Finally, my appreciation goes to my God sent Angel, Deborah, for her bountiful cares. You did not only rescue me at the critical time when my thesis needed tools to progress but also stay by me in your Laboratory for my success. I will never forget your presence in my life.

TABLE OF CONTENTS

Acknowledgements.....	i-ii
Table of Contents.....	ii-iv
Abstract.....	vii
List of Tables.....	viii
List of Figures.....	ix-x
 Chapter 1 Introduction	1
1.1 Introduction.....	1-2
1.2 Aims and Objectives of the Thesis.....	2-3
1.3 Outline of the Thesis.....	4
1.4 References.....	5
 Chapter 2 Basic Theory and Literature Review.....	6
2.1 Silicon-Based Solar Cells.....	6-7
2.2 Organic Solar Cells.....	8-10
2.2.1 Operation of organic Solar Cells.....	11
2.2.1.1 Absorption of Light.....	12
2.2.1.2 Generation and Separation of Charge Carriers.....	12
2.2.1.3 Selective Transport of the Charge Carriers Through the Bulk of the Device to the Appropriate Collection at the Electrodes.....	13
2.2.2 Advantages of Organic Solar Cells.....	14
2.2.3 Disadvantages of Organic Solar Cells.....	14

2.3 Characterization of Solar Cells.....	14-16
2.4 Characteristics Parameters of Silicon Solar Cells.....	17
2.4.1 Open Circuit Voltage.....	17-18
2.4.2 Short Circuit Current.....	18-19
2.4.3 Maximum Power.....	19
2.4.4 Fill Factor.....	19-21
2.4.5 Power Conversion Efficiency.....	21
2.5 Stretchable Organic Solar Cells.....	22-24
2.6 Review of Theory of Adhesion Between two Surfaces in Contact.....	24
2.6.1 Adhesion Force Measurements.....	24-27
2.6.2 Adhesion Energy.....	27
2.6.3 Adhesion Models.....	27-28
2.6.3.1 Hertzian Model.....	28-33
2.6.3.2 Johnson-Kendall-Roberts (JKR) Model.....	33-37
2.6.3.3 Derjerguin-Muller-Toporov (DMT) Model.....	37-38
2.6.3.4 Maugis-Dugdale (MD) Model.....	38-40
2.7 References.....	41-43

Chapter 3 Modelling of Adhesion Effects on Contact Lengths and Deformations Induced on the Interfaces of Organic Electronic Structures.....44

3.1 Introduction.....	44-45
3.2 Measurement of Adhesion Energy.....	46-47
3.3 Modelling of Adhesion Effects on Contact Lengths.....	47-51
3.4 Estimation of Residual Stresses, Mechanical Stresses and Crack Driving Forces.....	51

3.4.1 Residual Stresses.....	51-55
3.4.2 Mechanical Stresses.....	55-58
3.4.3 Crack Driving Forces.....	58-60
3.5 Results and Discussion.....	60
3.5.1 Results of Analytical Modelling.....	60-66
3.5.2 Finite Element Analysis of Contact Around Dust Particles.....	66-70
3.5.3 Finite Element Simulations of Stretching of Thin Film Layers of Stretchable Organic Solar Cells.....	70-75
3.5.4 Crack Driving Forces.....	75-80
3.6 Conclusions.....	80
3.7 References.....	81-82
Chapter 4 Experimental Study of Effects of Stretching on the Optical Properties and Mechanical Failure of Layers of Flexible Organic Solar Cells.....	83
4.1 Introduction.....	83
4.2 Fabrication of Stretchable Solar Cells.....	84
4.2.1 fabrication of PDMS Substrates.....	85
4.2.2 Deposition of ITO on PDMS Substrates.....	86
4.2.3 Deposition of Thin Film Layer of PEDOT:PSS on Glass Slide and on ITO-coated PDMS.....	88-89
4.2.4 Deposition of Thin Film Layer of P3HT:PCBM on PEDOT:PSS/ITO/PDMS.....	89-90
4.2.5 Vacuum Thermal Deposition of Al Cathode.....	90-91
4.3 Materials Characterization.....	91
4.3.1 Measurement of Stress-strain.....	92-94
4.3.2 Surface Morphology.....	94-95

4.3.3 Measurement of Optical Properties.....	95
4.4 Results and Discussion.....	95
4.4.1 Stress Analysis.....	95-97
4.4.2 Optical Properties.....	98-104
4.4.3 Surface Morphology of As-fabricated Layered Structures.....	104-107
4.4.4 Change in Grain Structures of the Layers of the Structures....	107-110
4.4.5 Interfacial Adhesion Forces and Energies.....	110-111
Chapter 5 Conclusion.....	112
5.1 Summary and Concluding Remarks.....	112-113
5.2 Future Work.....	113

ABSTRACT

This work presents the responses of optical properties and mechanical failure of layers of stretchable organic electronic structures under tension using analytical, simulations, and experimental techniques. The interfacial contact around dust particles was modelled. The deformation induced during stretching was also modelled before simulating the stress distributions and calculating the crack driving forces of the layers using finite element analysis. The finite element simulation of adhesion and contact around dust particle was done to fully understand the effects of adhesion on contact length of a two-layer structure. To understand how these structures behave under service condition, a stretchable organic electronic was fabricated. Each of the fabricated layers was fully characterized to know how their optical property and grain structure are being affected under monotonic loading. The adhesion forces and values of surface roughness of the layered structures were also measured using atomic force microscopy (AFM). The adhesion forces were incorporated into developed models along with their material properties, in order to calculate their interfacial adhesion energies. The results obtained are, therefore, summarized.

LIST OF TABLES

Table 2.1: Summary of Hertz, JKR, DMT, and MD Models

Table 3.1: Properties of the Materials Used for the Modelling

Table 3.2: Summary of the Energy Release Rate for Each of the Crack Length

Table 4.1: ITO Sputtering Parameters

Table 4.2: Values of RMS Roughness of ITO on Various Surfaces

Table 4.3: Comparison of Interfacial Adhesion Forces of the Layered Structure

Table 4.4: Comparison of Interfacial Adhesion Energies of the Layered Structures

LIST OF FIGURES

Figure 2.1: Schematic of a Silicon-Based Solar Cell

Figure 2.2: A Bulk heterojunction Solar Cell

Figure 2.3: Schematic of Organic Solar Cell Operation

Figure 2.4: Schematic of Solar Cell Characterization Set-Up

Figure 2.5: A Typical I-V Curves of a Solar Cell

(a) In the Dark

(b) Under Illumination of Photons

Figure 2.6: Schematic of I-V Curves for

(a) a Bad Solar Cell

(b) a Good Solar Cell

Figure 2.7: Layered Structures of a Flexible Organic Solar Cell

Figure 2.8: Chemical Structure of (a) P3HT (b) PEDOT (c) PSS and (d) PCBM

Figure 2.9: Schematic of Force-Displacement Curve Depicting the Various Stages [(A)-(E)] of Cantilever-Surface Engagement

Figure 2.10: The Contact Between Two Elastic Surfaces Both in the Presence (Contact Radius, a_0) and Absence (Contact Radius, a_1) of the Surface Forces:

(a) Contact between AFM Tip and Substrates

(b) Distribution of Stresses in Contacting Surfaces, and

(C) Force-Displacement Relation for Contacting Surfaces

Figure 2.11: Force (per unit area) – Distance Relation for Dugdale Model

Figure 3.1: Comparison of Adhesion Energies of Layers of a Typical Organic Solar Cell

Figure 3.2: Schematic of Deposition of a Film on a Dust Particle:

(a) the Particle Settled on Layer 2 Before Deposition

(b) During Deposition of Layer 1 with Uniform Pressure

(c) After Deposition of Layer 1

Figure 3.3: Schematic of Axisymmetric Model of Contact Around Dust Particles

Figure 3.4: Schematic of Organic Electronic Structure Under Tensile Force

Figure 3.5: A Simple Model of Crack Propagation in:

- (a) a Thin Film on PDMS and
- (b) a Quarter of the Deposited Thin Film

Figure 3.6: (a) Void Lengths as Functions of Heights of Dust Particles of various of Various Layers Layers of a Typical Organic Electronics

(b) Contact Length Versus Height of Dust Particles of Various Layers

(c) Void Length Versus Young's Modulus

(d) Contact Length Versus Young's Modulus

(e) Void Length as a Function of Adhesion Energy for various Layers

(f) Contact Length as a Function of Adhesion Energy for Various Layers

Figure 3.7: Finite Element Simulations of Contact around Different Sizes of Dust Particles Sandwiched between P3HT:PCBM:PEDOT:PSS

(a) Mesh Plot, (b) Height is $0.02\mu\text{m}$, (c) height is $0.022\mu\text{m}$, (d) Height is $0.023\mu\text{m}$, and (e) height is $0.024\mu\text{m}$

Figure 3.8: Variation of ration L_c/L as a Function of Young's Modulus

Figure 3.9: Variation of L_c/L as a Function of Interfacial Adhesion energy

Figure 3.10: (a'-e') Mesh Plots of Interfaces of a Typical Organic Solar Cell

(a - e) Distribution of Stress Within the Interfaces of a Typical Organic Solar Cell

Figure 3.11: Energy Release Rate Versus Crack Length and Stress Distribution as the Crack Penetrate across ITO Layer

Figure 3.12: Energy Release Rate Versus Crack Length and Stress Distribution as the Crack Penetrate across PEDOT:PSS Layer

Figure 3.13: Energy Release Rate Versus Crack Length and Stress Distribution as Cracks Penetrate across P3HT:PCBM Layer

Figure 3.14: Energy Release Rate Versus Crack Length and Stress Distribution as Cracks Penetrate across Al Layer

CHAPTER 1

1.1 INTRODUCTION

In recent years, there has been increasing interest in the use of solar energy in several applications where stretchability, ductility, weight, cost and durability are priorities [1]. Some of these applications include solar panels which, in many cases, require stretching. There is also a vision of solar cells integrated into electronic textiles [2] that are stretchable and energy harvesting devices, that are drapable over the roof tops of houses [3, 4]. Since such solar cells can be subjected to stress, there is a need to develop a basic understanding of the effects of stress on stretchable solar cells.

In the case of silicon based solar cells, stretchable and bendable solar cells have been fabricated by the clever use of mechanics concepts [5-8]. However, such systems are limited by the brittleness of silicon. The relatively high cost of silicon based photovoltaics is also a major obstacle to their widespread application.

In contrast, organic solar cells offer potentially lower cost alternatives to silicon based solar cells. However, such systems typically have lower efficiencies (typically less than 8%) than crystalline silicon solar cells, although the efficiencies of the best organic solar cells are now comparable to those of

amorphous solar cells. The adhesion between stretchable polymeric substrates and organic solar cells has also been difficult to engineer. There is, therefore, a need to engineer solar cells that can adhere well to flexible substrates without failing under applied loads or deformation.

1.2 AIMS AND OBJECTIVES OF THE THESIS

The objective of this thesis is to design and fabricate stretchable organic solar cells that can adhere well to poly(dimethyl-siloxane) (PDMS) substrates. Indium tin oxide (ITO) anodic layers will be magnetron sputtered onto these substrates before introducing the organic solar cells via spin coating, evaporation and lamination. The thesis will explore the effects of stress on optical properties and failure mechanism of the layers of stretchable organic solar cells. The optical property and surface morphology of the layered structures will be characterized along with their interfacial adhesion characteristics. The effects of stretching to the optical property of the layered structures of the flexible organic electronics will be explored as well the change in the grain structures of the layers.

This research will be carried out in the following stages.

- Modelling of adhesion as a function of contact length around dust particles
- Mechanical modelling of damage in the stretched layered structure of stretchable organic solar cells.

- Simulations of contact around dust particles
- Simulations of stretching and crack driving forces of the layered structures
- The molding of poly(dimethyl-siloxane) (PDMS) using a Slygard 184 silicon elastomer base and a Slygard 184 elastomer curing agent.
- Tensile experiments to measure the stress-strain behaviour of PDMS cured under different conditions.
- The deposition of indium tin oxide (ITO) onto PDMS using the magnetron sputtering technique.
- The characterization of the surface roughness of PDMS, ITO-coated using atomic force microscopy and profilometry.
- The deposition of organic solar cells onto the ITO-coated PDMS, and ITO-coated glass which will be studied as a control.
- The study of interfacial adhesion of the layered structures.
- Study the effect of monotonic stretching on optical property and mechanical failure of stretchable organic solar cells.
- SEM and optical characterization of damage in the stretched and unstretched layers of organic solar cells.

1.3 OUTLINE OF THE THESIS

Following the introduction (Chapter 1), a detailed theory and literature review is presented in chapter 2. This will include an overview of prior work on flexible substrates, coating techniques, and characterization of flexible solar cells. Prior work on the adhesion and stretching of flexible electronics will also be reviewed along with the underlying mechanics and physics concepts. This will be followed by chapter 3 in which modelling of adhesion effects on contact length and deformation-induced at the interfaces of the layered structures of organic electronics will be presented. Experimental study of effects of stretching on organic electronic structures will be described in chapter 4. These will include the techniques for device fabrication and characterization, as well as the effects of stretching on optical properties and failure mechanisms of the layered structures. The models in chapter 3 will be used to explain the results as well. Salient conclusions arising from this study will be presented in chapter 5 along with the suggestions for future work.

1.4 REFERENCES

- [1] M. Pagliaro, C. Palmisano, and R. Ciriminna, *Flexible Solar Cells*, (2008), 1-20
- [2] A. Rohatgi, *NREL 15th Workshop on Crystalline Silicon Solar Cells and Modules* (2005) 11-12
- [3] J. Weiss, P. Kukuri, J. Chiguma, J. Gendon, B. Arfaei, P. Borgesen, and W. Jones, *Fabrication of low cost flexible solar using solution-based coating techniques*, *Global Solar Technology* (2011) 10-15
- [4] G. Dennler, C. Lungenschimied, H. Neugebauer, and N. S. Sariciftci, *J. Matter. Res.*, Vol. 20, No. 12, (2005)
- [5] S. K. Hau, H.-L. Yip, J. Zou, A.K.Y. Jen: *Indium tin oxide-free semi-transparent inverted polymer solar cells using conducting polymer as both bottom and top electrodes*, *Organ Electron.* 10 (2009) 1401-1407.
- [6] B. Winther-Jensen, F.C. Krebs: *High-conductivity large-area semi-transparent electrodes for polymer photovoltaics by silk screen printing and vapour-phase deposition*, *Sol. Energy Mater. Sol. Cells* 90 (2006) 123-132.
- [7] E. Ahlswede, W. Muhleisen, M.W.b.M. Wahi, J. Hanisch, M. Powalla: *Highly efficient organic solar cells with printable low-cost transparent contacts*, *Appl. Phys. Lett.* 92 (2008) 143307.
- [8] Y.-M. Chang, L. Wang, W.-F. Su: *Polymer solar cells with poly(3, 4-ethylenedioxythiophene) as transparent anode*, *Organ. Electron.* 9 (2008) 968-973.

CHAPTER 2

2.0 BASIC THEORY AND LITERATURE REVIEW

2.1 SILICON-BASED SOLAR CELLS

The fabrication of solar cells that is based on the technology of crystalline silicon is increasing. The pioneering work by Albert Einstein (in 1905) [1] on the photoelectric effect provided the fundamental basis for the development of solar cells. Subsequent works by Shockley et al [2] resulted in the development of transistor that provided the basis for silicon microelectronics. The silicon-based photovoltaics is based largely on the p- and n-doped silicon that are arranged into p-n junctions that are connected in series and parallel. Further technologies of thin-film silicon-based solar cells have been explored in literatures [3, 56, 57].

Silicon-based solar cells are the current building block in photovoltaics [4]. They are from silicon wafers whose surfaces have been treated to maximize light absorption. Whenever radiation from sun hits a silicon solar cell, it generates current. Silicon solar cells are based on p-n junction that produces electron in the p-type region and holes in the n-type region. This lowers the potential energy

barrier at the junction. Hence, a current flows and establishes an external potential.

The current produced by a solar cell is too low for most applications. Therefore, many cells are connected in series-parallel to produce a module with a substantial output. A schematic of a silicon solar cell is presented below in Figure 2.1. The mobilities of silicon-based solar cells are greater than those of organic solar cells counterparts. Hence, the power conversion efficiencies of silicon-based solar cells are very high. However, the cost of silicon-based solar cells is relatively high (between \$1-50 per watt) for the people in the rural/urban areas of developing world.

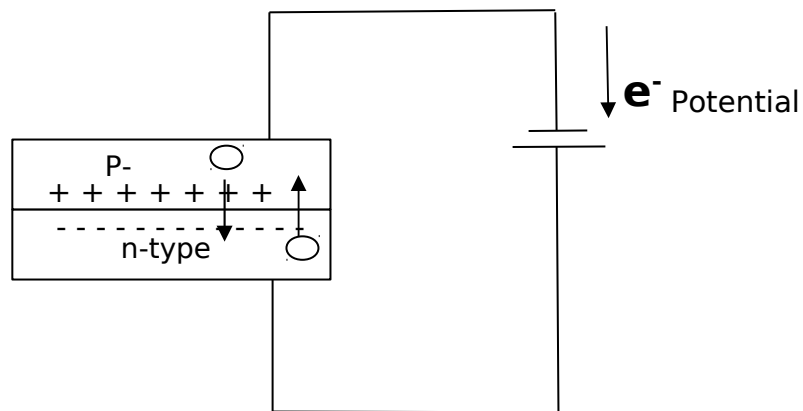


Figure 2.1: Schematic of a Silicon-Based Solar Cell

2.2 ORGANIC SOLAR CELLS

Although most of the photovoltaic devices that have been manufactured for the use by consumers use pure silicon, the high cost of silicon has limited the impact of photovoltaic devices in the world's energy generation [54]. The cost of manufacturing silicon solar cells is also too high for their proper diffusion in the rural/urban setting of developing world. In an effort to reduce the cost of silicon solar cells, alternative materials other than pure silicon are needed. The use of organic materials, as replacements for silicon, has significantly paved way for the commercial manufacture of low cost solar cells.

Organic semiconductor materials are regarded to have relatively strong absorption coefficients (more than 10^5 cm^{-1}) [5]. They have low mobilities, but their mobilities are partly balanced by their strong absorption coefficients [54]. In most of organic solar cells, the materials are holes conductors and have optical band gap of about 2 eV which is considerably greater than that of silicon-based solar cells. This limits the energy harvesting capabilities from the solar spectrum [6]. However, solar cells that are made of the organic semiconductors materials offer great possibilities of producing energy at an affordable cost.

In an effort to reduce the manufacturing cost of solar cells, there has been a tremendous research on organic solar cells within the last three decades [7-15]. The first organic solar cells were actually based on active layer that is made of a single material sandwiched between two electrodes of different work functions [16]. The introduction of a double-layer structure of two organic

semiconductor materials with different electron affinity by Tang (in 1986) is regarded as a breakthrough in the history of organic solar cells [6]. The second layer was a quantum leap (atomic electron transition) in terms of power conversion efficiency. These organic bilayer solar cells introduced by Tang [6] were made of conjugated small molecules, and achieved a low power conversion efficiency of about 1% [6]. The major limiting factor in this concept is that the thickness of the absorbing materials is much more than the diffusion length of the excitons (bound electron-hole pairs) [17]. In the real sense, for achieving high power conversion efficiency, the layer thickness of the absorbing materials has to be of the same order of the absorbing length.

The introduction of bulk heterojunction solar cells by Yu et al., in 1995 [17] has tremendously improved the manufacturing of organic solar cells. The interface between donor and acceptor materials is spatially distributed as both components inter-penetrate one another. The concept of bulk heterojunction solar cells is implemented by spin coating a polymer fullerene blend [18]. Presently, by using novel materials as well as additives optimizing the phase separation, solution processed poly(thiophene-fullerene) bulk heterojunction solar cells can achieve between 6-8% [18] power conversion efficiency.

Generally speaking, organic solar cells consist of organic materials that are sandwiched between two electrodes (an anode and a cathode). One of the electrodes is a transparent conducting oxide (the anode) while the other is a non-transparent Aluminium cathode. The sandwiched organic materials in the bulk

heterojunction solar cells consist typically of poly(3,4-ethylene-dioxylthiophene):poly(styrene-sulfonate) (PEDOT:PSS); poly(3-hexylthiophene) (P3HT) as the donor and fullerene derivative (6,6)-phenyl C₆₁-butyric acid methyl ester) (PCMB) as the acceptor. This bulk heterojunction system, P3HT:PCMB, is one of the most successful electron donor/acceptor combinations in terms of efficiency and long term stability [19]. It has dominated organic solar cells research for the past 5 years [20]. A schematic of bulk heterojunction solar cells is presented below in Figure 2.2. The organic solar cells are usually fabricated on brittle/glass substrates. However, they can also be fabricated on flexible substrates. When they are fabricated on flexible substrates, they are called flexible solar cells.

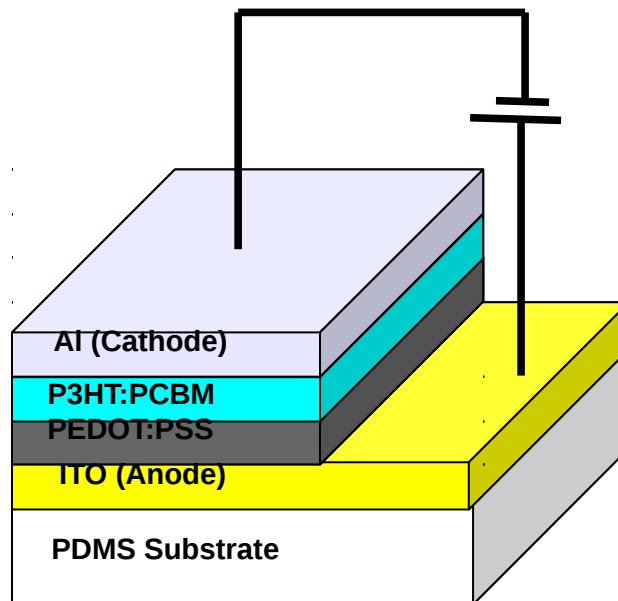


Figure 2.2 : Bulk heterojunction solar Cell

2.2.1 Operation of Organic Solar Cells

Compared to silicon-based solar cells, organic solar cells have a lower dielectric constant and a larger exciton binding energy. Hence, dissociation into free charge carriers does not occur at room temperature. In this respect, organic solar cells usually utilize two different materials called donor and acceptor materials that are sandwiched around the active material. Whenever the photovoltaic layer of organic solar cells absorbs sunlight, excitons (Coulombic bound electron-hole pairs) are created. These excitons are then dissociated into free charges, only at electron donor/acceptor interface. This occurs by rapid electron transfer between donor and acceptor materials [19, 21].

The operation of organic solar cells can be understood by considering the following three essential steps:

- the absorption of light
- the generation and separation of carrier charges and
- the selective transport of the carrier charges through the bulk of the device to the appropriate collecting electrodes

2.2.1.1 Absorption of Light

Whenever the photoactive layers of organic solar cells absorb light, electrons move from the highest occupied molecular orbital (HOMO) to the lowest unoccupied molecular orbital (LUMO) of the donor material. For the efficient collection of photons from sunlight, the absorption spectrum of the photoactive organic layer should match the solar emission spectrum. The layer should also be sufficiently thick to absorb the entire incident light.

2.2.1.2 Generation and Separation of Charge Carriers

Charge carrier creation is one of the major steps in organic solar cells in which light energy is converted to electrical energy. These charge carriers (electron-hole pairs) are photogenerated through the dissociation of excitons at electron donor/acceptor by electron transfer between the donor and acceptor of a photoactive layer, with the aid of additional input energy of an absorbed photon. The photogenerated carriers are then separated as holes diffused towards the positive large work function Φ_{anode} electrode, while the electrons diffuse towards the negative small work function $\Phi_{cathode}$ electrode without recombination. Charge carrier recombination is one of the major factors that limits the power conversion efficiency of organic solar cells.

2.2.1.3 Selective Transport of the Charge Carriers Through the Bulk of the Device to the Appropriate Collection at the Electrodes

This step is simply the collection of charge carriers at the electrodes. Yu et al. [18] have suggested that an ideal ohmic contact would be established for efficient carriers collection at the electrodes, when the acceptor LUMO level matches the Fermi level of the small work function electrode, and the donor HOMO matches the Fermi level of the large work function electrode. The charge carriers are collected at the electrodes through an external circuit. However, it is generally believed that there is always a carrier-collection loss at the electrodes, which is a major contributing factor for the low power conversion efficiency of organic solar cells. A schematic of the operation of organic solar cells is shown below in Figure 2.3.

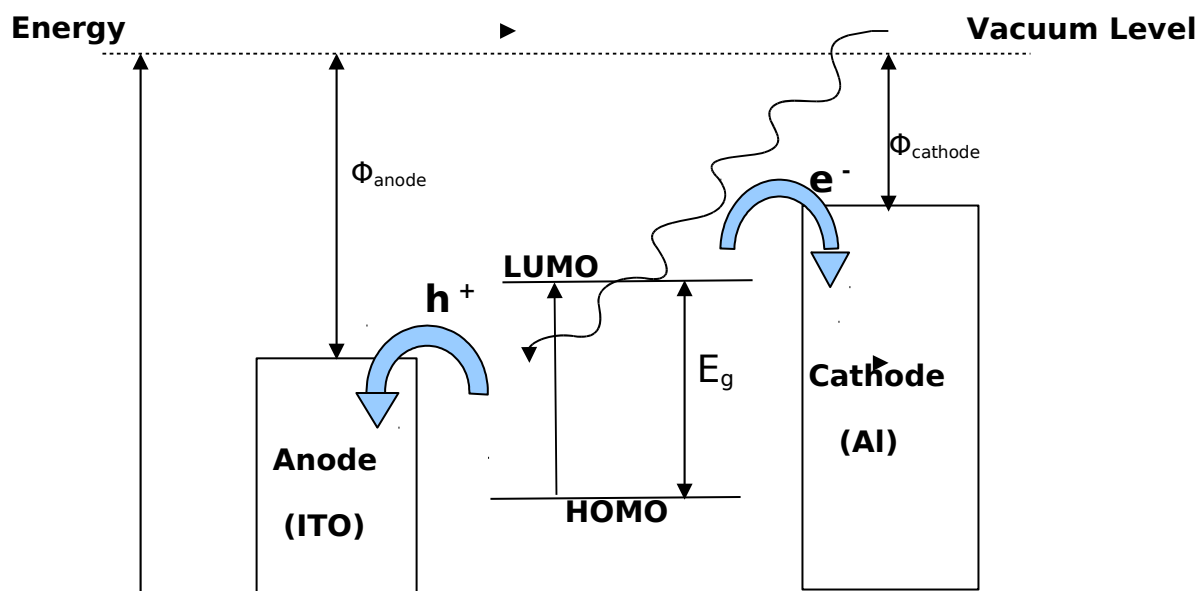


Figure 2.3: Schematic of Organic Solar Cell Operation

2.2.2 Advantages of Organic Solar Cells

The potential advantages of organic solar cells include the following:

- they would be relatively cheap to produce
- they can be fabricated on flexible substrates
- they can be shaped to suit architectural applications and
- the materials for organic solar cells can be tailored for specific applications

2.2.3 Disadvantages of Organic Solar Cells

Organic solar cells have the following disadvantages:

- the power conversion efficiencies of organic solar cells are still considerably lower than those crystalline solar cells and
- the lifetimes of organic solar cells are limited compared with those of silicon-based solar cells.

2.3 CHARACTERIZATION OF SOLAR CELLS

The current-voltage (I-V) characteristics of solar cells are usually used to characterize their performance. The following are the most essential manufacturing parameters of solar cells:

- open circuit voltage (V_{oc})
- short circuit current (I_{sc})
- maximum power (P_{max})
- fill factor (FF)
- power conversion efficiency (η)

The following equipments are usually used for characterization of solar cells:

- a source measure unit (SMU)
- a general purpose interface box (GPIB)
- a computer with graphical software (e. g Labtracer) and
- a solar simulator

Figure 2.4 below is the schematic of a set-up for solar cell characterization. A source measure unit (SMU) is usually programmed to source voltage while the current is measured and vice versa. The characterization is in the dark when solar simulator is switched off while it is under illumination of photon when the solar simulator is switched on. Solar cells behave like perfect diodes when they are characterized in the dark. The I-V curve is the forward bias curve of a diode. However, they have different curves when illuminated by photons. A typical I-V curves obtained for a bulk heterojunction solar cell is shown below in Figure 2.5

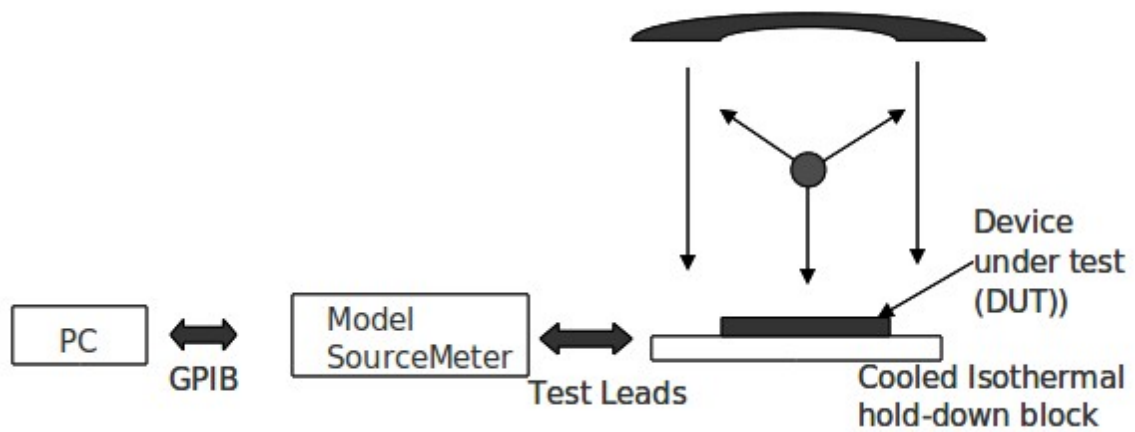


Figure 2.4: Schematic of Solar Cell Characterization Set-Up

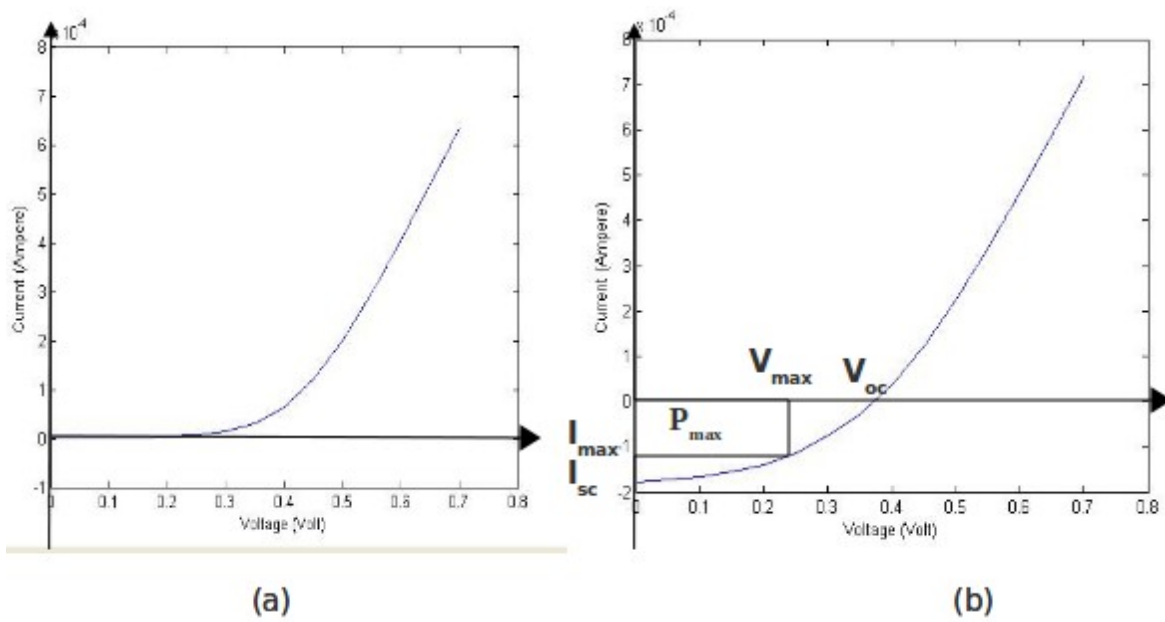


Figure 2.5: Typical I-V Curves of a Solar Cell (a) in the Dark and (b) under Illumination of Photons

2.4 CHARACTERISTICS PARAMETERS OF SOLAR CELLS

2.4.1 Open Circuit Voltage (V_{oc})

In silicon-based solar cells, the current density, J_L , under photon illumination is given by [30]:

$$J_L = J_s \left(e^{qV/nKT} - 1 \right) - J_{ph} \quad 2.1$$

where J_s is the saturation current density, V is the applied voltage, q is the elementary charge, T is the temperature, K is Boltzmann's constant, n is the ideality factor and J_{ph} is the photogenerated current density. For an ideal silicon-based solar cell, $J_{ph} = J_{sc}$ at the applied voltage. Open circuit voltage occurs when $J_L = 0$ or $I_L = 0$. By solving equation (2.1) using the fact that $J_L = 0$ or $I_L = 0$, the open circuit voltage is given by:

$$V_{oc} = \left(\frac{nKT}{q} \right) \ln \left(\frac{J_L}{J_s} + 1 \right) \quad 2.2$$

where $\frac{J_{sc}}{J_s} = \frac{I_{sc}}{I_s}$, I_{sc} is the short circuit current, and I_s is the saturation current.

According to Kostar et al. [23], the open circuit voltage of organic solar cells is given by:

$$V_{oc} = \frac{E_g}{q} - \frac{KT}{q} \ln \left[\frac{(1-P)\gamma N_c^2}{P G_b} \right] \quad 2.3$$

where E_g is the energy gap, N_c is the effective density of states, G_b is the generation rate of the bound electron-hole pairs, P is the dissociation probability of a bound electron-hole pairs into charge carriers, and γ is the Langevin recombination constant. The energy gap is the energy difference between the highest occupied molecular orbital HOMO level of the donor and the lowest unoccupied molecular orbital LUMO level of the acceptor [32].

2.4.2 Short Circuit Current (I_{sc})

The current generated by a solar cell is a function of the number of photogenerated charges that are collected at the electrodes. In silicon-based solar cells, a short circuit current occurs when the voltage applied tends to zero. For an ideal silicon-based solar cell, when $V = 0$ in equation (2.1), then the maximum current is the total photogenerated current. This is given by:

$$J_{ph} = J_{sc} = J_{max} = J_L$$

or

2.4

$$I_{ph} = I_{sc} = I_{max} = I_L$$

However, in organic solar cells, the short circuit current is the product of the photo-induced charge carrier density and the charge carrier mobility [33]. This is possible if the organic solar cells are ideal and have loss free contact. The short circuit current is given by:

$$I_{sc} = ne\mu E$$

2.5

where n is the density of charge carrier, e is the elementary charge, μ is the mobility, and E is the electric field. The photogenerated current depends on the absorbed photons [24]. It is, therefore, a key parameter for efficient charge collection of organic solar cells.

2.4.3 Maximum Power (P_{max})

Maximum power of solar cells occurs on the “knee” of the I-V curve. At the “knee”, current and voltage are referred to as maximum current and maximum voltage respectively. As shown in Figure 2.6a and 2.6b, the maximum power is the area of the rectangle, which is simply the product of the maximum current and the maximum voltage and it is given by:

$$P_{max} = V_{max} \times I_{max}$$

2.6

2.4.4 Fill Factor (FF)

The Fill Factor is essentially a characteristic parameter of solar cells. From Figure 2.6, knowing values of the maximum power, the open circuit voltage, and the short circuit current of a solar cell, the Fill factor is thus calculated as:

$$FF = \frac{P_{max}}{V_{oc} \times I_{sc}} = \frac{V_{max} \times I_{max}}{V_{oc} \times I_{sc}} \quad 2.7$$

Fill factor is generally used to determine if a solar cell is good or not, To understand how fill factor is used to characterize solar cells, we consider two I-V curves of bad and good solar cells in Figure 2.6 below.

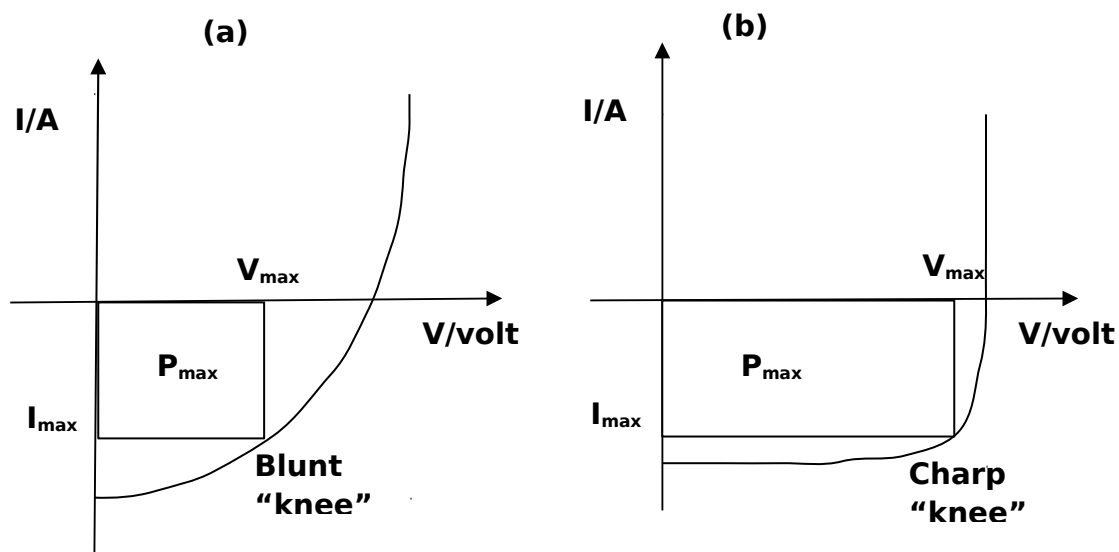


Figure 2.6: Schematic of I-V Curves for: (a) a Bad Solar Cell and (b) a Good Solar Cell

Basically, the fill factors of bad solar cells are very small (in most cases, they cannot be approximated to 1.0) due to their small maximum power. However, as shown in Figure 2.6b, good solar cells usually have bigger maximum power (P_{max}). The fill factor of good solar can be approximated to 1.0

The Fill factor of organic solar cells depends primarily on the charge dissociation, the charge carrier transport, the recombination processes, the

thickness of the active layer, and the morphology of the cathode/polymer interface [25]. The fill factor can be maximized by increasing the mobility of charges and preventing recombination of electron-hole pairs by increasing the lifetime of exciting [26].

2.4.5 Power Conversion Efficiency (η)

The power conversion efficiency of solar cells is defined as the ratio of the output power to the input power.

$$\eta = \frac{P_{out}}{P_i} \quad 2.8$$

$$P_{max} = P_{max} = V_{max} \times I_{max} = V_{oc} \times I_{sc} \times FF$$

$$\eta = \frac{V_{oc} \times I_{sc} \times FF}{P_i} \quad 2.9$$

where P_{out} is the output power and P_i is the input power

The power conversion coefficient of a solar cell is measured simply by characterizing the device. From the I-V curve, the maximum voltage and maximum current are deduced. The power generated by solar simulator, the maximum voltage, and maximum current can then plug into equation 2.8 to calculate the power conversion efficiency.

2.5 STRETCHABLE ORGANIC SOLAR CELLS

In an effort to develop more robust solar cells that can deform by stretching or bending, significant efforts have been made to deposit solar cells on flexible substrates [27-36]. Krebs et al. [27,31] have fabricated modules from PET-ITO/ZnO nanoparticles/PCMB:P3HT/PEDOT:PSS/Ag cells (Figure 2.7) using a roll-to-roll process [32]. They have also achieved power conversion efficiencies (PCE) of 2.33% from a working area of 4.8 cm². Flexible inverted polymer solar cells containing ZnO nanoparticles as an electron collection layer [32, 33] or CsCO₃ as a buffer layer [34] have been reported by other research groups. Chu et al. [35] have fabricated flexible dye-sensitized solar cells (DSSC) based on vertical ZnO nanowire arrays. They used peel-off technique to transfer vertically aligned ZnO nanowire arrays onto ITO-coated poly(ethylene-terephthalate) (PET) substrates. They then assembled bendable ZnO nanowire-based DSSCs, following polymer packaging with nanowires as electrodes.

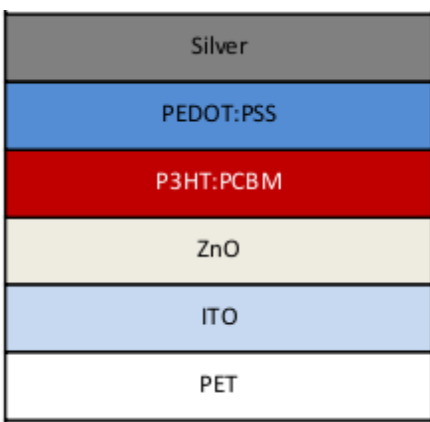


Figure 2.7: Layered Structure of a Flexible Organic Solar Cell

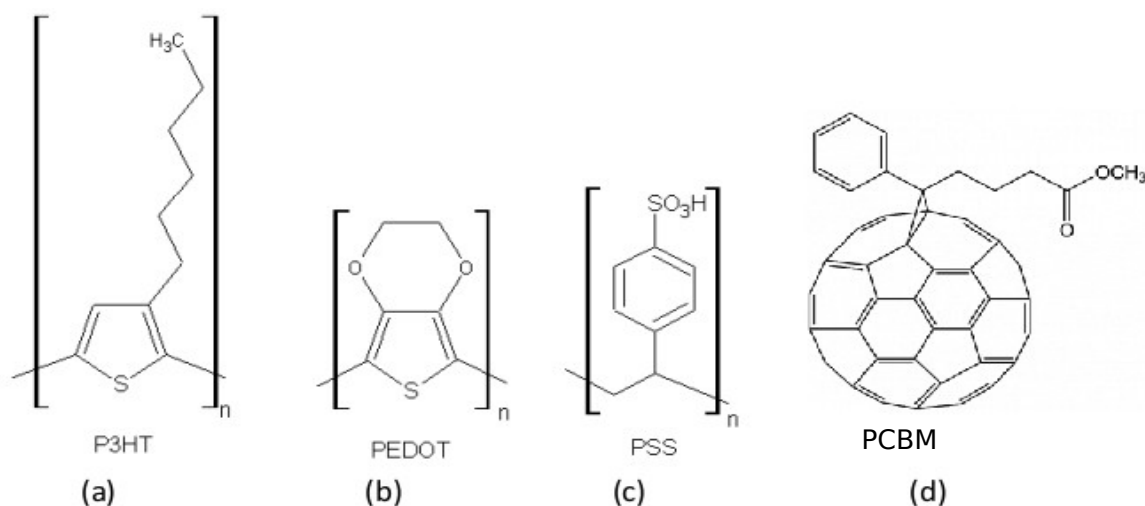


Figure 2.8: Chemical Structure of (a) P3HT, (b) PEDOT, (c) PSS, and (d) PCBM

In 2004, Aernouts et al. [37] replaced the anodic transparent indium tin oxide of organic bulk donor/acceptor heterojunction solar cells with organic alternative in the form of a highly conductive poly(3,4-ethylene-dioxythiophene):poly(styrene-sulphonate) (PEDOT:PSS). In an effort for them to improve the conductivity of PEDOT:PSS, they introduced an underlying metallic silver-grid. The chemical structure of P3HT, PSS, PEDOT and PCBM are shown above in Figure 2.8. Between 2006 and 2011, there has been further intensive investigations and reports on replacement of ITO by highly conductive PEDOT:PSS [55-57],[38,39]. Stephenie et al [40] have studied the electrical properties of stretchable gold films and shown that gold films can function as interconnects for power and signal to a fully elastic thin film transistor inverter. The experimental investigations of the elastic-plastic deformation behaviour and

cracking of nano/micro thick conducting metal on PDMS substrates have also been carried out in literature [41, 42].

The fabrication of stretchable solar cells requires good adhesion between thin film solar cells and their flexible substrates. Delamination, adhesion failure, flaking, buckling, mechanical failure and contamination by diffusion of impurities (from the substrate) may occur in these structures due to residual stresses or deformation. Hodges et al [43] have studied the adhesion of a flexible substrate Cadmium Telluride (CdTe) thin film solar cells. In their work, adhesion was studied by the analysis of foil substrates effects, surface roughness, stress, microstructure and the coefficient of thermal expansion mismatch between the substrate and the film layer. Tong et al. [44] have also presented atomic force microscopy (AFM) measurements of the adhesion between layers that are relevant to organic electronic structures (OPV cells and OLEDs). In 2010, Akogwu et al. [45] presented the results of an experimental study of the effects of cyclic damage and adhesion on Au thin films deposited on a flexible PDMS substrate.

2.6 REVIEW OF THEORY OF ADHESION BETWEEN TWO SURFACES IN CONTACT

Since adhesion between layers is crucial for the effective performance of organic electronic structures, a solid fundamental understanding of adhesion theories is helpful as a precursor to the study of the role of adhesion in stretchable organic electronic structures. This will be presented here along with a

review of the atomic force microscopy (AFM) technique that can be used to measure adhesion.

2.6.1 Adhesion Force Measurement

The Adhesion force is of a significant interest in the fabrication of organic solar cells. Since the contacts between layers can affect the degradation and efficiencies of organic solar cells, there is a need to measure the adhesion between layers that are relevant to organic solar cells. The contact mode of atomic force microscopy (AFM) is generally used to measure the adhesion force between two surfaces.

First, the tip is displaced towards the substrate of the bi-material pair. The tip then jumps to contact with the substrate when adhesive interactions are experienced. The tip is bent under elastic deformation as both surfaces remain in contact. The tip displacement is reversed but residual adhesion interactions still keep the tip in contact with the substrate even at zero loads until a negative force (pull off force), which eventually overcome the adhesion, is experienced. These various steps have been explained in literature [36, 44]. These steps are illustrated schematically below in Figure 2.9.

According to Hooke's law, the applied force is directly proportional to the displacement provided that the elastic limit is not exceeded. Hence, the adhesion force is related to the displacement as:

$$F_{adhesion} = -kx \quad 2.10$$

where k is the spring constant and x is the displacement. The negative sign accounts for the negative force experienced.

In contact mode, the accurate measurement of adhesion forces between the layers of the organic solar cells depends on the spring constant of the AFM cantilever tip [36]. The spring constant can be calculated from the cantilever geometrical and material properties [44, 45]. The mathematical model for the most commonly used V-shaped cantilevers use two-beam approximation, in which the cantilever is described by two rectangular beams in parallel. The expression for the spring constant, k , is given by [46].

$$k = \left(\frac{t}{l} \right)^3 \frac{Ew}{4} \quad 2.11$$

where w , t , l , and E are the width, thickness, length and bulk materials of the cantilever beams. However, the values for the spring constant are provided by most manufacturers of the AFM tip.

We can estimate the adhesion force from equation 2.10 knowing fully well the value of the spring constant. The adhesion force is used to find energy required to separate layers of the stretchable electronic structures like organic solar cells.

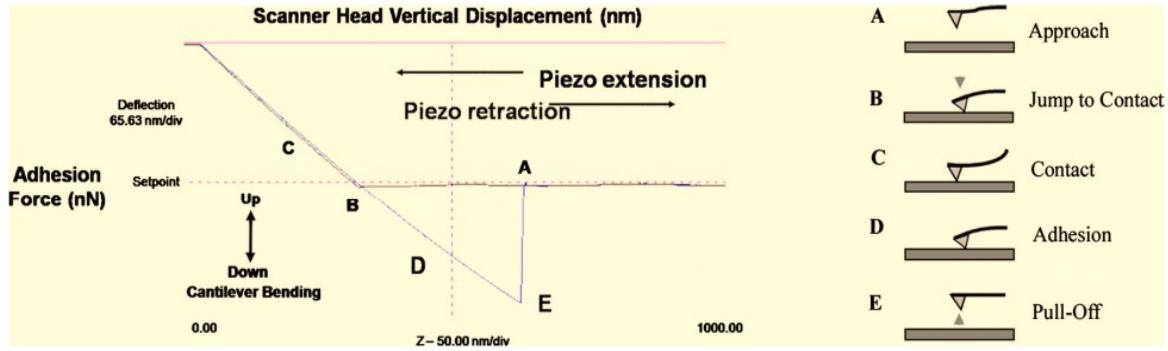


Figure 2.9: Schematic Force-Displacement Curve Depicting the Various Stages [(A)-(E)] of Cantilever-Surface Engagement.(Adapted from Akogwu et al. [53])

2.6.2 Adhesion Energy

Adhesion energy is the work required to build a unit of a particular surface. From fracture mechanics perspective, the adhesion energy, γ , corresponds to the mode I fracture energy G_I . For crack growth between two different materials **a** and **b** with surface energy γ_a and γ_b respectively, the adhesion energy is given by [44]

$$G_{adhesion} \approx G_{elastic} = \gamma_a + \gamma_b - \gamma_{ab} \quad (2.12)$$

where γ_{ab} is an interaction surface energy and $G_{elastic}$ is the mode I energy releases rate for crack growth between materials **a** and **b**.

2.6.3 Adhesion Models

Several models have been developed for different materials and geometry properties of the interacting layers. Among these are Hertzian, Johnson-Kendall-

Roberts (JKR), Darjaguin-Muller-Toporov (DMT), and Maugis-Dugdale (MD) models.

2.6.3.1 Hertzian Model

Hertz was the first to present contact mechanics. He studied the geometrical effects on local elastic deformation properties [47]. Hertzian theory of elastic deformation relates the circular contact area of a sphere with a plane (or in more general cases, between two spheres) to the elastic deformation properties of the materials. It assumed that when the separation between the surfaces is zero, the repulsion resembles a hard sphere model and adhesive forces are negligible. The model is illustrated below in Figure 2.10.

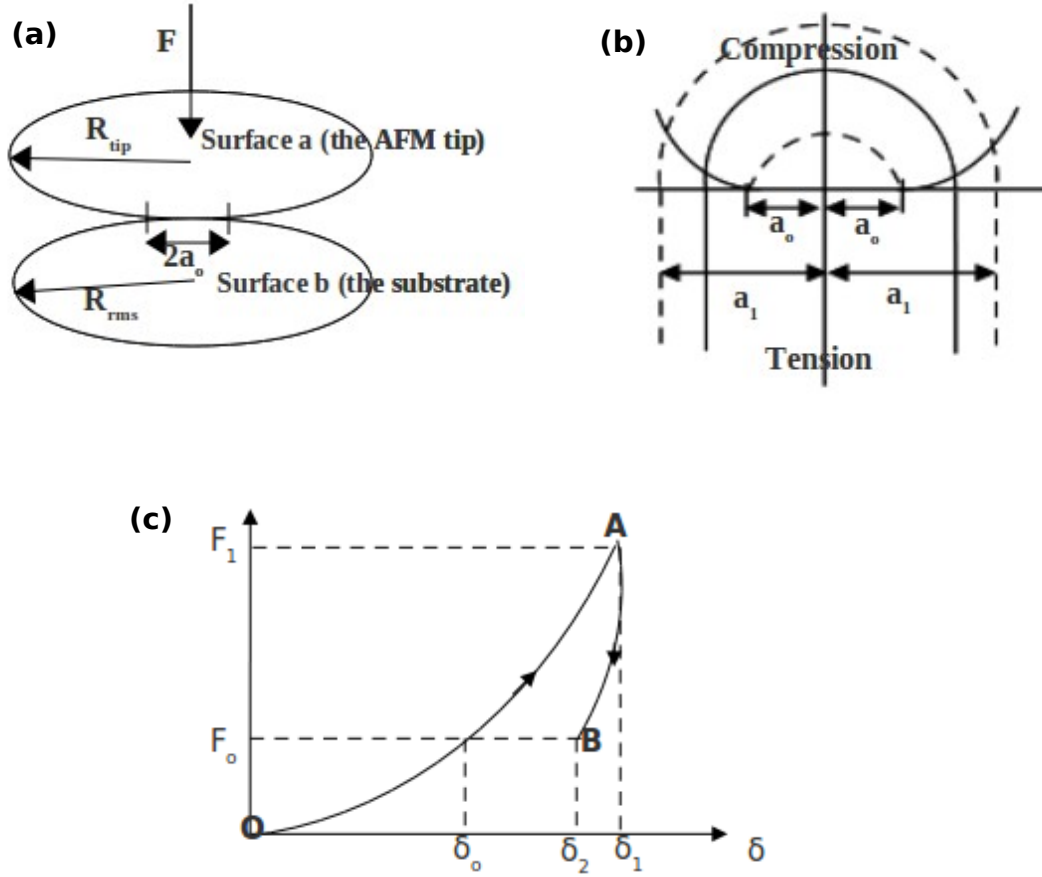


Figure 2.10: The Contact Between Two Elastic Surfaces Both in the Presence (contact radius, a_1) and Absence (Contact Radius, a_o) of the Surface Forces. (a) Contact Between AFM Tip and Substrate, (b) Distribution of Stress in Contacting Surfaces, and (c) Force-Displacement Relation for Contacting Surfaces

When there is no surface force between the two surfaces, the contact radius, a_o is related to applied normal force, F_o , by the following Hertz equation

$$a_o^3 = \frac{RF_o}{K} \quad 2.13$$

Where the effective radius, R and elastic constant, K of the two surfaces a and b is given respectively by:

$$R = \left(\frac{1}{R_a} + \frac{1}{R_b} \right)^{-1} \quad 2.14$$

$$K = \frac{3}{4} \left(\frac{1-\nu_a^2}{E_a} + \frac{1-\nu_b^2}{E_b} \right)^{-1} \quad 2.15$$

Where R_a is the radius of the surface a (tip of the AFM) and R_b is the root-mean squared roughness of the surface b (the substrate), E_a and E_b are the AFM tip and substrate Young's moduli, while ν_a and ν_b are the AFM tip and substrate Poisson ratios respectively.

When there is attractive force between two surfaces, the radius, a_1 corresponds to an apparent Hertz force, F_1 , in equilibrium even though the applied force is still maintained at F_o .

Hertz equation is thus

$$a_1^3 = \frac{RF_1}{K} \quad 2.16$$

The displacement (movement) δ of the applied normal force, F_o is given by

$$\delta = \frac{a^2}{R} \quad 2.17$$

Considering the force-displacement curve (Figure 2.8c), the elastic energy, U_E , of the system can be calculated using the following equation

$$U_E = U_1 - U_2 \quad 2.18$$

Where U_1 is the energy required to give a contact radius, a_1 , when normal force, F_1 , is applied to the system taking surface forces to be zero and U_2 is the energy released to reduce the applied force to F_0 to give the final state (B) of the system.

Using the fact that a small work done is the product of the displacement and small applied force, therefore

$$dU_1 = \delta_1 dF \quad 2.19$$

Combining equations 2.16 and 2.17, gives

$$\delta = \frac{F^{2/3}}{K^{2/3} R^{2/3}} \quad 2.20$$

Equation 2.19 becomes

$$U_1 = \int_0^{F_1} \frac{F^{2/3}}{K^{2/3} R^{1/3}} dF$$

$$U_1 = \frac{2}{3} \frac{F^{5/3}}{K^{2/3} R^{1/3}} \quad 2.21$$

For U_2 , we use the force-displacement relation which is given by [40]:

$$\delta = \frac{2}{3} \frac{F}{K a_1} \quad 2.22$$

Similarly, $dU_2 = \delta dF$

$$U_2 = \int_{F_0}^{F_1} \frac{2}{3} \frac{F}{K a_1} dF$$

$$U_2 = \frac{1}{3 K^{2/3} R^{1/3}} \left[\frac{F_1^2 - F_0^2}{F_1^{1/3}} \right] \quad 2.23$$

Therefore, $U_E = \frac{2}{3} \frac{F_1^{5/3}}{K^{2/3} R^{1/3}} - \frac{1}{3 K^{2/3} R^{1/3}} \left[\frac{F_1^2 - F_0^2}{F_1^{1/3}} \right]$

$$U_E = \frac{1}{K^{2/3} R^{1/3}} \left[\frac{2 F_1^{5/3}}{5} - \frac{F_1^2}{3 F_1^{1/3}} - \frac{F_0^2}{3 F_1^{1/3}} \right]$$

This can be simplified further to give

$$U_E = \frac{1}{K^{2/3} R^{1/3}} \left[\frac{F_1^{5/3}}{15} - \frac{F_0^2 F_1^{-1/3}}{3} \right] \quad 2.24$$

The mechanical energy, U_M due to the applied normal force, F_0 is given by [40]

$$U_M = -F_0 \delta_2 \quad 2.25$$

Where $\delta_2 = \delta_1 - \frac{2dF}{3K a_1}$

$$\delta_2 = \frac{F_1^{2/3}}{K^{2/3} R^{1/3}} - \frac{2}{3} \frac{1}{K a_1} \int_{F_0}^{F_1} dF$$

$$\delta_2 = \frac{F_1^{2/3}}{K^{2/3}R^{1/3}} - \frac{2(F_1 - F_0)}{3Ka_1} \quad 2.26a$$

Substituting equation 2.16 into equation 2.26a, we have

$$\begin{aligned} \delta_2 &= \frac{F_1^{2/3}}{K^{2/3}R^{1/3}} - \frac{2}{3} \left(\frac{K}{RF_1} \right)^{1/3} \left(\frac{F_1 - F_0}{K} \right) \\ \delta_2 &= \frac{F_1^{2/3}}{K^{2/3}R^{1/3}} - \frac{2F_1^{2/3}}{3K^{2/3}R^{1/3}} + \frac{2F_0F_1^{-1/3}}{3K^{2/3}R^{1/3}} \\ \delta_2 &= \frac{1}{K^{2/3}R^{1/3}} \left[\frac{F_1^{2/3}}{3} + \frac{2F_0F_1^{-1/3}}{3} \right] \end{aligned} \quad 2.26b$$

By substituting equation 2.26b into equation 2.25, the mechanical energy, U_E becomes

$$U_M = -\frac{F_0}{K^{2/3}R^{1/3}} \left[\frac{F_1^{2/3}}{3} + \frac{2F_0F_1^{-1/3}}{3} \right] \quad 2.27$$

2.6.3.2 Johnson-Kendall-Roberts (JKR) Model

The first model to account for adhesion forces between surfaces is Johnson-Kendall-Roberts (JKR) model [48]. The model assumed that adhesion forces deform the surface inside the region of contact and that no external attractive forces are present outside this region. It is applicable to tips (two materials in contact) with large radii and small stiffness. Such systems are called strongly

adhesive systems. The model also accounts for the influence of Van der Waals forces within the contact region.

Johnson-Kendall-Roberts (JKR) model assumed that adhesive forces deform the surfaces. The surface energy, U_s due to the adhesion force is given by [40]

$$U_s = -\pi a_1^2 \gamma \quad 2.28$$

Substituting equation 2.16 into 2.28, we have

$$U_s = -\pi \gamma \left(\frac{RF_1}{K} \right)^{2/3} \quad 2.29$$

Where γ is the adhesion energy of both the surfaces (AFM tip and the substrate).

The total energy, U_{total} of the system is made up of the stored elastic energy, U_E , the mechanical energy, U_M , and the surface energy, U_s . That is

$$U_{total} = U_E + U_M + U_s \quad 2.30$$

We substitute equations 2.24, 2.27 and 2.29 into equation 2.30, and then we have

$$U_{total} = \frac{1}{K^{2/3} R^{1/3}} \left[\frac{F_o^{5/3}}{15} + \frac{F_o^2 F_1^{-1/3}}{3} \right] - \frac{1}{K^{2/3} R^{1/3}} \left[\frac{F_o F_1^{2/3}}{3} + \frac{2F_o^2 F_1^{-1/3}}{3} \right] - \frac{\pi \gamma R^{2/3} F_1^{2/3}}{K^{2/3}}$$

Now we find the contact radius of the system. This is possible when the system is

at equilibrium such that $\frac{dU_{total}}{da_1} = 0$

Since F_1 is function of a_1 , we can differentiate the total energy with respect to F_1 and then simplify as follow

$$\frac{dU_{total}}{dF_1} = \frac{1}{K^{2/3}R^{1/3}} \left[\frac{F_1^{2/3}}{9} - \frac{F_o^2 F_1^{-4/3}}{9} \right] - \frac{1}{K^{2/3}R^{1/3}} \left[\frac{2F_o F_1^{-1/3}}{9} - \frac{2F_o^2 F_1^{-4/3}}{9} \right] - \frac{2\pi\gamma R^{2/3} F_1^{-1/3}}{3K^{2/3}} = 0$$

$$\frac{1}{K^{2/3}R^{1/3}} \left[\frac{F_1^{2/3}}{9} - \frac{F_o^2 F_1^{-4/3}}{9} - \frac{2F_o F_1^{-1/3}}{9} + \frac{2F_o^2 F_1^{-4/3}}{9} \right] - \frac{2\pi\gamma R^{2/3} F_1^{-1/3}}{3K^{2/3}} = 0$$

$$\frac{F_1^{-4/3}}{K^{2/3}R^{1/3}} [F_1^2 - F_o^2 - 2F_o F_1 + 2F_o^2 - 6\pi\gamma R F_1] = 0 \quad 2.31$$

Equation 2.31 implies that

$$F_1^2 - F_o^2 - 2F_o F_1 + 2F_o^2 - 6\pi\gamma R F_1 = 0$$

$$F_1^2 - 2F_1(F_o + 3\pi\gamma R) + F_o^2 = 0$$

$$F_1 = \frac{2}{2}(F_o + 3\pi\gamma R) \pm \frac{1}{2}\sqrt{4(F_o + 3\pi\gamma R)^2 - 4F_o^2}$$

$$F_1 = F_o + 3\pi\gamma R \pm \frac{2}{2}\sqrt{F_o^2 + 6\pi\gamma R F_o + (3\pi\gamma R)^2 - F_o^2}$$

$$F_1 = F_o + 3\pi\gamma R \pm \sqrt{6\pi\gamma R F_o + (3\pi\gamma R)^2}$$

We can now ignore the negative sign due to the fact that the system is stable

(that is $\frac{d^2 U_{total}}{dF_1^2} > 0$). Hence

$$F_1 = F_o + 3\pi\gamma R + \sqrt{6\pi\gamma R F_o + (3\pi\gamma R)^2}$$

Since $F_1 = f(a_1) = \frac{a_1^3 K}{R}$,

$$a_1^3 = \frac{R F_1}{K}$$

Therefore,

$$a_1^3 = \frac{R}{K} \left(F_o + 3\pi\gamma R + \sqrt{6\pi\gamma R F_o + (3\pi\gamma R)^2} \right)$$

In general, JKR modification of Hertz equation that consider the surface energy effect is given by

$$a^3 = \frac{R}{K} \left(F + 3\pi\gamma R + \sqrt{6\pi\gamma R F + (3\pi\gamma R)^2} \right) \quad 2.32$$

If the surface energy, γ , is zero, equation 2.32 becomes Hertz equation

The contact area, $A = \pi a^2$, can be written as:

$$A = \pi (DR)^{2/3} \left(F + 3\gamma\pi R + \sqrt{6\gamma\pi R F + (3\gamma\mu R)^2} \right)^{2/3}$$

where $D = \frac{3}{4K}$

For the solution of equation 2.32 to be real, $6\pi\gamma R F + (3\pi\gamma R)^2 \geq 0$ such that

$$6\pi\gamma RF \geq -(3\pi\gamma R)^2 \quad 2.33$$

JKR further predicts that, at $a = 0$ using the fact that equation 2.33 holds, the composite force, F_c is given by

$$F_c = -3\pi\gamma R \quad 2.34$$

The pull off force (adhesion force) needed for separation of the AFM tip and the substrate is given by:

$$F_{adhesion} = \frac{F_c}{2} = -\frac{3\pi\gamma R}{2} \quad 2.35$$

Equation 2.35 implies that the adhesion energy, γ_{JKR} for JKR model can be related to adhesion force, $F_{adhesion}$ as:

$$\gamma_{JKR} = -\frac{2F_{adhesion}}{3\pi R} \quad 2.36$$

2.6.3.3 Derjaguin-Muller-Toporov (DMT) Model

Derjaguin-Muller-Toporov (DMT) presented another theory that considered the adhesive forces to have the nature of Van der Waals forces [49]. This model is used to examine the weak interactions between stiff materials with small radii [45]. It considered the contact radius, a , as a function of applied force as follows.

$$a = \left[\frac{R}{K} (F + 4\pi\gamma R) \right]^{\frac{1}{3}} \quad 2.37$$

Similarly, the composite force, F_c , at $\alpha = 0$, is given by

$$F_c = -4\pi\gamma R \quad 2.38$$

The pull off force required to separate the two surfaces is then given by

$$F_{adhesion} = -2\pi\gamma R$$

Hence, the adhesion energy for DMT model can be related to adhesion force as

$$\gamma_{DMT} = -\frac{F_{adhesion}}{2\pi R} \quad 2.39$$

2.6.3.4 Maugis-Dugdale (MD) Model

Maugis-Dugdale (MD) Model examined the theory of contact on the basis of fracture mechanics [50] and was able to give the analytical solution that matched the JKR or DMT solutions. The model is an intermediate between JKR and DMT models. Maugis considered a 'Dugdale' (square-well) potential to describe adhesive forces between two contacting surfaces. Figure 2.11 below is force per unit area-distance relation for Dugdale model. He determined a dimensionless parameter, λ , which is given by [44, 47]:

$$\lambda = 2\sigma_o \left(\frac{R}{\pi K^2 \gamma} \right)^{1/3} = -0.913 \ln(1 - 1.018\alpha) \quad 2.40$$

In this model, the adhesion energy, $\gamma = \sigma_o \delta_t$

where σ_o is a constant (maximum) adhesion stress (Force per area), δ_t is the separation height (range), α is the transition parameter. The adhesion energy can also be written as [44]:

$$\gamma = \frac{F_{adhesion}}{\pi R f_{adhesion}} \quad 2.41a$$

$$\text{where } f_{adhesion} = 0.267 \alpha^2 - 0.757 \alpha + 2 \quad 2.1b$$

The dimensionless parameter, λ , can be used to characterize the entire range of adhesion models. According to Tong et al., if $\lambda = 5$, the JKR model applies and if $\lambda = 0.1$, the DMT model is applies. The interval $0.1 < \lambda < 5$ corresponds to MD model, which is a regime between JKR and DMT models. The Hertz, JKR, DMT, and MD models are summarized below in table 2.1.

Table 2.1: Summary of Hertz, JKR, DMT, and MD Models

Model	Assumptions	Restrictions
Hertz	No surface forces	It is not applied to small loads in the presence of surface forces
JKR	The surface forces act within the contact region	It is applied only to large value of dimensionless parameter, λ of about 5.0
DMT	The surface forces act only outside the contact region	The dimensionless parameter, $\lambda = 0.1$
MD	The tip-sample interface is modeled as a ring	It is applied to all values of λ between 0.1 and 5

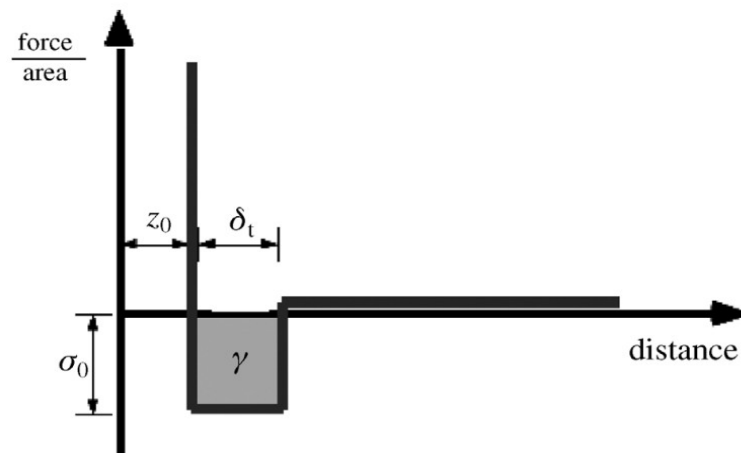


Figure 2.11: Force (per unit area)-Distance Relation for Dugdale Model (Adapted from [50])

2.7 REFERENCES

- [1] Einstein Albert, *Ann. Phys.*, Lpz 17, 549-560, 1905
- [2] www.nobelprize.org/physics/laureates/1956
- [3] A. V. Shah, H. Schade, M. Vanecek, J. Meier, E. Vallat-Sauvain, N. Wyrsch, U. Kroll, C. Droz and J. Bailat: *Prog. Photovolt: Res. Appl.* 2004; 12:113-142
- [4] Kalu Uduma and Tomasz Arciszewski: *Sustainable Energy Development, Sustainable* 2010, 2, 1558-1570
- [5] H. Hoppe and N. S. Sariciftci, *Organic Solar Cells: An Overview*, *J. Mater. Res.*, Vol. 19, No. 7 (2004)
- [6] Tang, C. W.: *Two-layer organic photovoltaic cell*. *Appl. Phys. Lett.* 48, 183-185 (1986)
- [7] A. Goetzberger, C. Hebling, and H. W. Schock: *Photovoltaic materials, history, status and outlook*. *Mater. Sci. Eng. R* 40, 1(2003).
- [8] G.A. Chamberlain: *Organic solar cells: A review*. *Solar Cells* 8,47 (1983).
- [9] D. Wöhrle and D. Meissner: *Organic solar cells*. *Adv. Mater.* 3,129 (1991).
- [10] C.J. Brabec, N.S. Sariciftci, and J.C. Hummelen: *Plastic solar cells*. *Adv. Funct. Mater.* 11, 15 (2001).
- [11] J.J.M. Halls and R.H. Friend: in *Clean Electricity from Photo-voltaics*, edited by M.D. Archer and R. Hill (Imperial College Press, London, U.K., 2001).
- [12] J. Nelson: *Organic photovoltaic films*. *Curr. Opin. Solid State Mater. Sci.* 6, 87 (2002).
- [13] J-M. Nunzi: *Organic photovoltaic materials and devices*. *C. R. Physique* 3, 523 (2002).
- [14] C.J. Brabec, V. Dyakonov, J. Parisi, and N.S. Sariciftci: (Springer, Berlin, Germany, 2003). *Organic Photovoltaics: Concepts and Realization*; Vol. 60
- [15] P. Peumans, A. Yakimov, and S.R. Forrest: *Small molecular weight organic thin film photodetectors and solar cells*. *J. Appl. Phys.* 93, 3693 (2003).
- [16] Arkhipov, V. I., Bäessler, H.: *Exciton dissociation and charge photogeneration in pristine and doped conjugated polymers*. *Phys. Status Solidi A.* 201, 1152-1187 (2004)
- [17] Nunzi, J. M.: *Organic photovoltaic materials and devices*. *C. R. Physique.* 3, 523- 542 (2002)
- [18] Yu, G., Gao, J., Hummelen, J. C., Wudl, F., Heeger, A. J.: *Polymer Photovoltaic Cells: Enhanced Efficiencies via a Network of Internal Donor-Acceptor Heterojunctions*, *Science*, 270, 1789-1791 (1995)
- [19] N. S. Sariciftci, L. Smilowitz, A. J. Heeger and F. Wuli, *Science* (1992), Vol. 258, No. 5087, 1474-1476.
- [20] Gilles Dennler, Markus C. Scharber, and Christoph J. Brabec: *Polymer-Fullerene Bulk, Heterojunction Solar Cells*, *Adv. Mater.* (2009), 21, 1323-1338.
- [21] Joachim Loos, : *Volume Morphology of Printable Solar Cells*, *Materials today*, Vol. 13, No. 10 (2010).

- [22] S. M. Sze, *Physics of Semiconductor Devices* (Wiley, New York, 1981)
- [23] L. J. A. Koster, V. D. Mihailetschi, R. Ramaker, P. W. M. Blom: Light intensity dependence of open-circuit voltage of polymer:fullerene solar cells. *Appl. Phys. Lett.* 86, 123509 (2005)
- [24] G. Dennler, C. Lungenschmied, H. Neugebauer, and N.S. Sariciftci: Flexible, conjugated polymer-fullerene-based bulk-heterojunction solar cells: Basics, encapsulation, and integration, *J. Mater. Res.*, Vol. 20, No. 12, 2005
- [25] Sariciftci, N. S., Günes, S., Neugebauer, H.: Conjugated Polymer-Based Organic Solar Cells. *Chem. Rev.* 107, 1324-1338 (2007)
- [26] Ma, W.L., Yang, C.Y., Gong, X., Lee, K., and Heeger, A.J.: Thermally stable, efficient polymer solar cells with nanoscale control of the interpenetrating network morphology. *Advanced Functional Materials*, 2005. 15(10): p. 1617-1622.
- [27] F. C. Krebs et al.: *Sol. Energy Mater – Solar cells* 93 (2009) 1968-1977
- [28] M. Al-Ibrahim, H. K. Roth, M. Schoeder, A. Kankin, U. Zhokhavets, G. Gobsch, P. Scharff, S. Sensfuss: *Org. Electron* 6(2005) 65-77
- [29] L. Blankenburg, K-Schulthesis, H. Schach, S Sensfuss, M. Schroder, *Sol. Energy Mater. Sol. Cell* 93(2009) 476-483
- [30] R. Steim, P. schilinsky, S. A. Choulis, C. J. Brabee, *Sol. Energy Mater. Sol. Cells* 93(2009)1963-1967
- [31] F. C. Krebs, T. O. Nielson, J. Fyanbo, M. Wadstrom, T. S. Pederson, *Energy Environ. Sci.* 3(2010) 512-525
- [32] F. C. Krebs, S. A. Gevorgyan, J. Alstrup: *J. Mater. Chem.* 19(2009) 5442-5451
- [33] F. C. Krebs, *Organic Electron.* 10(2009) 761-768
- [34] G-Li V. Shrotriya, J. Huang, Y. Yea, T. Moriarty, K. Emery, Y. Yong, *Nat. Mater.* 4(2005) 864-868
- [35] Sheng Chu, Dongdong Li, Pai-Chun Chang, Jia G. Lu: *Nanoscale Research Letter* (2011) 6: 38
- [36] D. R. Hodges, V. Palekis, S. Bhandaru, K. Singh, D. Morel, E. K. Stefanakos, and C. S. Ferekides: *Mater. Res. Soc. Symp. Proc. Vol. 1165*(2009)[37],
- [37] T. Aernouts, P. Vanlaeke, W. Geens, J. Poortmans, P. Heremans, S. Borghs, R. Mertens, R. Andriessen, L. Leenders: *Printable anodes for flexible organic solar cell modules, Thin Solid Films* 451 – 452 (2004) 22-25
- [38] Y. Zhou, F. Li, S. Barrau, W. Tian, O. Inganäs, F. Zhang, *Inverted and transparent Polymer solar cells prepared with vacuum-free processing, Sol. Energy Mater. Sol. Cells* 93 (2009) 497-500.
- [39] Y Galagan, Jan-Eric J.M. Rubingh, R. Andriessen, Chia-Chen Fan, Paul W.M. Blom, S. C. Veenstra, J. M. Kroon: *ITO-free flexible organic solar cells with printed current collecting grids, Solar Energy Materials & Solar Cells* 95 (2011) 1339-1343
- [40] Stephenie P. Lacour, Joyelle Jones, Sigurd Wegner: *Elastomeric Interconnects, International Journal of High Speed Electronics and Systems*, Vol. 16, No 1 (2006)

- [41] S. Midturi: *Stress-Strain Behavior of Nano/Micro Thin Film Materials*, ARPN Journal of Engineering and Applied Sciences, vol. 5, no. 3, 2010
- [42] O. Akogwu, D. Kwabi, S. Midturi, M. Eleruja, B. Babatope, W.O. Soboyejo: *Large Strain Deformation and Cracking of Nano-Scale Gold Films on PDMS Substrate*, Materials Science and Engineering B 170 (2010) 32–40
- [43] D. R. Hodges, V. Palekis, S. Bhandaru, K. Singh, D. Morel, E. K. Stefenakos, and C. S. Ferekides: *Mater. Res. Soc. Symp. Proc. Vol. 1165*(2009)
- [44] T. Tong, B Babatope, S. Admassie, J. Meng, O. Akwogu, W. Akande and W. O. Soboyejo: *Adhesion in Organic Structures*, Journal of Applied Physics 106, 083708 (2009).
- [45] O. Akogwu, D. Kwabi, A. Munhutu, T. Tong, and W. O. Soboyejo: *Adhesion and cyclic stretching of Au thin film on poly(dimethyl-siloxane) for stretchable electronics*, Journal of Applied Physics, 108, 123509 (2010)
- [46] Rev. AO, Vol. AN90 □Veeco Instruments Inc., 2005.
- [47] J.A. Greenwood, "Adhesion of Elastic Spheres". *Proc. R. Soc. Lond. A* (1997) 453, 1277-1297
- [48] K. L. Johnson and K. Kendall and A. D. Roberts: *Surface energy and the contact of elastic solids*, *Proc. R. Soc. Lond., A* 324 (1971) 301–313.
- [49] B. V. Derjaguin and V. M. Muller and Y. P. Toporov: *Effect of contact deformations on the adhesion of particles*, *J. Colloid Interface Sci.* 53 (1975) 314–325.
- [50] D. Maugis and M. Barquins and R. Courtel, *M'iaux: Corrosion, Industrie* 605 (1976) 1.
- [51] D. S. Grierson, E. E. Flater and R. W. Carpick: *Accounting for the JKR–DMT transition in adhesion and friction measurements with atomic force microscopy*, *J. Adhesion Sci. Technol.*, Vol. 19, No. 3–5, pp. 291– 311 (2005)
- [52] J. M. Neumeister and W. A. Ducker. *Rev. Sci. Instrum.* **65**, 2527 (1994).
- [53] J. E. Sader, I. Larson, P. Mulvaney, L. R. White. *Rev. Sci. Instrum.* **66**, 3789 (1995).
- [54] J. E. Sader. *Rev. Sci. Instrum.* **66**, 4583 (1995).
- [55] M. Pagliaro, C. Palmisano, and R. Ciriminna, *Flexible Solar Cells*, (2008), 1-20
- [56] S. K. Hau, H.-L. Yip, J. Zou, A.K.Y. Jen: *Indium tin oxide-free semi-transparent inverted polymer solar cells using conducting polymer as both bottom and top electrodes*, *Organ. Electron.* 10 (2009) 1401–1407.
- [57] J. Weiss, P. Kukuri, J. Chiguma, J. Gendon, B. Arfaei, P. Borgesen, and W. Jones, *Fabrication of low cost flexible solar using solution-based coating techniques*, *Global Solar Technology* (2011) 10-15

CHAPTER 3

MODELLING OF ADHESION EFFECTS ON CONTACT LENGTHS AND DEFORMATIONS INDUCED AT THE INTERFACES OF ORGANIC ELECTRONIC STRUCTURES

3.1 Introduction

In recent years, there has been increasing interest in the development of flexible electronic for applications in electronic textile [19], flexible solar cells, etc [2, 6, 12]. However, their optoelectronic properties are at risk, as they undergo deformation. Furthermore, the residual stresses that occur during their fabrication can also contribute to their failure. In cases in which interfacial failure can be induced [2, 12], the adhesion between layers is concern. The adhesion has been modelled using analytical, numerical simulation and experimental techniques. In the case of bulk heterojunction organic solar cells, the new solar cells (PDMS/ITO/PEDOT:PSS/P3HT:PCMB/Al) have four interfaces that require excellent adhesion for performance.

This chapter introduces mechanics and physics models of deformation-induced phenomena in stretchable organic solar cells. The deformation arises

during the fabrication and use of the devices. Furthermore, since the devices are often used under monotonic loading, this chapter focuses on the mechanics and mechanisms of damage in flexible solar cells deformed under monotonic loading. The deformation-induced phenomena are related to stress distributions computed using finite element models. Analytical models of adhesion energies are presented along with finite element simulation on contact between layers that are relevant to stretchable bulk heterojunction solar cells. The models explore effects of adhesion on contact, while the finite element simulations explore the stress distributions and contacts between layers that are relevant to charge transport across bulk heterojunction solar cells.

Following the introduction (section one), modelling of adhesion energies of the interfaces is discussed in section two. The modeling of adhesion effects on contact lengths is presented in section three. Residual stresses are also estimated using mechanics model in section four. The expressions for the estimation of crack driving forces for delamination are also presented in this section. Results and discussion of the analytical and finite element simulations are presented in section five before the salient conclusions arising from this study are presented in section six.

3.2. Measurement of Adhesion Energy

Adhesion energies are needed for modelling of the role of adhesion during contact between two surfaces. Although they can be computed, adhesion energies can also be measured using a combination of force microscopy and adhesion theory [2]. The choice of adhesion theory depends on the properties of the contacting surfaces, in chapter 2 of this thesis. In the current study, the interactions between stiff materials [2,3,4] was described using the DMT model [2, 20 - 23]. This gives the adhesion energy as:

$$\gamma_{DMT} = -\frac{F_{adhesion}}{2\pi R} \quad 3.1$$

where $F_{adhesion}$ is adhesion force and R is given by:

$$R = \left(\frac{1}{R_{tip}} + \frac{1}{R_{rms}} \right)^{-1} \quad 3.2$$

where R_{tip} and R_{rms} are radius of AFM tip and root mean square roughness of the substrate. Knowing the value of $F_{adhesion}$ and R, we can estimate the adhesion energies of each of the interfaces in the layers of organic electronic structures [2]. Typical values of the adhesion energies obtained in prior work of Tong et al. [2] are presented in Figure 3.1.

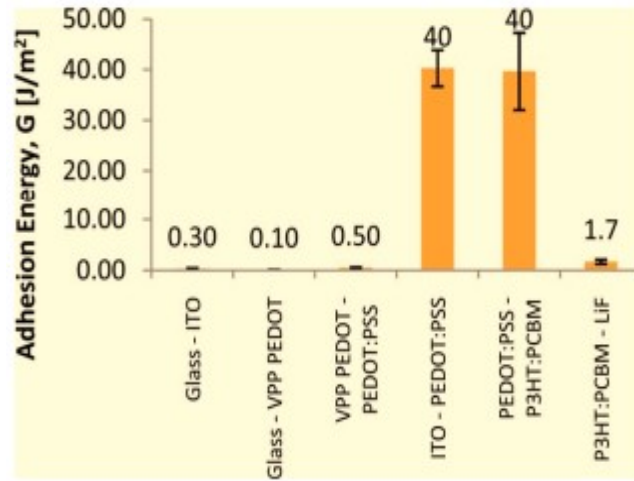


Figure 3.1: Comparison of Adhesion Energies of Layers of a Typical Organic Solar Cell

3.3 Modeling of Adhesion Effects on Contact Lengths

During the deposition of layers of organic electronic materials in a clean room, there is high possibility of depositing on particles of dust. This might, in one way or the other, affects the adhesion between the interfacial structures of the fabricated device. This section explores the effects of dust particles and adhesion on contact lengths between bi-material pairs that are relevant to organic electronic structures.

We consider a simple structure of a sandwiched dust particle between two layers of organic electronic materials. We refer to h_o as the height of the dust particle before deformation and t_1 and t_2 as the thickness of the two layers, where 1 and 2 designate layer 1 and layer 2, respectively. Before deposition of

the top layer (layer 1), we assume that the particle has already settled on layer 2, as shown below in Figure 3.2a. After deposition, provided that the thickness of layer 1 is greater than the height of the dust particle ($t_1 > h_o$), the top layer covers the particle completely, as shown in Figure 3.2c.

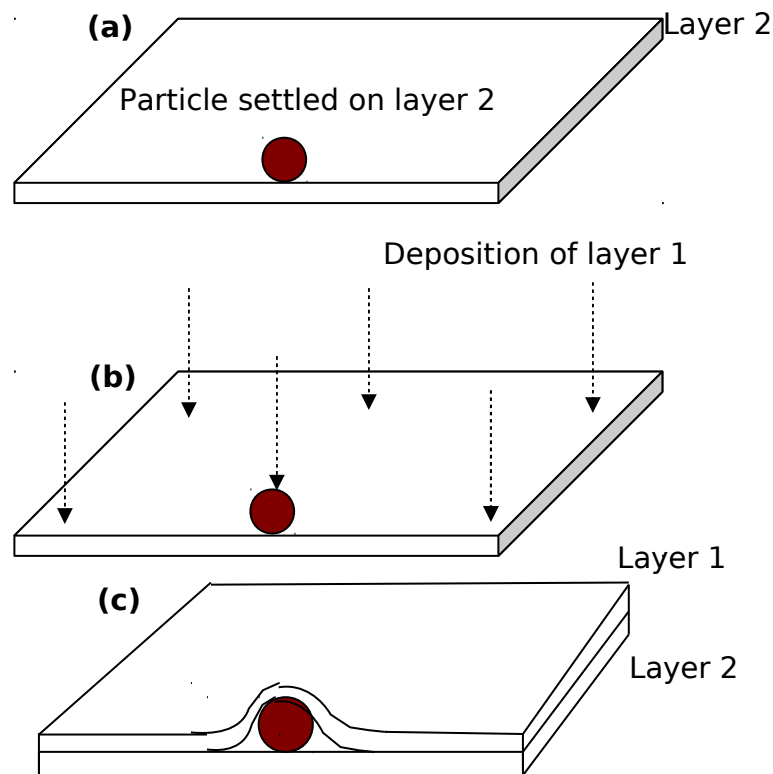


Figure 3.2: Schematic of Deposition of a Thin Film on a Dust Particle (a) the Particle Settled on Layer 2 Before Deposition (b) During Deposition of Layer 1 With Uniform Pressure and (c) after Deposition of Layer 1

The above demonstration can be modeled axisymmetrically (Figure 3.3), which is similar to a cantilever beam of length, L width, w and thickness, t_1 . The final structure (after deposition of layer 1 by magnetron sputtering technique) is an s-shape of the cantilever beam. The elastic energy stored in the beam is given by [7, 13]:

$$U_e = \frac{6EIh^2}{s^3} \quad 3.3$$

where E is the Young's modulus, I is the second moment area of the beam, h is the height of the dust particle after deposition, and s is the void length (the length where there is no contact between the two layers).

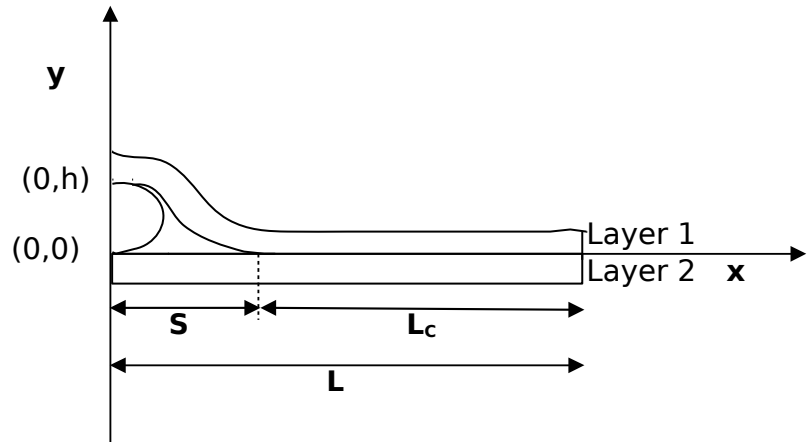


Figure 3.3: Schematic of Axisymmetric Model of Contact Around Dust Particle

The surface energy, U_s , due to adhesion at the region where there is contact is given by:

$$U_s = -\gamma A_c \quad 3.4$$

where A_c is the contact area and γ is the adhesion energy. The contact area can be written as:

$$A_c = w \times L_c = w \times (L - s)$$

where L_c is the contact length. The surface energy is thus:

$$U_s = -\gamma w(L - s)$$

The total energy of the system is the sum of both the elastic energy stored in the beam and the surface energy. This is given by:

$$U_T = \frac{6EIh^2}{s^3} - \gamma w(L - s) \quad 3.5$$

This total energy is minimum at equilibrium value of s . By differentiating equation 3.5 with respect to s , we have:

$$\frac{dU_T}{ds} = -\frac{18EIh^2}{s^4} + \gamma w$$

At equilibrium, $\frac{dU_T}{ds} = 0$, hence

$$\gamma = \frac{18EIh^2}{s^4 w} \quad 3.6a$$

The analytical form of the second moment area, I , is given by [12]:

$$I = \frac{wt^3}{12} \quad 3.6b$$

Combining equations 3.6a and 3.6b, we have

$$\begin{aligned} \gamma &= \frac{3}{2} \frac{Et^3 h^2}{s^4} \\ s^4 &= \frac{3}{2} \frac{Et^3 h^2}{\gamma} \\ s &= \left(\frac{3}{2} \frac{Et^3 h^2}{\gamma} \right)^{1/4} = L - L_c \\ L_c &= L - \left(\frac{3}{2} \frac{Et^3 h^2}{\gamma} \right)^{1/4} \end{aligned} \tag{3.7a}$$

The nominal contact length is thus given by:

$$\frac{L_c}{L} = 1 - \frac{1}{L} \left(\frac{3}{2} \frac{Et^3 h^2}{\gamma} \right)^{1/4} \tag{3.7b}$$

3.4 Estimation of Residual Stresses, Mechanical Stresses and Crack Driving Forces

3.4.1 Residual Stresses

Residual stresses are present in the layered organic electronic structures, especially when some of the layers are deposited at high temperature. Hence, if we refer to T_i as the layer deposition temperature of the deposition of the layers i , then the residual stress is associated with the temperature difference between T_i

and room temperature. Assuming an elastic response, we consider the effect of change in temperature from T_i to room temperature, T to be $\Delta T = T_i - T$.

For simplicity, we consider the first layer (ITO) of the structure on unbuckled PDMS. Assuming that the component of strain, ε_{33} and stress component, σ_{33} , due to thermal expansion mismatch along z-direction are zero, then the generalized plane stress conditions [5] of the first layer and the PDMS are given, respectively, by:

$$\sigma_{\alpha\beta}^1 = \frac{E_1}{1-\nu_1^2} [\varepsilon_{\alpha\beta}^1 + \nu \varepsilon_{\gamma\gamma}^1 \delta_{\alpha\beta}] \quad 3.8a$$

$$\sigma_{\alpha\beta}^s = \frac{E_s}{1-\nu_s^2} [\varepsilon_{\alpha\beta}^s + \nu \varepsilon_{\alpha\beta}^s \delta_{\alpha\beta}] \quad 3.8b$$

We also consider t_1 and t_2 to be the thickness of PDMS and ITO respectively such that $t_2 \ll t_1$. Upon deposition of ITO on PDMS, the PDMS expands freely, The strains, $\varepsilon_{\alpha\beta}^1$, due to thermal expansion, α_1 , of the PDMS are given by:

$$\varepsilon_{\alpha\beta}^s = \alpha_s \Delta T \delta_{\alpha\beta}, \quad \alpha, \beta = 1, 2 \quad 3.9a$$

$$\alpha_{\gamma\gamma}^s = \alpha_s \Delta T$$

Away from the edges of the composite, the in plane strains of the PDMS and ITO are the same [6]

$$\varepsilon_{\alpha\beta}^1 = \varepsilon_{\alpha\beta}^s, \quad \alpha, \beta = 1, 2$$

where $\varepsilon_{\alpha\beta}^1$ is the strain of the ITO, which is given by:

$$\varepsilon_{\alpha\beta}^1 = \alpha_1 \Delta T \delta_{\alpha\beta} \quad 3.9b$$

$$\varepsilon_{\gamma\gamma}^1 = \alpha_1 \Delta T \quad 3.9c$$

Assuming $E_1 \sim E_2$ and $\nu_1 \sim \nu_2$

$$\sigma_{\alpha\beta}^1 = \Delta \sigma_{\alpha\beta} = \frac{E_1}{1-\nu_1^2} [\varepsilon_{\alpha\beta}^s + \nu_1 \varepsilon_{\gamma\gamma}^s \delta_{\alpha\beta} - \varepsilon_{\alpha\beta}^1 - \nu_1 \varepsilon_{\gamma\gamma}^1 \delta_{\alpha\beta}] \quad 3.10$$

By substituting equation 3.9a and 3.9b into 3.10 gives

$$\sigma_{\alpha\beta}^1 = \frac{E_1}{1-\nu_1^2} [\alpha_s \Delta T \delta_{\alpha\beta} + \nu_1 \alpha_s \Delta T \delta_{\alpha\beta} - \alpha_1 \Delta T \delta_{\alpha\beta} - \nu_1 \alpha_1 \Delta T \delta_{\alpha\beta}] \quad 3.11$$

$$= \frac{E_1}{1-\nu_1^2} [\alpha_s + \nu_1 \alpha_s - \alpha_1 - \nu_1 \alpha_1] \Delta T \delta_{\alpha\beta}$$

$$= \frac{E_1}{1-\nu_1^2} [\alpha_s (1 + \nu_1) - \alpha_1 (1 + \nu_1)] \Delta T \delta_{\alpha\beta}$$

$$= \frac{E_1}{1-\nu_1^2} (\alpha_s - \alpha_1) (1 + \nu_1) \Delta T \delta_{\alpha\beta}$$

$$\sigma_{\alpha\beta}^1 = \frac{E_1 (\alpha_s - \alpha_1) \Delta T \delta_{\alpha\beta}}{1-\nu_1} \quad 3.12$$

Equation 3.12 is the residual stress due to thermal expansion mismatch when the first layer, ITO, is deposited on an unbuckled PDMS substrate.

Similarly, the residual stresses of other layers that are deposited on ITO-coated PDMS are estimated. In general, the residual stresses of each of the layers deposited on the PDMS substrate are given by:

$$\sigma_{\alpha\beta}^i = \frac{E_i(\alpha_s - \alpha_i)(T - T_i)\delta_{\alpha\beta}}{1 - \nu_i} \quad , \quad \alpha, \beta = 1, 2$$

This implies that

$$\sigma_{11}^i = \sigma_{22}^i = \frac{E_i(\alpha_s - \alpha_i)(T - T_i)}{1 - \nu_i} \quad 3.13$$

We can, from equation 3.13, compute the residual stress of the composite structure as:

$$\sigma = \sum_{i=1}^4 \sigma^i = \sum_{i=1}^4 \frac{E_i(\alpha_s - \alpha_i)(T - T_i)}{1 - \nu_i} \quad 3.14$$

Equation 3.13 is used to calculate the residual stresses of the layers of the organic electronic structure, while equation 3.14 is used to compute the residual stress of the composite structure.

Since both PEDOT: PSS ($i = 2$) and P3HT: PCBM ($i = 3$) are spin-coated onto the ITO-coated PDMS, the deposition temperatures T_i ($i = 2, 3$) is assumed to be the same with the room temperature (T) and therefore, their residual stresses, σ^2, σ^3

are zero. Hence, residual stresses are induced only during the deposition of ITO ($i = 1$) and Al ($i = 4$).

3.4.2 Mechanical Stresses

Since organic electronic structures are being considered for application in stretchable electronic structures, they can deform under service conditions. However, there is an extent to which they can be stretched without significant damage [6]. In this study, a simple composite framework (Figure 3.4) is used to model the deformation behaviour of stretchable solar cells.

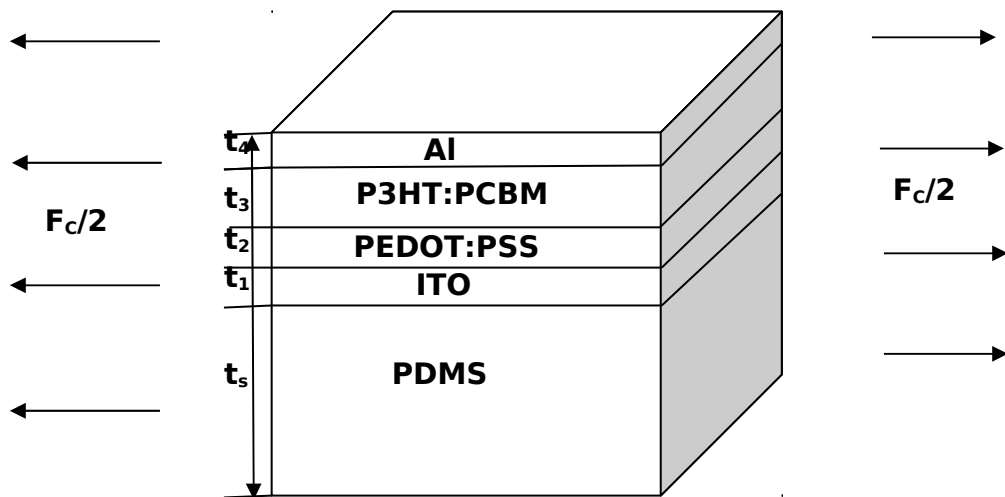


Figure 3.4: Schematic of Organic Electronic Structure under Tensile Force

We consider the composite system of the device shown in Figure 3.4a. PDMS, ITO, PEDOT:PSS, P3HT:PCBM, and Al layers of the system are designated by layers s , 1, 2, 3, and 4 respectively. Also, t_s , t_1 , t_2 , t_3 , and t_4 refer to the thickness of PDMS substrate, ITO, PEDOT:PSS, P3HT:PCBM, and Al, respectively. Each of the layers has the same width, w . Using a simple force balance, the total force on the composite [12], F_c is the sum of the forces on the PDMS, F_s , ITO, F_1 , PEDOT:PSS, F_2 , P3HT:CBM, F_3 , and the Al, F_4 . The total force, F_c on the composite is given by:

$$F_c = F_s + F_1 + F_2 + F_3 + F_4 \quad 3.15$$

We also use the fact that the force is the product of stress, σ and cross sectional area, A . Furthermore, the cross-sectional area, A is the product of the width, w and the thickness, t . Hence, the forces on the PDMS, ITO, PEDOT: PSS, P3HT: PCBM, and Al layers can be written, respectively, as:

$$F_s = \sigma_s \times A_s = \sigma_s \times w \times t_s = \sigma_s w t_s \quad 3.16a$$

$$F_1 = \sigma_1 \times A_1 = \sigma_1 \times w \times t_1 = \sigma_1 w t_1 \quad 3.16b$$

$$F_2 = \sigma_2 \times A_2 = \sigma_2 \times w \times t_2 = \sigma_2 w t_2 \quad 3.16c$$

$$F_3 = \sigma_3 \times A_3 = \sigma_3 \times w \times t_3 = \sigma_3 w t_3 \quad 3.16d$$

$$F_4 = \sigma_4 \times A_4 = \sigma_4 \times w \times t_4 = \sigma_4 w t_4 \quad 3.16e$$

By substituting equations 3.16(a-e) into equation 3.15, we obtain:

$$F_C = \sigma_s w t_s + \sigma_1 w t_1 + \sigma_2 w t_2 + \sigma_3 w t_3 + \sigma_4 w t_4 \quad 3.17$$

Now, we refer to total cross-sectional area of the system, the total thickness of the system, and the stress applied to the system as A_C , t_{total} , and σ_C respectively, such that

$$F_C = \sigma_C \times A_C = \sigma_C \times w \times t_{total} = \sigma_C w t_{total} \quad 3.18$$

Substituting equation 3.18 for F_C into equation 3.17 gives:

$$\begin{aligned} \sigma_C w t_{total} &= \sigma_s w t_s + \sigma_1 w t_1 + \sigma_2 w t_2 + \sigma_3 w t_3 + \sigma_4 w t_4 \\ \sigma_C &= \frac{1}{t_{total}} (\sigma_s t_s + \sigma_1 t_1 + \sigma_2 t_2 + \sigma_3 t_3 + \sigma_4 t_4) \end{aligned} \quad 3.19$$

Furthermore, each of the layers of the organic electronic structures has different elastic properties. Hence, the stresses, σ_i , experienced by layers can be related to their Young's moduli, E_i and strains, ϵ_i . Thus gives :

$$\sigma_i = E_i \epsilon_i, \quad i = s, 1, 2, 3, 4 \quad 3.20$$

Substituting equation 3.20 into 3.19, gives:

$$\sigma_C = \frac{1}{t_{total}} (E_s \epsilon_s t_s + E_1 \epsilon_1 t_1 + E_2 \epsilon_2 t_2 + E_3 \epsilon_3 t_3 + E_4 \epsilon_4 t_4) \quad 3.21a$$

Or

$$\sigma_c = \frac{1}{t_{total}} \{E_s \varepsilon_s t_s + \sum_{i=1}^N E_i \varepsilon_i t_i\}, N = 4 \quad 3.21b$$

Equation 3.21 can be used to estimate the stress-strain behaviour of each layer within the stretchable organic solar cell. Also, for a bilayer structure with a thin film on a stretchable substrate, equation 3.21 can be used with $N=1$.

3.4.3 Crack Driving Forces

This section presents crack driving forces that are relevant to layers of stretchable organic solar cells. During service, the layers of stretchable organic solar cells may experience damage through cracks propagation as a result of stretching. For simplicity, we considered a simple crack growing on a thin film deposited on a flexible substrate PDMS (Figure 3.5). For a compliant substrate, the applied tensile force (F_c) on the composite is expected to damage the deposited thin film without having significant effects on the substrate.

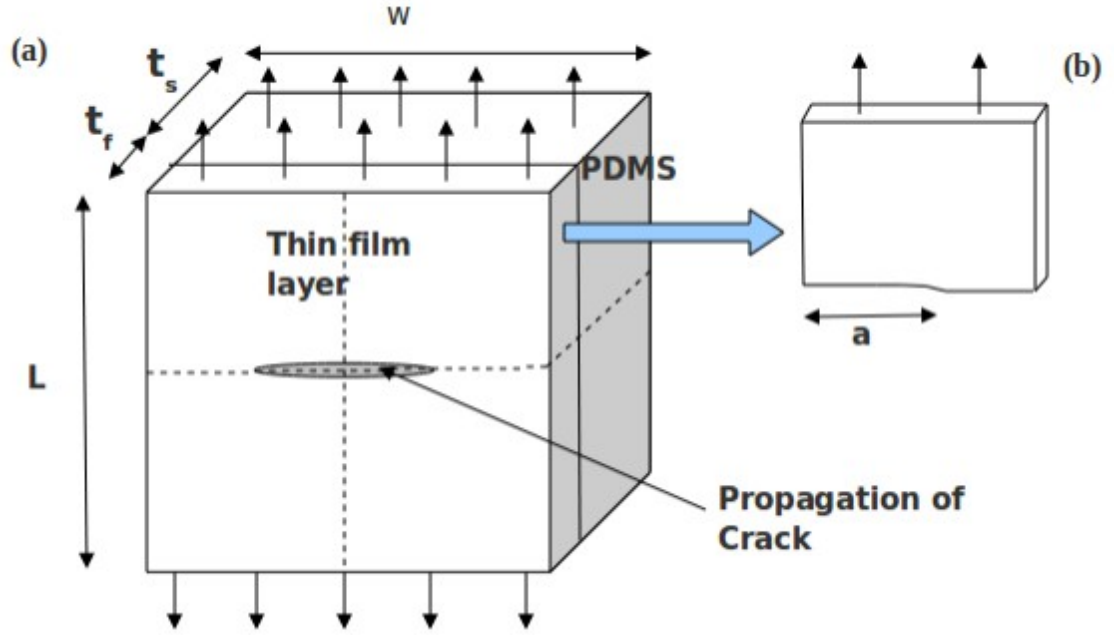


Figure 3.5: A Simple model of Crack Propagation in (a) a Thin Films on PDMS and (b) a Quarter of the Deposited Thin Film

We refer to L , w , t_s , t_f as the length, width, thickness of the substrate, and thickness of the film, respectively. In this model, a fracture mode I loading was considered such that the measure of stress concentration, K_I , on the film is given by [11, 17]:

$$K_I = f\sigma\sqrt{\pi a} \quad 3.22$$

where a is the crack length, σ is the applied stress, and f is a non-dimensional function of the material's relative crack length and the loading angle. The value

of f has been previously determined by Atkinson, et al [18], which can be determined by using ABAQUS. The energy release rate, G , is given by [11, 17, 18]:

$$G = \frac{K_I^2}{E^I} \quad 3.23$$

where $E^I = \frac{E}{(1-\nu^2)}$ for plane strain

3.5 RESULTS AND DISCUSSION

3.5.1 Results of Analytical Modelling

Estimates of the contact lengths obtained from equations 3.7a and b, using the prior measurements of material properties in Table 3.1, are presented in Figure 3.6 (a-f).

Table 3.1: Properties of the Materials used for the Modelling

Material	Young's Modulus (GPa)	Poisson Ratio	References
PDMS	0.003	0.48	[2], [8]
Dust	70	0.3	[2], [7]
PEDOT:PSS	1.56±0.08	0.3	[2]
P3HT:PCBM	6.02	0.35	[10]
ITO	116	0.35	[9],
Al	70	0.3	[11]

The results shows that, the void length between two layers of organic solar cells, increases with increasing height of the sandwiched dust particles. Hence, high efficiency performing organic solar cells can be fabricated in clean rooms/glove boxes with small dust particle sizes. Conversely, layer dust particle sizes increase the void lengths that are observed in organic electronic structures. Such voids can reduce the extent of charge transport between layers that are relevant to organic solar cells or light emitting devices. They may , therefore, compromise their efficiencies.

Furthermore, increasing Young's moduli result in increasing void length and decreasing contact length (Figures 3.6c and 3.6d).

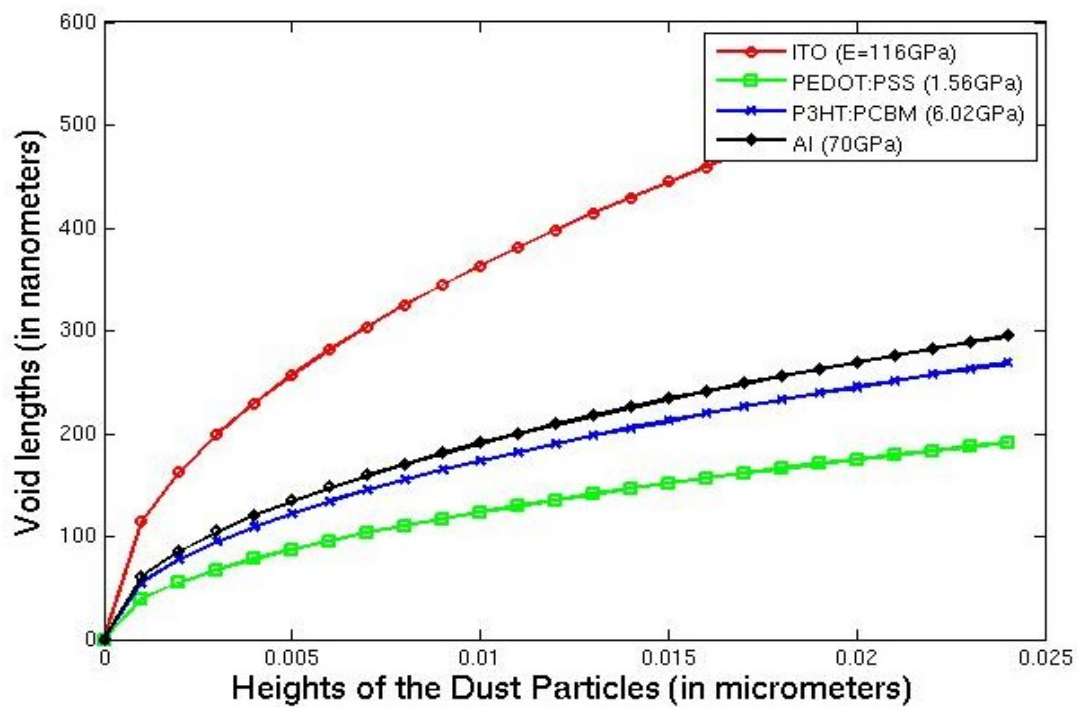


Figure 3.6a: Void Lengths as Functions of Heights of the Dust Particles of Various Layers of a Typical Organic Electronic

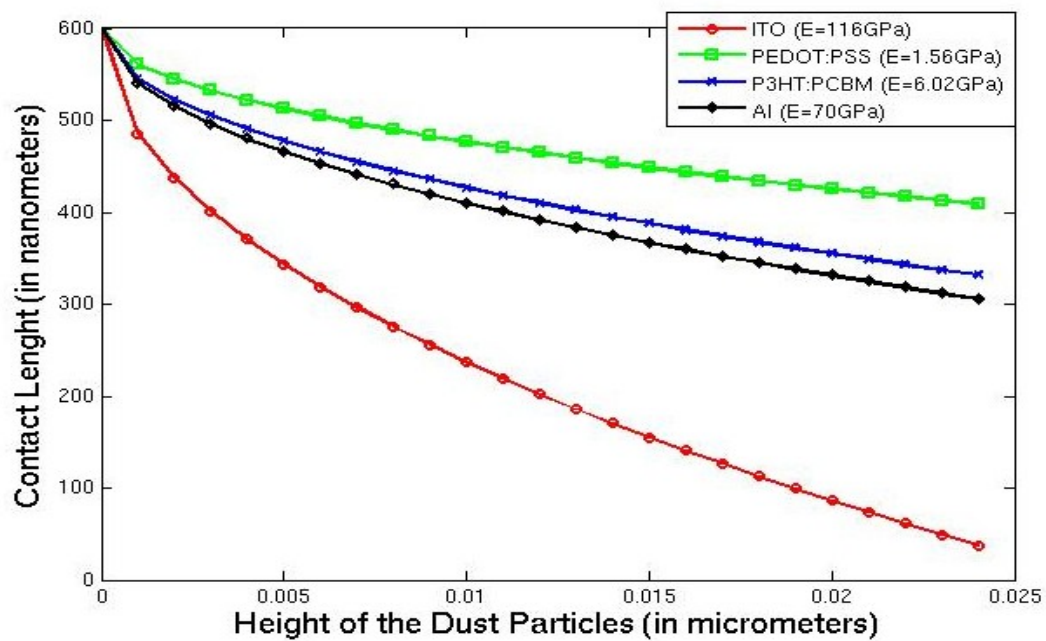


Figure 3.6b: Contact Length Versus Height of Dust Particles of Various Layers

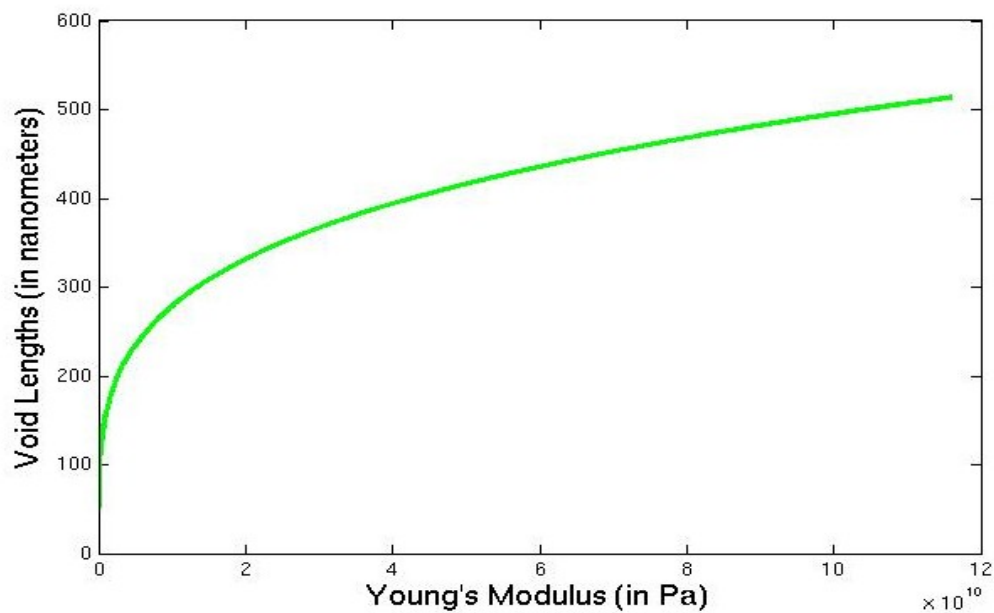


Figure 3.6c: Change in Void Length as a Function of Young's Modulus (0-116GPa)

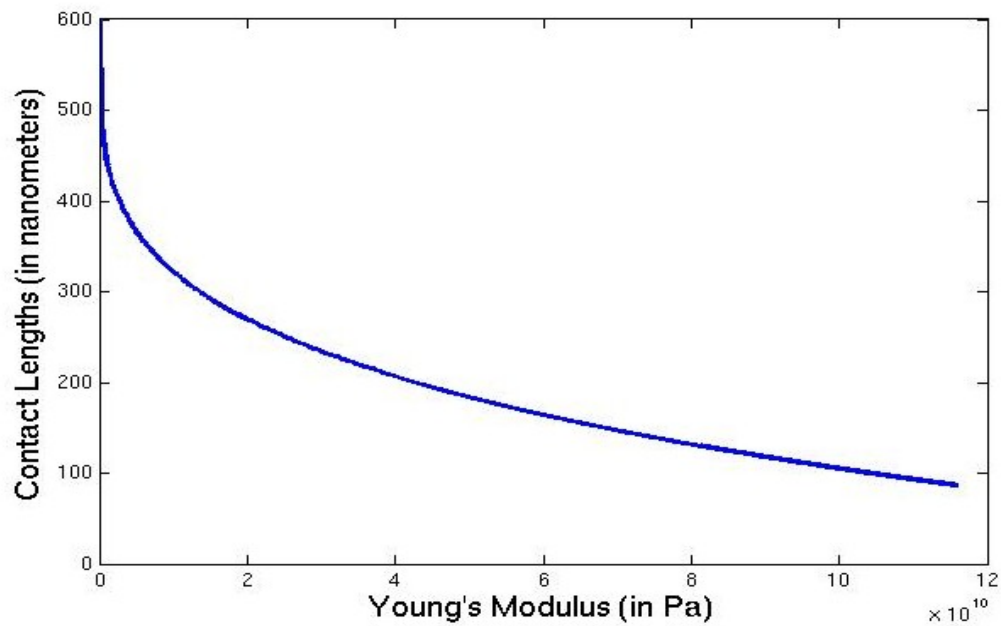


Figure 3.6d: Change in Contact Length as a Function of Young's Modulus (0-116GPa)

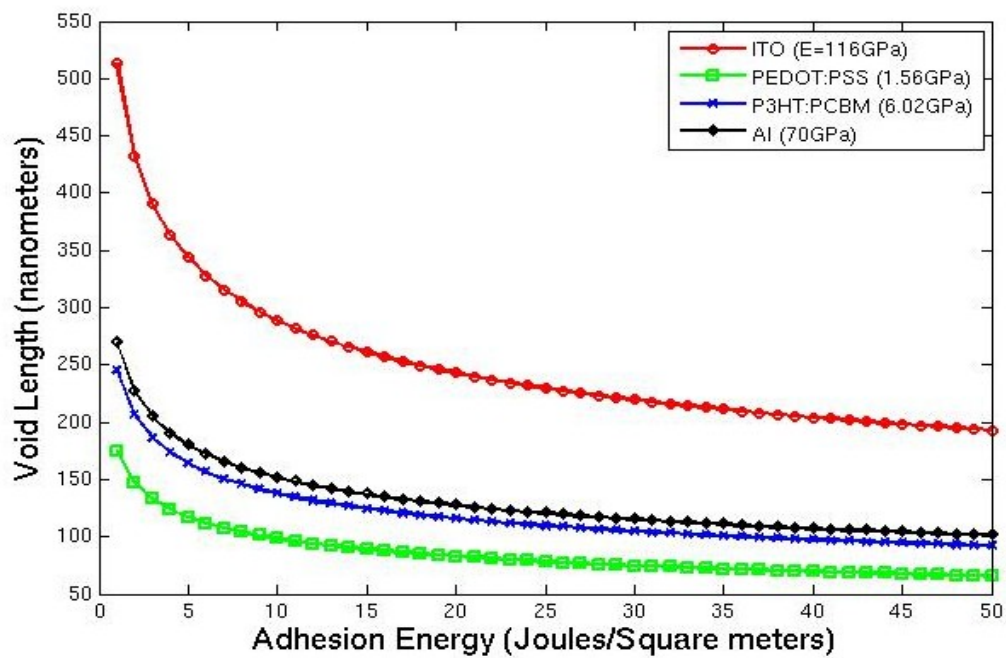


Figure 3.6e: Void Length as a Function of Adhesion Energy for Various Layers

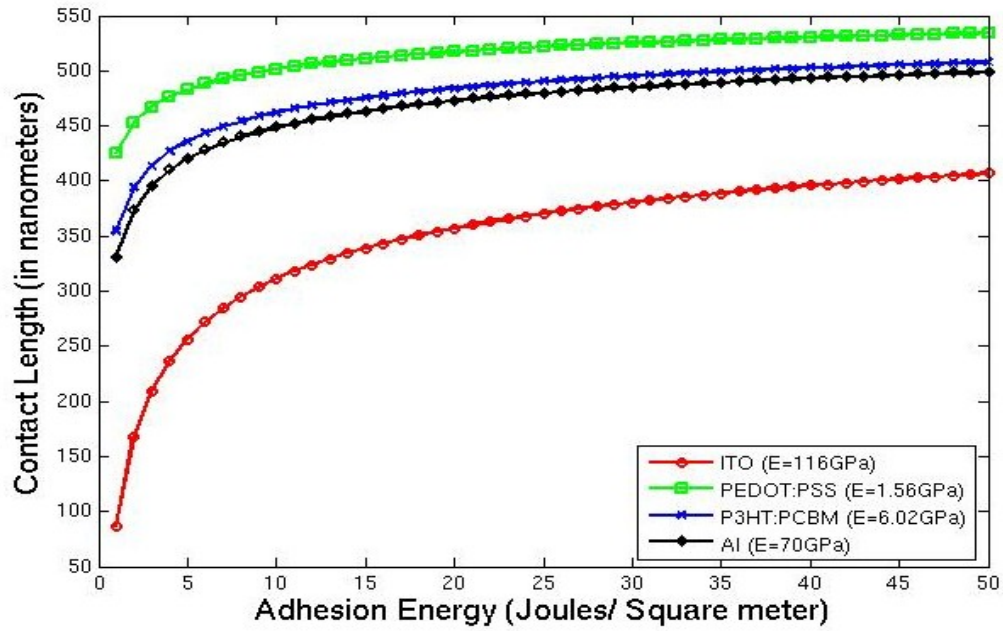


Figure 3.6f: Contact Length as a Function of Adhesion Energy for Various Layers

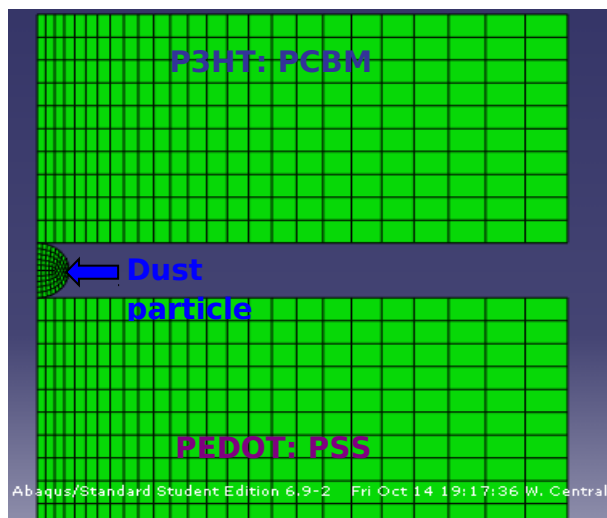
Increasing surface energy decreases the void lengths, as shown in Figure 3.6e. Also, for the actual layered structures that were examined in this study, the void lengths were increasing as the sizes of the dust particles increases, which invariably decreases the adhesion energies of the interfaces. This suggests that the layered structures of organic electronic adhere better when deposited in a clean room/glove boxes. Also, the efficiencies of the final fabricated devices depend on the adhesion of their interfacial structures. The contact lengths (Figures 3.6e and 3.6f) decreases with increasing Young's moduli and adhesion energies of the layered structures. The analytical results, therefore, suggest that materials with low Young's moduli are encourage for fabrication of stretchable

organic solar cells. This will help improve the interfacial adhesion which makes charge carriers to be transported across the layers.

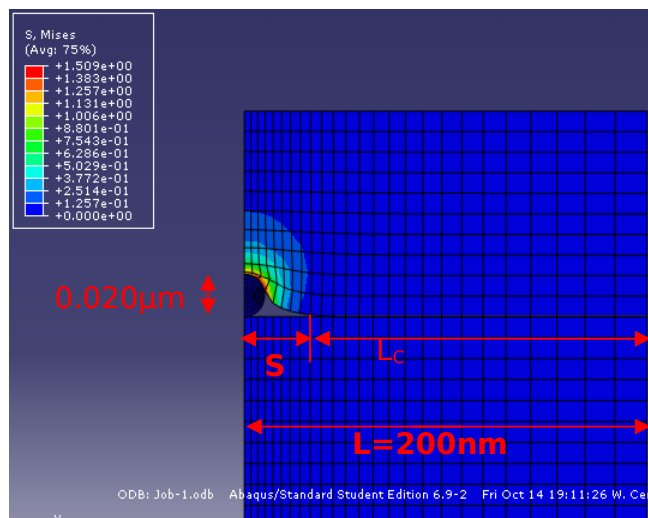
3.5.2 Finite Element Analysis of Contact Around dust Particles.

The finite element simulation of adhesion effects on the contact lengths was done by considering different sizes of dust particle. The interfaces of all the layers were considered for the simulations. The range of the heights of the dust particles used is 0.020-0.024 μm . The minute length, $L = 200\text{nm}$, was used while the thickness of each of P3HT:PCBM, PEDOT:PSS, and ITO is 100nm. The thickness of Aluminum is 50nm. We carried out the simulation for the dust particles of heights 0.02 μm , 0.022 μm , 0.23 μm , and 0.024 μm . The results of the simulations for different sandwiched dust particles between P3HT:PCBM and PEDOT:PSS are shown below in Figures 3.7 (a-e).

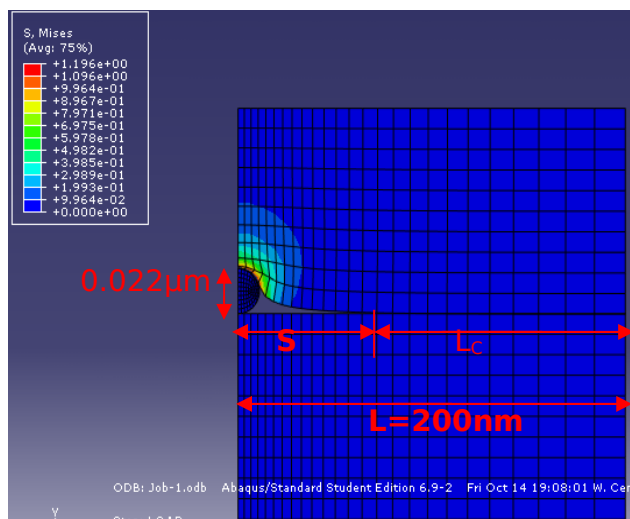
(a)



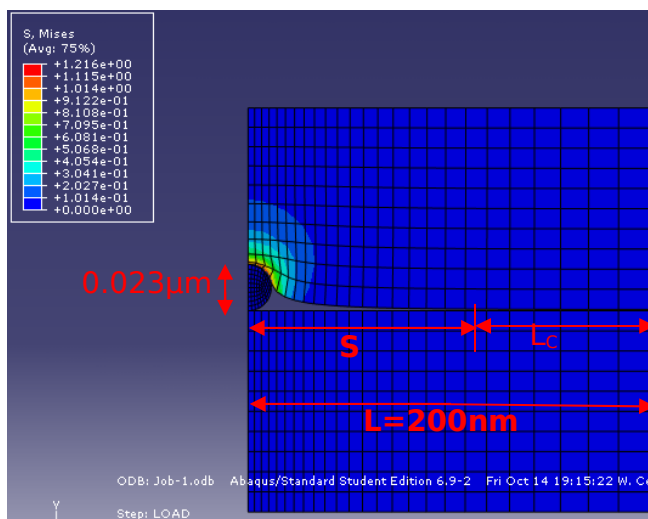
(b)



(c)



(d)



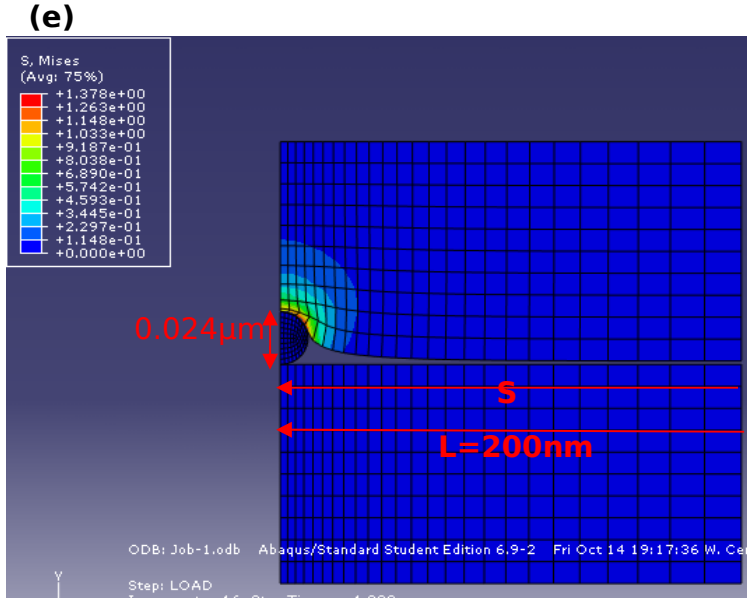


Figure 3.7: Finite Element Simulation of Contact Around Different Sizes of Dust Particle Sandwiched Between P3HT:PCBM and PEDOT:PSS Interface (a) Mesh Plot, (b) Height is 0.02μm, (c) Height is 0.022μm, (d) Height is 0.023μm, and (e) Height is 0.024μm.

From the results (Figures 3.7), the void length, S , increases with increasing height of the dust particles, which invariably reduces the contact length, L_c . The results of the simulations confirm the graph of void lengths versus heights of the dust particle obtained from the analytical modeling. This is, of course, an interesting result that must be taken into account when fabricating organic solar cells.

The finite element simulation has revealed significant results that are applicable to fabrication of organic electronic structures. Hence, the ratio of contact length to the length of the organic structure are expressed as functions

of some key variables (Figures 3.8 and 3.9) that are relevant to organic electronic structures. When the Young's moduli of layered structures tend to zero, the ratio L_C/L (normalized contact length) of each layer is a unity. However, the interfacial adhesion energies tend to infinity as the L_C/L increases to 1.

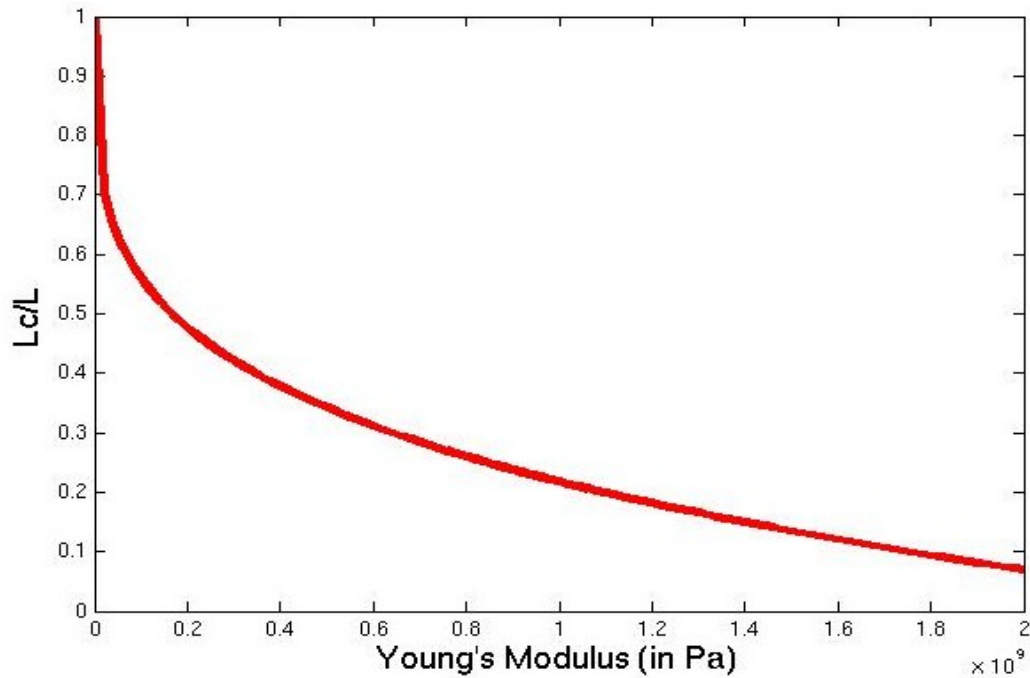


Figure 3.8: Variation of Ratio L_C/L as a Function of Young's Modulus

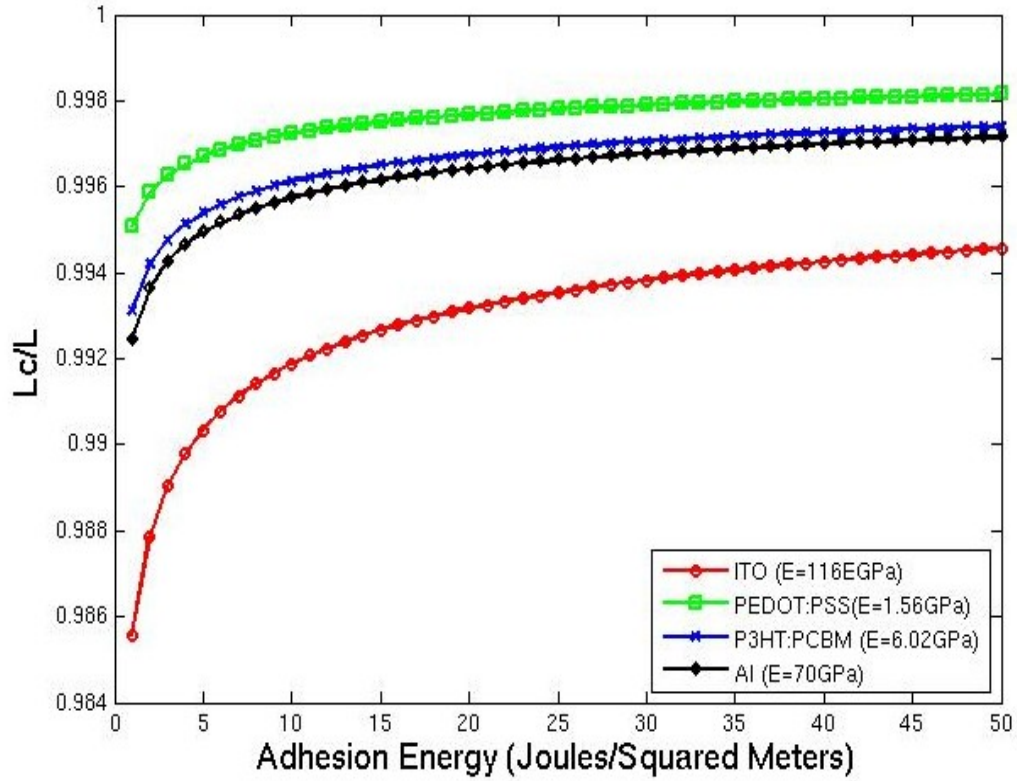
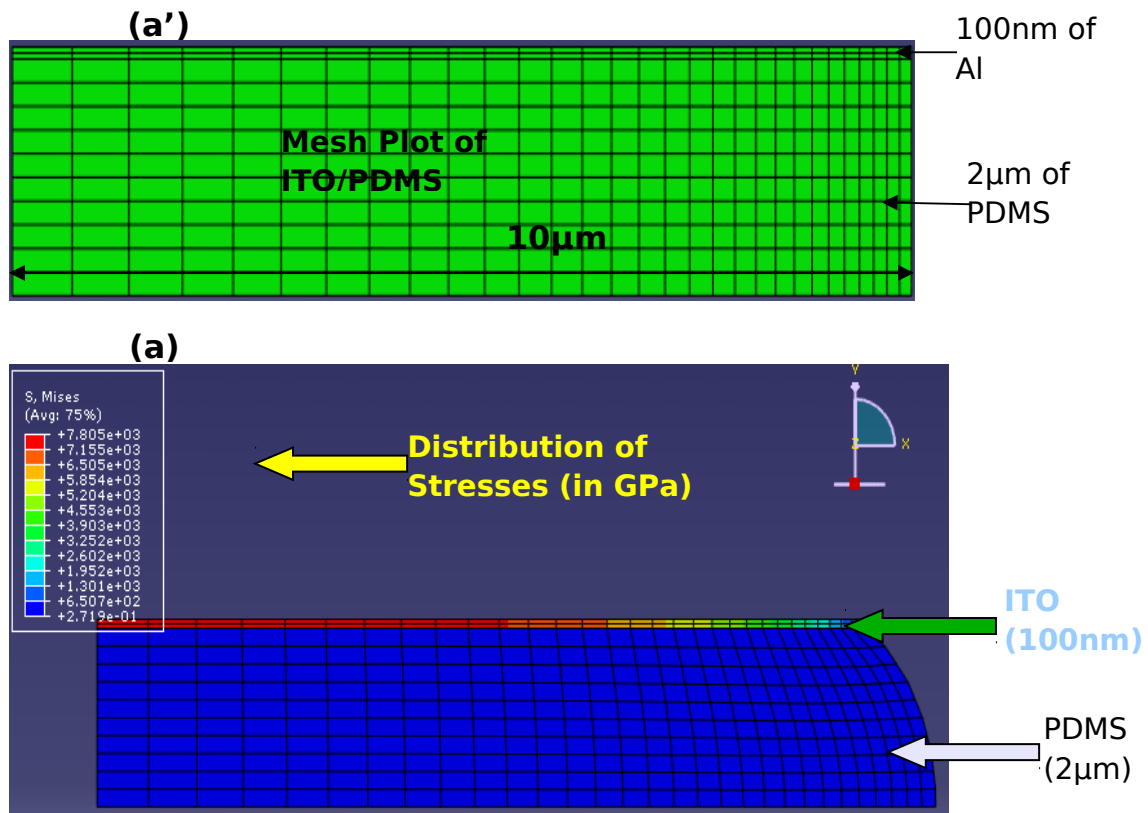


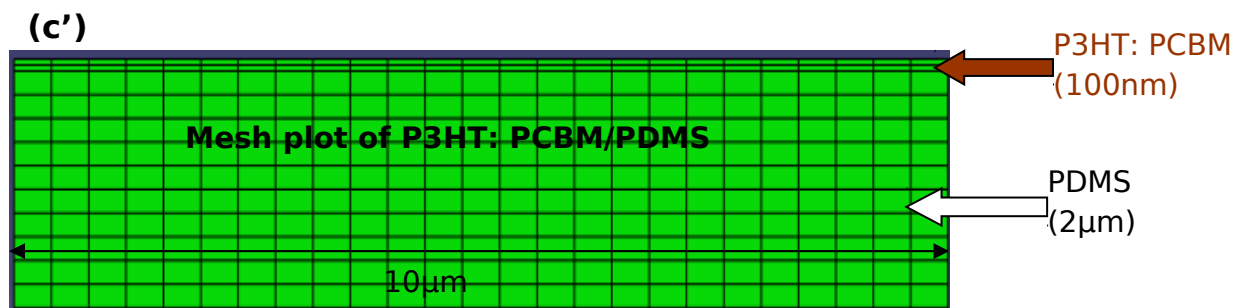
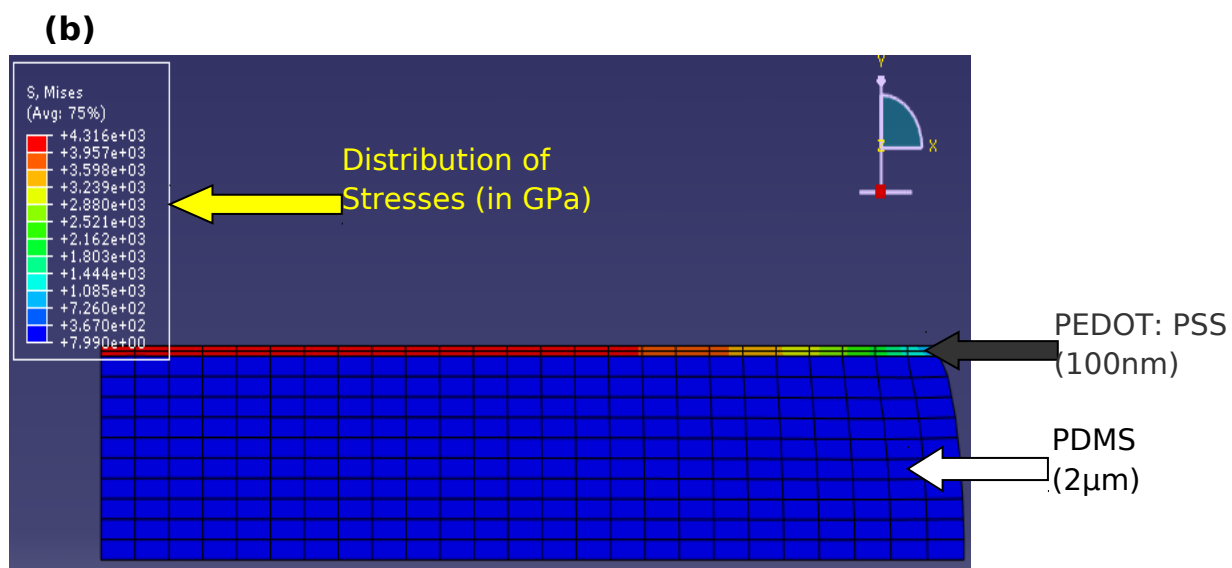
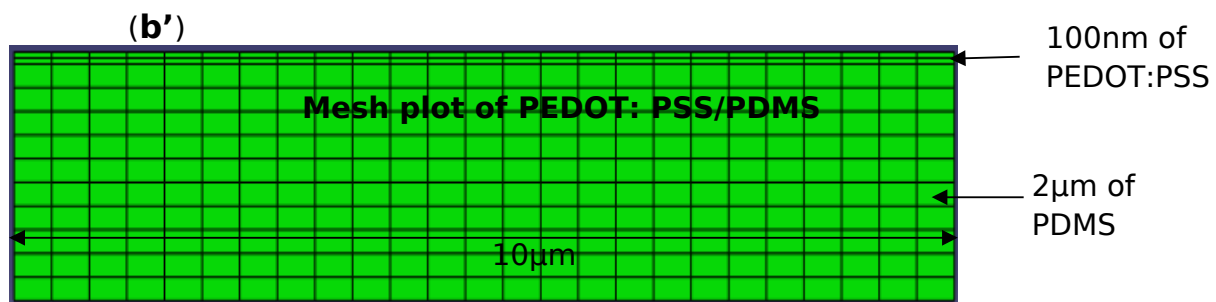
Figure 3.9: Variation of L_c/L as a Function of Adhesion Energy of Various Layers

3.5.3 Finite Element Simulations of Stretching of Thin Films of Stretchable Organic Solar Cells

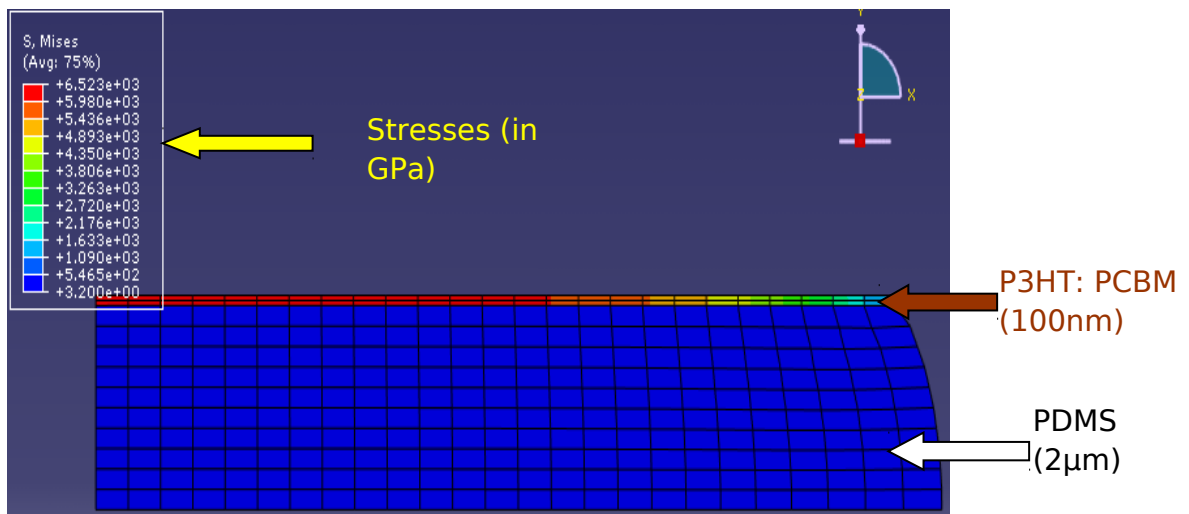
To understand the effects of stretching on the layers of stretchable organic solar cells better, the simulation of stretching of each of the layers on polymeric flexible substrate (PDMS) was carried out. The simulation was also performed on the whole structure of a typical organic solar cell. By using the mechanical properties of the layers in Table 3.1, an ABAQUS software package was used to

create and implement the model. 2D modeling space was used to show the thicknesses and the lengths of the layers. The thicknesses of the layers are as shown in the mesh plots in Figure 3.10 (a'-e'). The left hand surfaces were fixed while the top and lower surfaces were allowed to move on x-axis. Equal pressure (stress) was applied to the composite on the hand right surface in each of the cases. The distribution of stresses is shown below in Figure 3.10 (a-e).

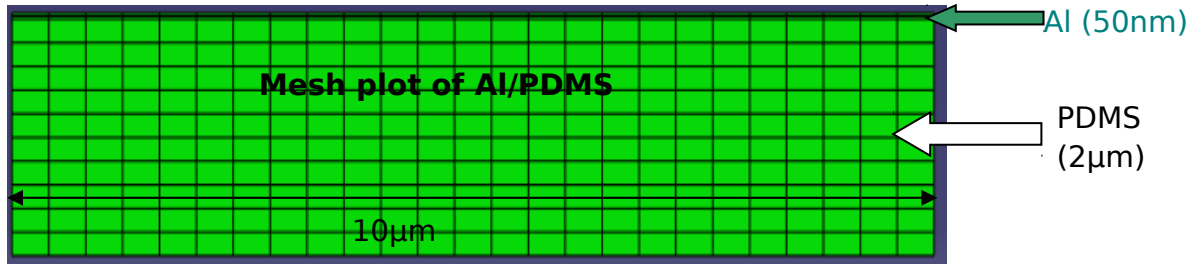




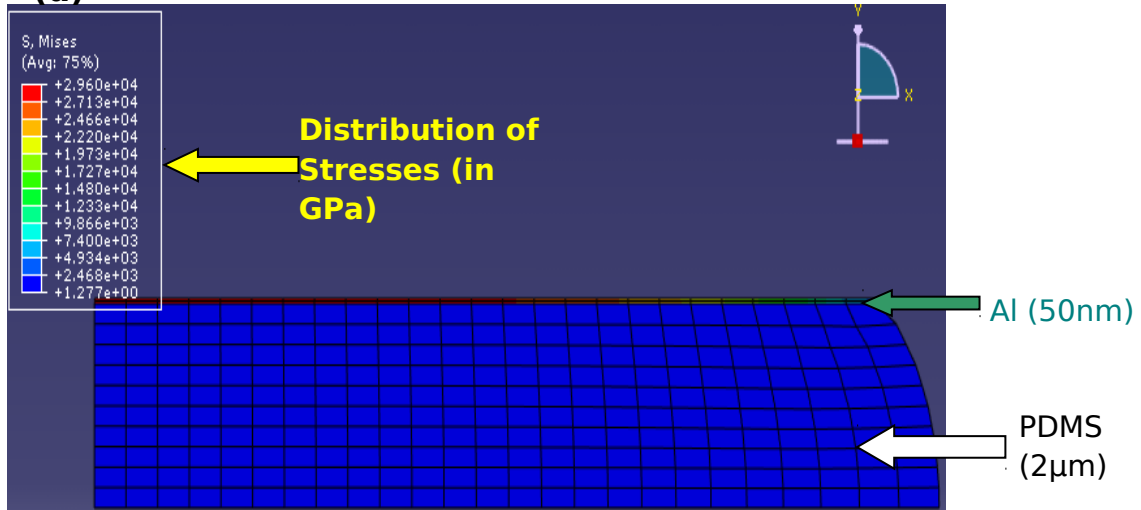
(c)



(d')



(d)



(e')

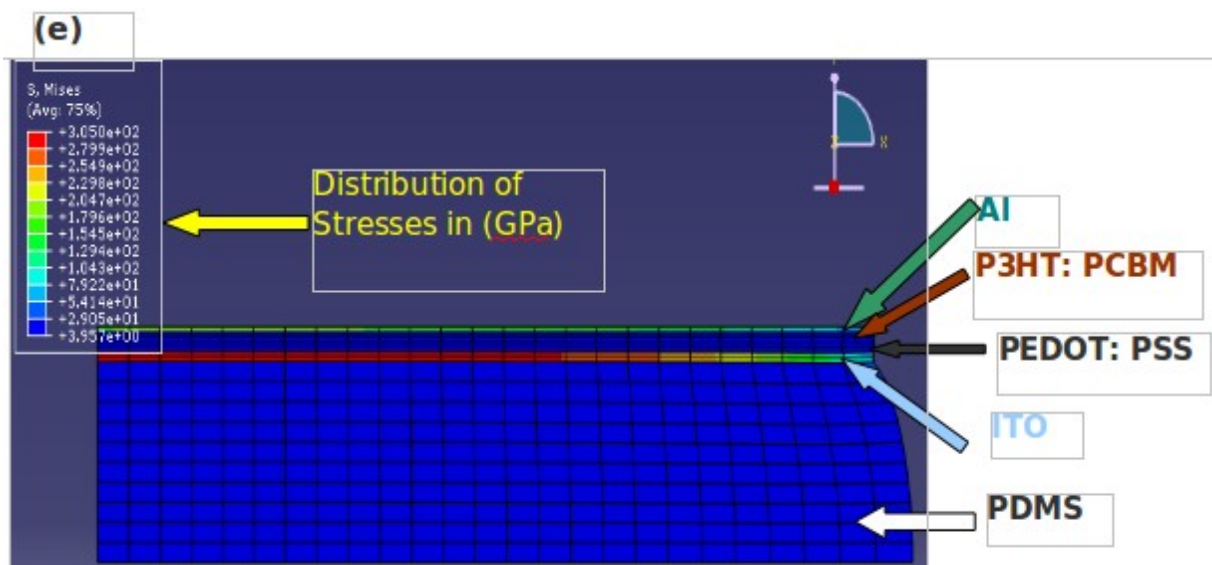
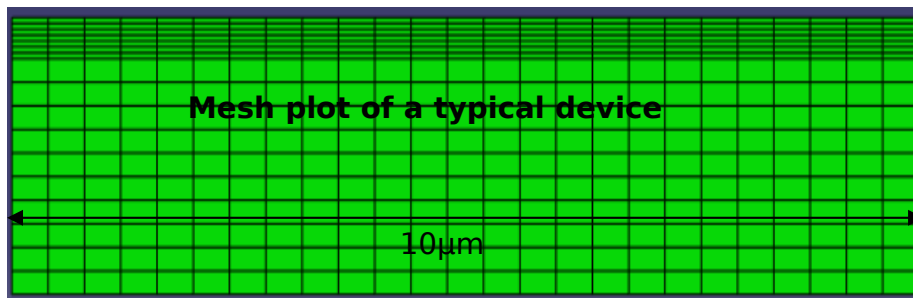


Figure 3.10: Mesh Plots of Interfaces (a' - e') and Distribution of Stress within the Interfaces (a - e) of a Typical Organic Solar Cell

The simulation reveals that stress is concentrated on the layer with high Young modulus. The simulation of tensile stress on interfaces between each of the layers and the flexible polymeric substrate (PDMS) helps us understand their

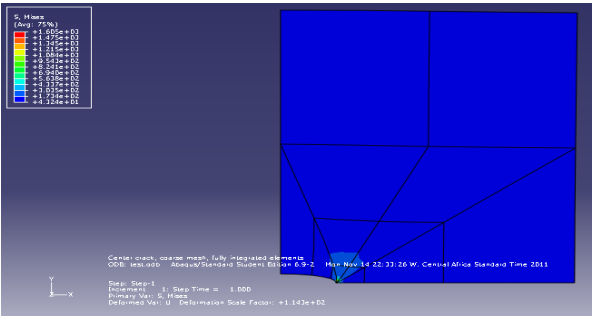
response to stretching. The region where stress is concentrated may experience delamination upon further application of stress. The layer with highest Young's modulus experienced more stress and was more likely to crack or delaminate first. From Figure 3.10e, the distribution of stress across the layers of a typical stretchable organic solar cell is not uniform. ITO experienced more stress followed by Aluminum cathode, while P3HT:PCBM/PEDOT:PSS interface experienced the least stress. It is therefore necessary to optimize ITO/PDMS and Al/PEDOT:PSS interfaces to know the threshold of the applied stress before damage begins to occur. This will also help us to avoid short circuiting and discontinuity in the final stretched devices.

3.5.4 Crack Driving Force

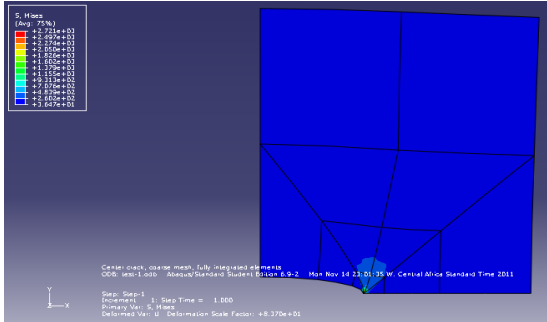
ABAQUS software package was also used to simulated a quarter of the thin film of the layers of stretchable solar cells in Figure 3.5 by taking the length, L , and the width, w , to be 20mm each. Stress of 10MPa was applied to the layers as shown in Figure 3.5 along with their material properties. The energy release rates were calculated for each of the crack lengths used.

The results of of the simulation are shown below in Figures 3.11. 3.12, 3.13, and 3.14 for ITO, PEDOT:PSS, P3HT:PCBM, and Al layers, respectively. The results reveal that increasing crack length in thin films increases the energy release rate. The energy release rate also increases as the Young's modulus of

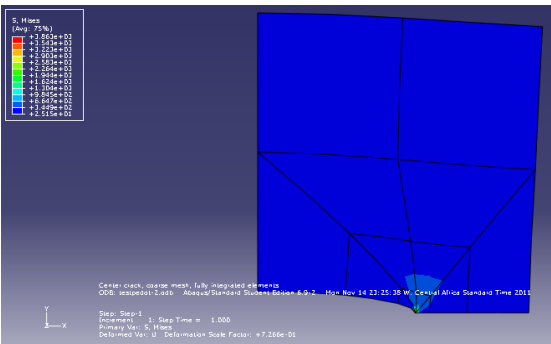
the layers reduces. The distribution of stresses increases as cracks penetrate the layers of the structures.



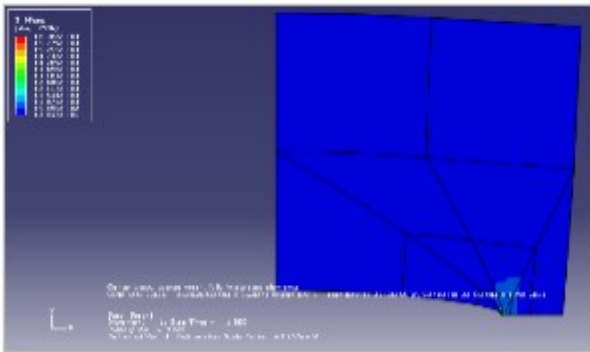
A: Crack length=2mm



B: Crack length=4mm



C: Crack length=6mm



D: Crack length=8mm

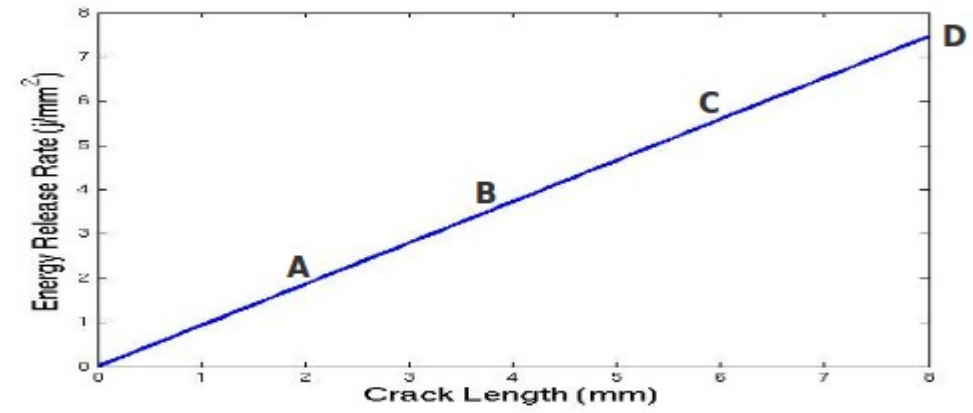
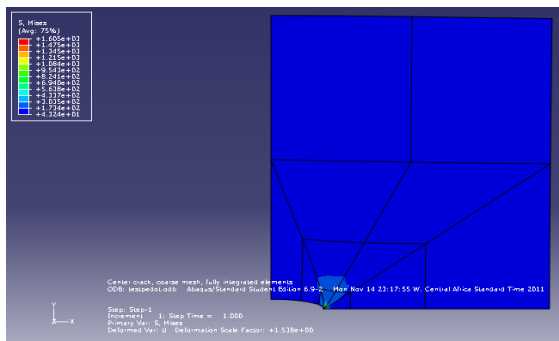
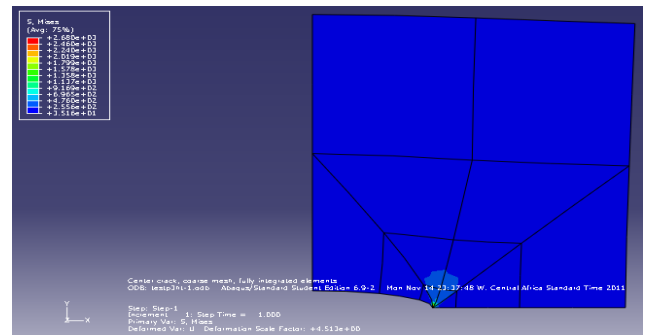


Figure 3.11 : Energy Release Rate Versus Crack Length and Stress Distribution as Crack Penetrate Across ITO Layer



A: Crack length=2mm



B: Crack length=4mm

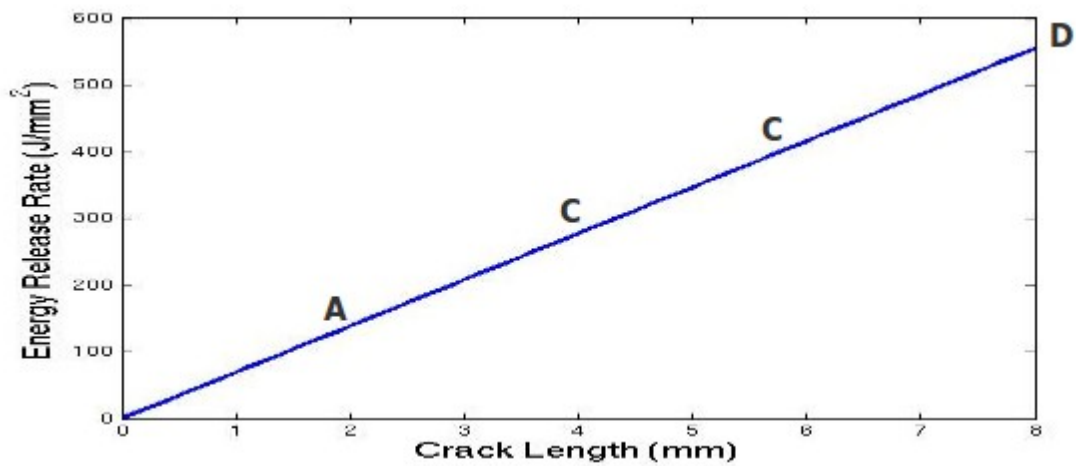
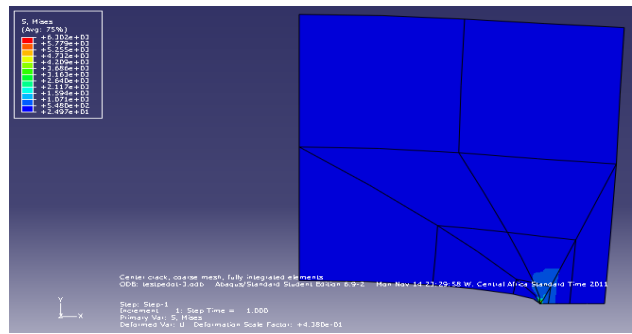
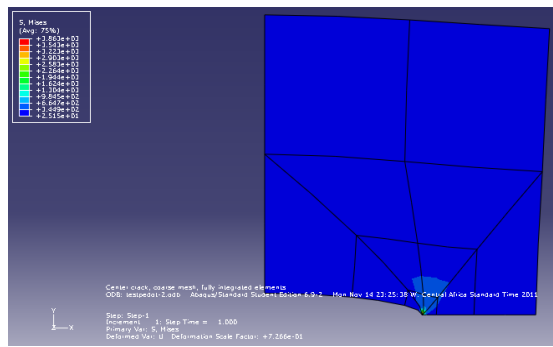
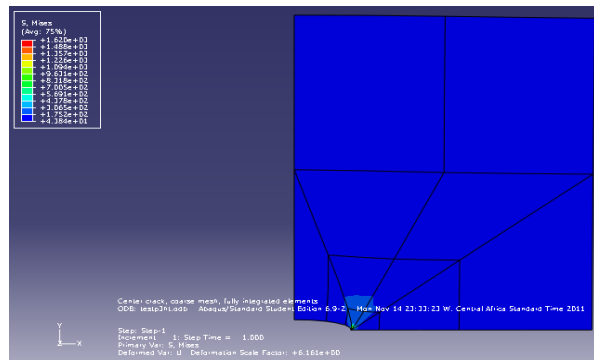
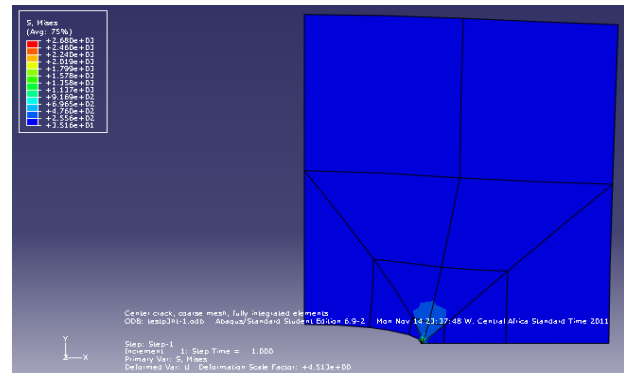


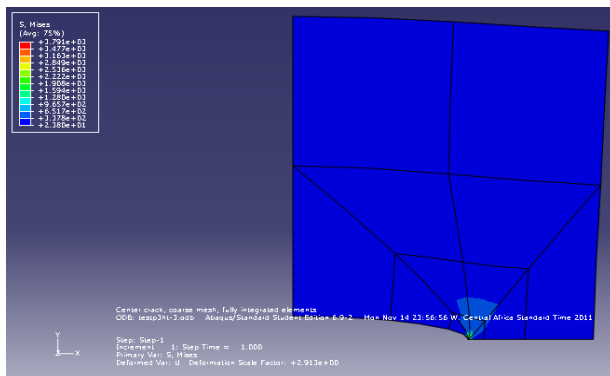
Figure 3.12:Energy Release Rate Versus Crack Length and Stress Distribution as Crack Penetrate Across PEDOT:PSS



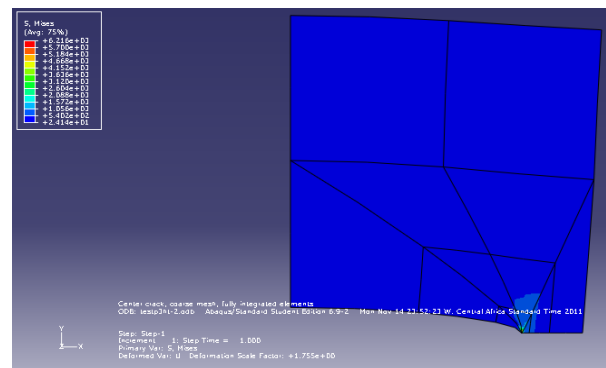
A: Crack length=2mm



B: Crack length=4mm



C: Crack length=6mm



D: Crack length=8mm

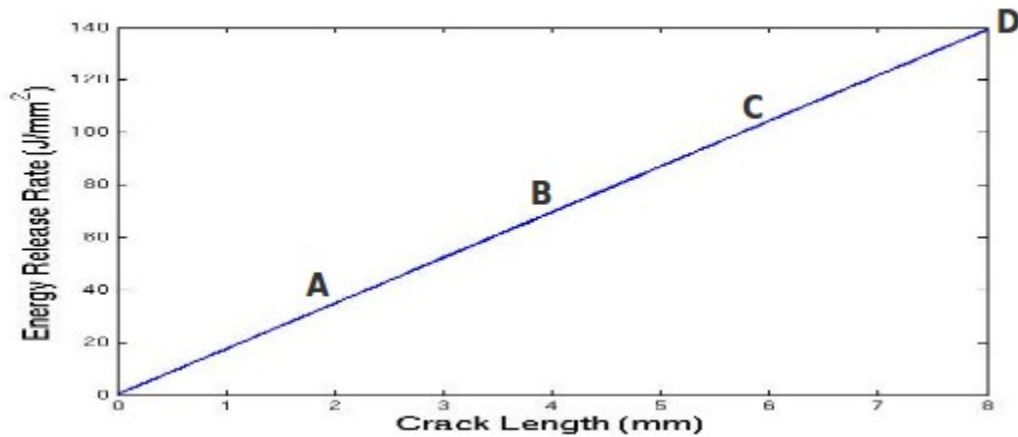
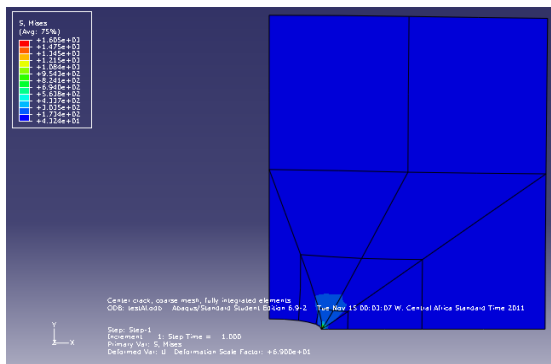
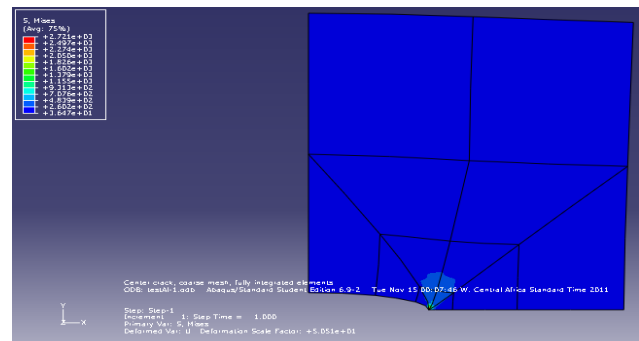


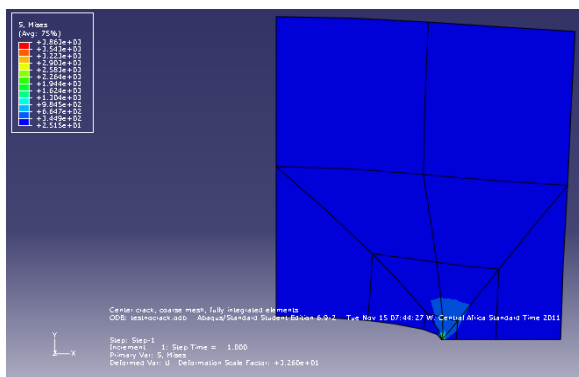
Figure 3.13: Energy Release Rate Versus Crack Length and Stress Distribution as Crack Penetrate across P3HT:PCBM Layer



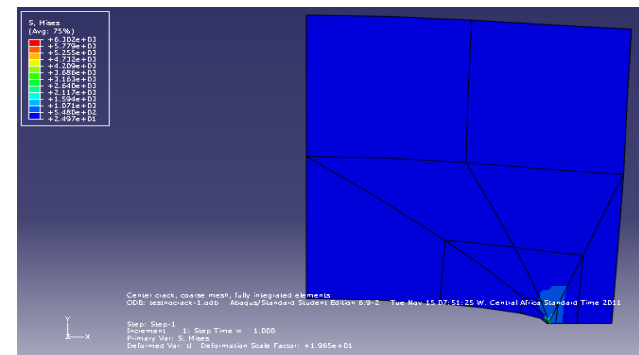
A: Crack length=2mm



B: Crack length=4mm



C: Crack length=6mm



D: Crack length=8mm

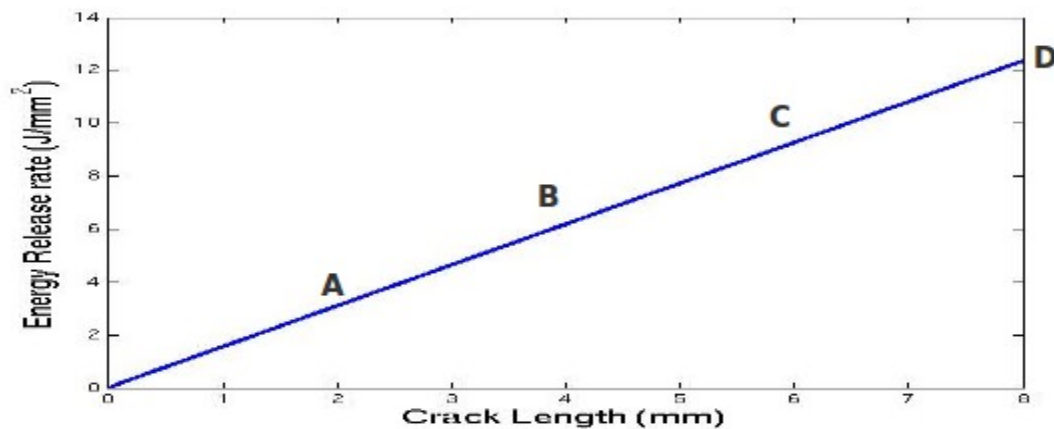


Figure 3.14: Energy Release Rate Versus Crack Length and Stress Distribution as Crack Penetrates Across Al Layer

In summary, the values of energy release rate that correspond to each of the cracks of the layered structures as shown in Table 3.2.

Table 3.2: Summary of the Energy Release Rate for each of the Cracks Lengths

Crack Length (mm)	G (J/mm²) for ITO	G (J/mm²) for PEDOT:PSS	G (J/mm²) for P3HT:PCBM	G (J/mm²) for Al
2	0.57	42.71	10.67	0.95
4	1.47	109.32	27.37	2.43
6	3.21	239.22	59.85	5.33
8	7.46	554.75	139.09	12.36

3.6 CONCLUSION

This chapter has presented the results obtained from modelling of effects of adhesion on contact lengths and deformation induced across interfaces that are relevant to stretchable organic solar cell. It was found that increasing adhesion increases the contact lengths across the interfaces of the studied stretchable solar cell. This was confirmed by both analytical modelling and numerical simulations. The study revealed, however, that in the presence of dust particles, the contact lengths at the interfaces reduces which invariably reduces the adhesion. Moreover, The stresses experienced by the layers of the stretchable organic solar cell depends on their Young's modulus.

3.7 REFERENCES

- [1] J. Ralston I. Larson, M. W. Rutland, A. A. Feiler and M. Kleijn: *atomic force microscopy and direct surface force measurements*, *Pure Appl. Chem.*, Vol. 77, No. 12, pp. 2149–2170, 2005.
- [2] T. Tong, B Babatope, S. Admassie, J. Meng, O. Akwogu, W. Akande and W. O. Soboyejo: *Adhesion in Organic Structures*, *Journal of Applied Physics* 106, 083708 (2009).
- [3] J. M. Neumeister and W. A. Ducker. *Rev. Sci. Instrum.* **65**, 2527 (1994).
- [4] J. E. Sader, I. Larson, P. Mulvaney, L. R. White. *Rev. Sci. Instrum.* **66**, 3789 (1995).
- [5] J. E. Sader. *Rev. Sci. Instrum.* **66**, 4583 (1995).
- [6] O. Akogwu, D. Kwabi, A. Munhutu, T. Tong, and W. O. Soboyejo: *Adhesion and cyclic stretching of Au thin film on poly(dimethyl-siloxane) for stretchable electronics*, *Journal of Applied Physics*, 108, 123509 (2010)
- [7] K. L. Johnson, K. Kendall and A. D. Roberts: *Surface energy and the contact of elastic solids*, *Proc. R. Soc. Lond. A.* 324, 301-313 (1971)
- [8] B. V. Derjaguin and V. M. Muller and Y. P. Toporov: *Effect of contact deformations on the adhesion of particles*, *J. Colloid Interface Sci.* 53 (1975) 314–325.
- [9] O. Pi´etrement and M. Troyon: *General Equations Describing Elastic Indentation Depth and Normal Contact Stiffness versus Load*, *Journal of Colloid and Interface Science* **226**, 166–171 (2000)
- [10] Wole Soboyejo: *Mechanical Properties for Engineered Materials*, Marcel Dekker, Inc., pp105-115 (2003)
- [11] A.G. Evans and J.W. Hutchinson: *The Thermomechanical Integrity of Thin Films and Multilayers*, *Acta metal. Mater.* Vol. 43. No 7, pp. 2507-2530, 1995.
- [12] Wali O. Akande, Yifang Cao, Nan Yao, and Wole Soboyejo: *Adhesion and the Cold Welding of Gold –Silver Thin Films*, *Journal of Applied physics* 107, 043519 2010.
- [13] A. Bietsch and B. Michel: *J. Appl. Physics.* 88, 4310 2000
- [14] D. G. Neerincx and T. J. Vink,: *Thin Solid Films*, 1996, 278,12

- [15] D. Tahk, H. H. Lee, N. Y. Khang: *Macromolecules*, 2009, 42, 7079
- [16] D. Choi, K. Y. Lee, Mi-Jin Jin, Soo-Ghong Ihn, S. Yun, X. Bulliard, W. Choi, S. Y. Lee, Sang-Woo Kin, Jae-Young Choi, J. Min Kim and Z. L. Wang: *Electronic Supplementary Science*, The Royal Society of Chemistry 2011.
- [17] Z. Suo and J. W. Hutchinson, *Materials Science and Engineering: A* 107, 135-143 (1989).
- [18] C. Atkinson, R. E. Smelser, and J. Sanchez, *International Journal of Fracture* 18, 279-291 (1982)
- [19] A. Rohatgi, *NREL 15th Workshop on Crystalline Silicon Solar Cells and Modules* (2005) 11-12
- [20] J.A. Greenwood, "Adhesion of Elastic Spheres". *Proc. R. Soc. Lond. A* (1997) 453, 1277-1297
- [21] K. L. Johnson and K. Kendall and A. D. Roberts: *Surface energy and the contact of elastic solids*, *Proc. R. Soc. Lond., A* 324 (1971) 301-313.
- [22] B. V. Derjaguin and V. M. Muller and Y. P. Toporov: *Effect of contact deformations on the adhesion of particles*, *J. Colloid Interface Sci.* 53 (1975) 314-325.
- [22] D. Maugis and M. Barquins and R. Courtel, *M'iaux: Corrosion, Industrie* 605 (1976) 1.
- [23] D. S. Grierson, E. E. Flater and R. W. Carpick: *Accounting for the JKR-DMT transition in adhesion and friction measurements with atomic force microscopy*, *J. Adhesion Sci. Technol.*, Vol. 19, No. 3-5, pp. 291- 311 (2005).

CHAPTER 4

EXPERIMENTAL STUDY OF EFFECTS OF STRETCHING ON OPTICAL PROPERTIES AND MECHANICAL FAILURE OF LAYERS OF FLEXIBLE ORGANIC SOLAR CELLS

4.1 Introduction

This chapter explores the experimental method of studying the effects of stretching on optical properties and failure mechanism of layers of stretchable solar cells. This involves fabrication of each of the layers of stretchable organic solar cells (from the poly di-methyl siloxane (PDMS) substrate to the aluminum cathode) and studying their responses to tensile force. The PDMS substrate was fabricated and characterized before subsequent layers were deposited on it and characterized.

Following the introduction (section one), the experimental procedures for the fabrication of PDMS and deposition of layers of organic solar cell are presented in section two. Section three explores the characterization of PDMS and layers of organic solar cells (OPV). This includes the interfacial adhesion measurement of the layered structures. The experimental results and discussion are summarized in section four.

4.2 Fabrication of Stretchable Solar Cells

The schematic diagram of steps involved in the fabrication of layers of a single stretchable organic solar cell is shown below in Figure 4.1. The PDMS cured in glass mold was used as a substrate for the fabrication.

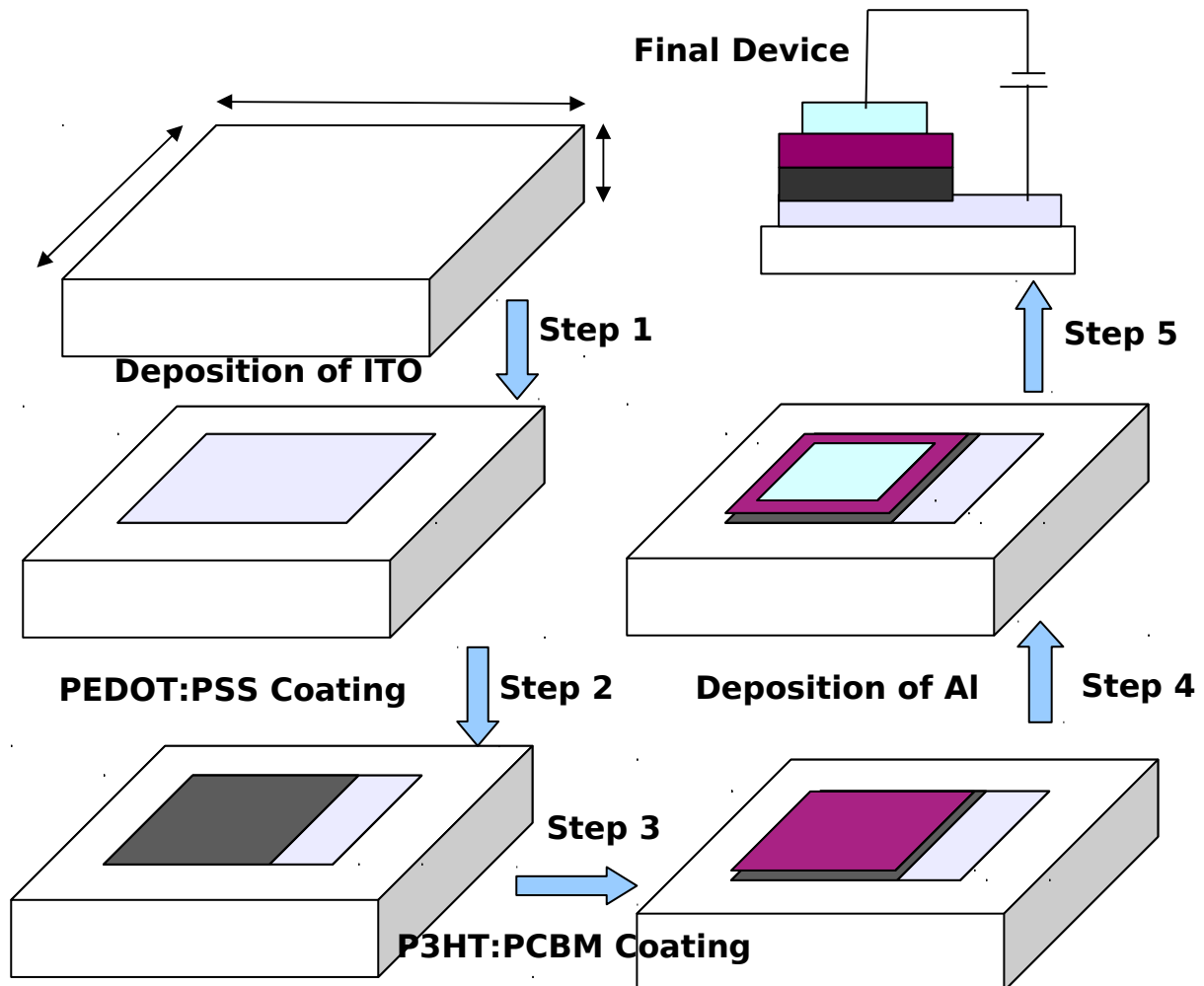


Figure 4.1: Schematic of Steps Involved in the Fabrication of a Stretchable Solar Cell

4.2.1 Fabrication of PDMS Substrates

The following equipments were used for the fabrication of the PDMS:

- i Vacuum oven
- ii Pipette
- iii Slygard 184 (Base and curing agent)
- iv Graduated plastic beaker
- v Molds

Slygard 184 base was poured into the graduated beaker before slygard 184 curing agent (1/10 of the base) was measured with pipette into it. The mixture was stirred vigorously using a disposable stir rod. The mixture was degassed in a vacuum oven for 60min until all the bubbles were cleared to form PDMS. The vacuum gauge level was above 15 inch/Hg at 0°C. The PDMS was gently poured into the glass and Aluminum molds until their cavities were filled up. PDMS was degassed further to ensure that no bubble was trapped when curing. The PDMS was then kept on a leveled surface to cure at different temperatures (70°C for 60min, 100°C for 45min, 125°C for 25min, and room temperature for 3days). The room temperature of the Laboratory used was in a range of 27 - 37°C. The cured PDMS was then pilled off the substrate and ready for use.

4.2.2 Deposition of ITO on PDMS

This is the step 2 of the fabrication process as shown in Figure 4.1 above. PDMS substrates each of dimension 25mm x 25mm x 1mm were placed on the substrate holder and loaded in the chamber of an Edwards Auto 306 13.56 MHz radio frequency (RF) magnetron sputtering system, with 99.99% $\text{In}_2\text{O}_3:\text{SnO}_2$ ceramic target. The shadow mask used is as in Figure 4.2.

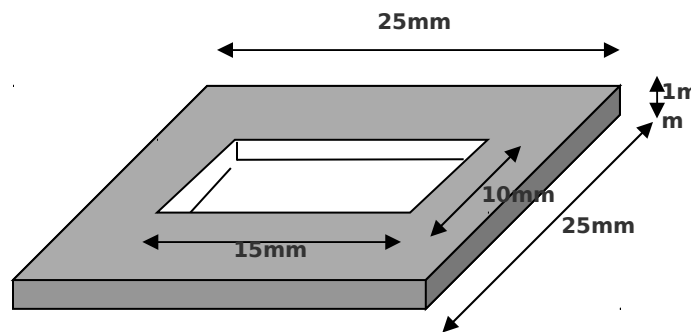


Figure 4.2 : Shadow Mask for ITO Deposition

First, the system was evacuated to 2.0×10^{-5} before Argon gas was introduced into the system to excite ions on the ITO target. The system was operated at RF power of 60W with deposition vacuum pressure that was maintained at an average value of 3.2×10^{-3} Torr. Indium-tin-oxide of thickness 100nm was sputtered unto the PDMS substrate at room temperature ($27^\circ\text{C} - 32^\circ\text{C}$). The deposition process lasted for 70 minutes at an average deposition rate of $0.6\text{\AA}/\text{s}$. The parameters used for the deposition are summarized in Table 4.1. The set-up for the deposition is as in Figure 4.3. The ITO-coated PDMS substrates were then removed from the chamber for characterization and deposition of other layers.

Table 4.1: ITO Sputtering Parameters

Residual pressure	2.0×10^{-5} Torr
Substrate temperature	Room temperature (27°C-32°C)
RF power	60W
Deposition pressure	3.2×10^{-5} Torr
Deposition rate	0.6Å/s



Figure 4.3: Edwards Auto 306 Sputtering System Set Up

4.2.3 Deposition of Thin Film Layer of PEDOT:PSS on Glass Slide and ITO-Coated PDMS

Deposition of PEDOT: PSS onto ITO-coated PDMS is the third step of the fabrication process (Figure 4.1). The following materials and equipments were used for depositing PEDOT:PSS on both plane glass slide and ITO-coated PDMS substrates:

- i PEDOT:PSS solution
- ii 0.2 μ m mesh size filter
- iii 2ml syringes
- iv Laurell Spin Coater (WS-650HZ Model)
- v PDMS and ITO-coated PDMS
- vi glass slides of the same dimension as PDMS substrates
- vii dry – clean beakers

The PEDOT: PSS solution was filtered through a 0.2 μ m mesh size filter into a beaker. The Laurell spin coater was set to 2 step program. The first step was set to spread the dispensed solution for 10 seconds with a moderate speed of 200 rpm. The high speed of 1000 rpm in the second step thins and dry the solution of the PEDOT:PSS for 40 seconds.

The PEDOT:PSS was first optimized on plane glass slides until 90nm thickness was achieved. PDMS substrate were attached to plane glass slides of the same dimension to avoid sinking of the flexible PDMS substrates in the vacuum chuck of spin coater. The PDMS substrate on glass slide was placed on the chuck and the PEDOT:PSS of 90nm

thickness was deposited on it. The PEDOT:PSS was baked for 5min at 70°C on a hot plate.

4.2.4 Deposition of Thin Film Layer of P3HT:PCBM on Glass Slides and on PEDOT:PSS/ITO-Coated PDMS

First, 1 wt % concentration of ratio 1:1 blend of P3HT:PCBM was prepared by mixing 11.11mg/ml of P3HT and 11.11mg/ml of PCBM together. The mixture was stirred for 12hours at a temperature of 50°C. The estimation of masses of P3HT and PCBM is as follows:

$$\text{Volume of the solvent (Chlorobenzene)} = 4.5\text{ml}$$

$$\text{Density of the Chlorobenzene} = \frac{\text{mass}}{\text{volume}} = 1.11\text{g/ml}$$

$$\text{mass of the Chlorobenzene} = 4.5 \times 1.11 = 4.995\text{g}$$

Since the mass of Chlorobenzene is 99 percent of the entire solution expected, then

$$\text{mass of the entire solution} = \frac{100}{99} \times 4.995 = 5.045\text{g}$$

$$\text{mass of 1 P3HT : PCBM} = 5.045 - 4.995 = 0.0504\text{g}$$

For ratio of P3HT : PCBM, mass of P3HT = mass of PCBM, therefore

$$\text{mass of P3HT} = \text{mass of PCBM} = 0.5 \times 0.0504 = 25\text{mg}$$

This means that 25mg of P3HT must be dissolved required 2.25ml of solvent

This can be written as 11.11mg /ml of P3HT . This is the same for PCBM

The solution of P3HT:PCBM blend was first optimized on plane glass for a thickness of 100nm before spin coating it on PEDOT:PSS/ITO-coated PDMS using 1500rpm for 45min. This process is the step 4 of the fabrication process(as shown in Figure 4.1).

4.2.5 Vacuum Thermal Deposition of Al Cathode

The following materials and equipments were used for the deposition of cathodic Aluminum layer:

- i 99.99% pure Aluminum pellets
- ii vacuum thermal Evaporator
- iii shadow mask (Figure 4.4)

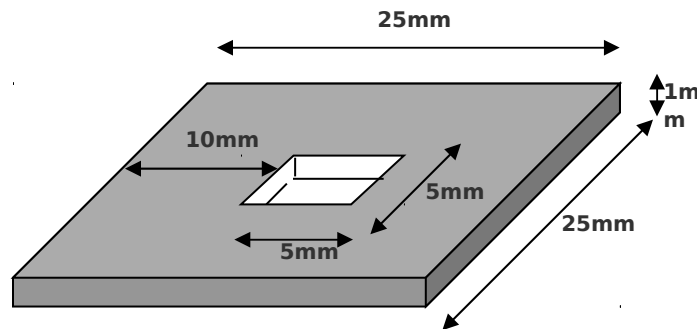


Figure 4.4: Shadow Mask for Deposition of Aluminum Cathode

This is the step 5 of the fabrication process (as in Figure 4.1). A 99.99% pure Aluminum rod of radius 1mm and length 15mm was placed on the Tungsten filament in the chamber of the thermal evaporator. A thin film layer of Aluminium of 150nm thickness

was deposited on glass slide and P3HT:PCBM/PEDOT:PSS/ITO-coated PDMS at a low vacuum pressure of 2.0×10^{-5} Torr. The thickness of the Aluminum thin film was measured using an Infinicon Thin Film Controller and later confirmed by using Veeco Dektak 150 Surface Profiler. The set-up of the system is shown below in Figure 4.5.

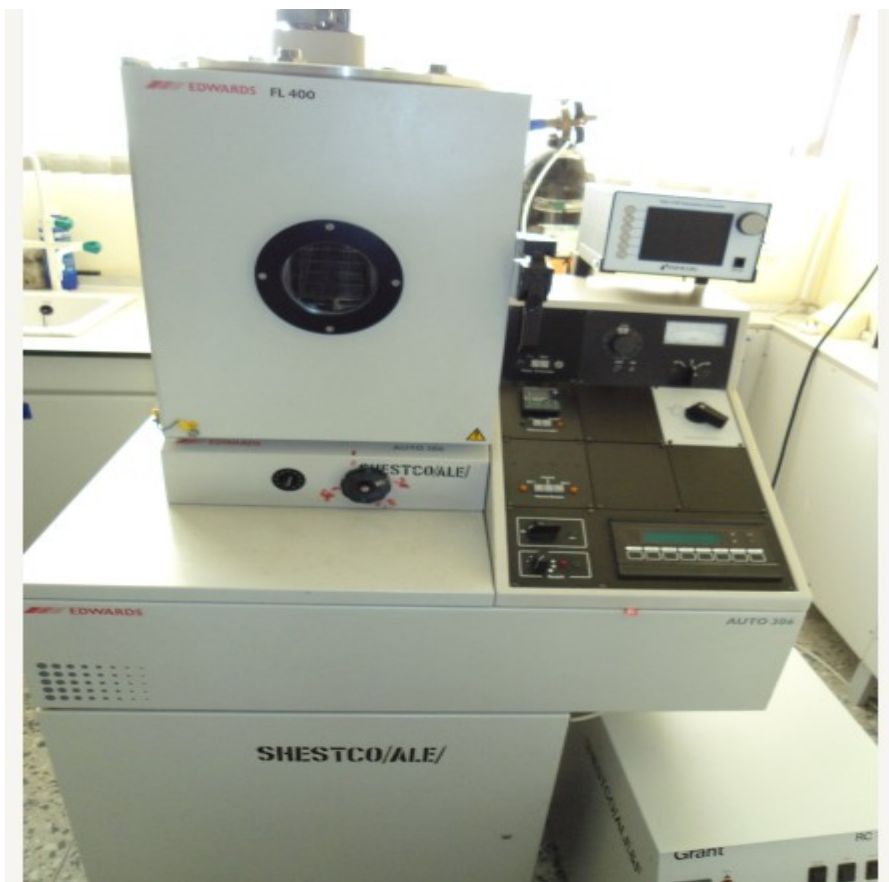


Figure 4.5: Edwards Auto 306 Thermal Vacuum Evaporator

4.3 MATERIALS CHARACTERIZATION

The following samples were prepared for characterization:

sample A: PDMS cured at room temperature in glass mold

sample B: PDMS cured at 70°C in glass mold

sample C: PDMS cured at 100°C in glass mold

sample D: PDMS cured at 125°C in glass mold

sample A': PDMS cured at room temperature in Aluminum mold

sample B': PDMS cured at 70°C in Aluminum mold

sample C': PDMS cured at 100°C in aluminum mold

sample D': PDMS cured at 125°C in Aluminum mold

sample E: ITO-coated PDMS substrate

sample F: PEDOT:PSS/ITO-coated PDMS

sample G: P3HT:PCBM/PEDOT:PSS/ITO-coated PDMS

sample H: Al/P3HT:PCBM/PEDOT:PSS/ITO-coated PDMS

4.3.1 Measurement of Stress-Strain

The mechanical tensile test was carried out on PDMS substrates (samples A, B, C, and D). A schematic of the rectangular shaped of each of the samples is shown in Figure 4.6. Each of the samples was mounted in between the jaws of the universal tensile machine (TIRA test 2810) as shown in Figure 4.7. The test was carried out at strain rate 10mm/min. A precision load cell measured the force on the sample while the motion of the cross - head measured the extension on the sample. The stress on the samples was

thus calculated using the fact that stress is force per cross-sectional area. Also, strain is extension per original length. The same tensile test was done on samples E – H before extracting the stress-strain data of each of the deposited thin films using the earlier model that was developed in chapter 3 (equation 3.21b) of this thesis.

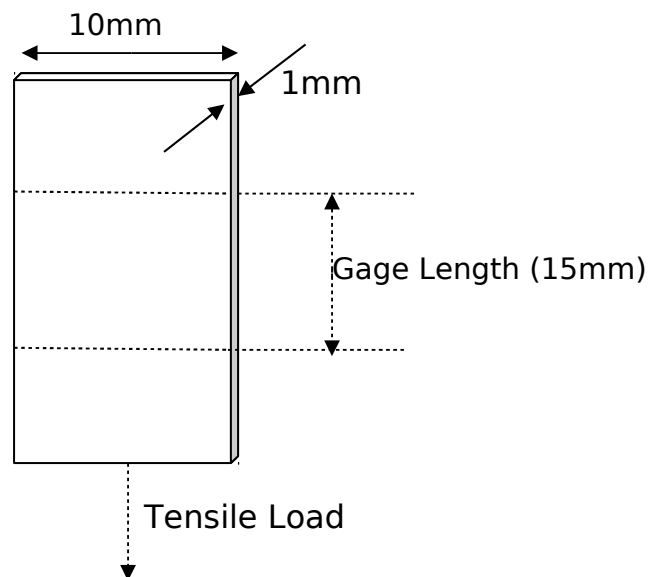


Figure 4.6: Schematic of Sample for Tensile Test



Figure 4.7a: Sample Mounted on Universal Tensile Machine

4.3.2 Surface Morphology

Since surface roughness of ITO coated substrate is a function of the final device performance, the root mean square surface roughness of the ITO-coated PDMS substrate was measured using atomic force microscopy. A full 10x10 scan was done on each of the surfaces of the ITO on PDMS samples. Surface roughness of each of the layers of organic electronic deposited was also measured using both AFM and Veeco Dektak 150 Surface Profiler.

In an effort to study the damage in the deposited layers of stretchable organics solar cells, the grain structures of the layers were checked under optical microscope. The change in grain structure of each layer was studied under different applied strains: 0%, 20%, 50%, and 70%. The grain structures at 0% refers to the grain structures of

as-fabricated layers. Figure 4.7b is the schematic of the test sample for observing the grain structure of the strained layered structures.

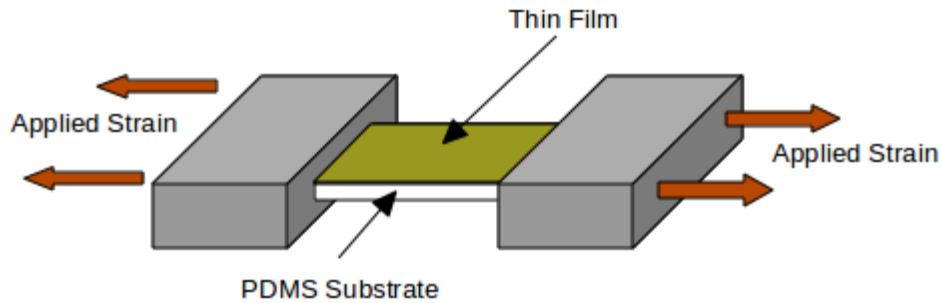


Figure 4.7b: Schematic of Test Sample for Surface Morphology and Optical Transmittance

4.3.3 Optical Characterization

For the optical characterization, the transmittance of each of the samples was measured using Avantes AvaSpec 128 UV-VIS spectrophotometer. The optical transmittance of each of the layers was also taken when strained to 20%, 50%, and 70%

4.4 RESULTS AND DISCUSSION

4.4.1 Stress Analysis

The results of the stress-strain curves of the PDMS substrate samples (A-D) cured at different temperatures and the layers of the stretchable solar cells are shown in Figure 4.8(a-d). The results revealed that the PDMS substrates cured at room temperature has the largest strain with the lowest Young's modulus of 0.0086GPa. The Young's modulus of the PDMS substrates fabricated at temperatures 70°C for 60min, 100°C for 45min, and 125°C for 25min are 0.012GPa, 0.015GPa, and 0.019GPa

respectively. The Young's modulus of PDMS substrates increases with increase in their curing temperature, which invariably reduces their stretchability. By using the model in chapter 3 (equation 3.21), the stresses of all the layers of organic solar cells were computed for each of the applied strains.

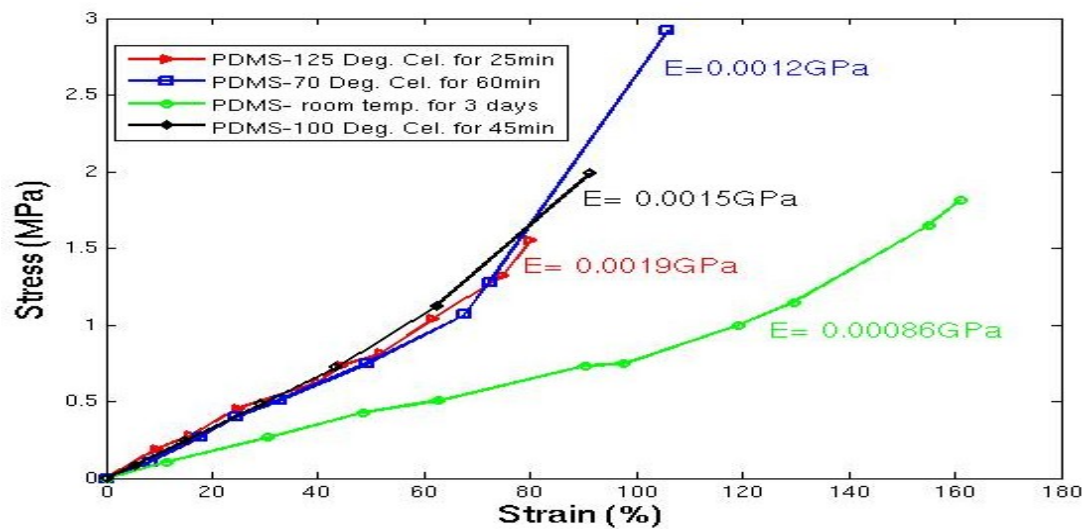


Figure 4.8a: Stress-Strain Curves of PDMS substrates Cured at Different Conditions

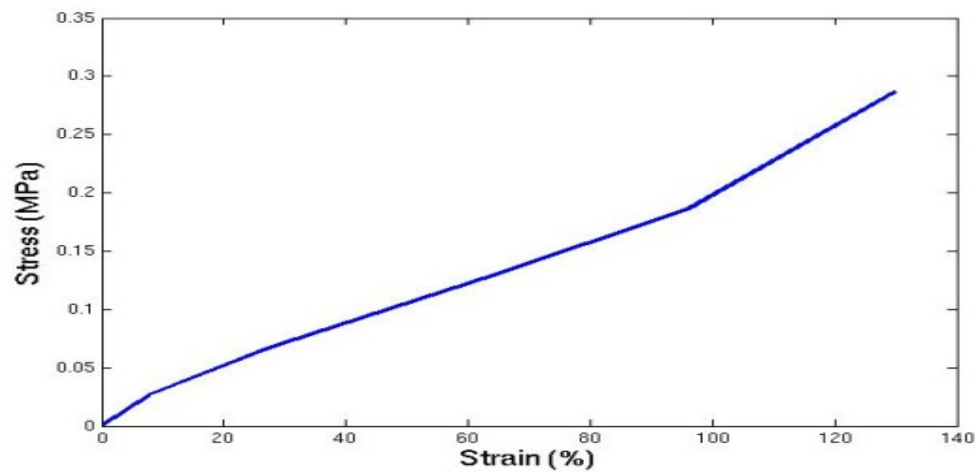


Figure 4.8b: Stress-Strain Curves of ITO layer on PDMS substrate

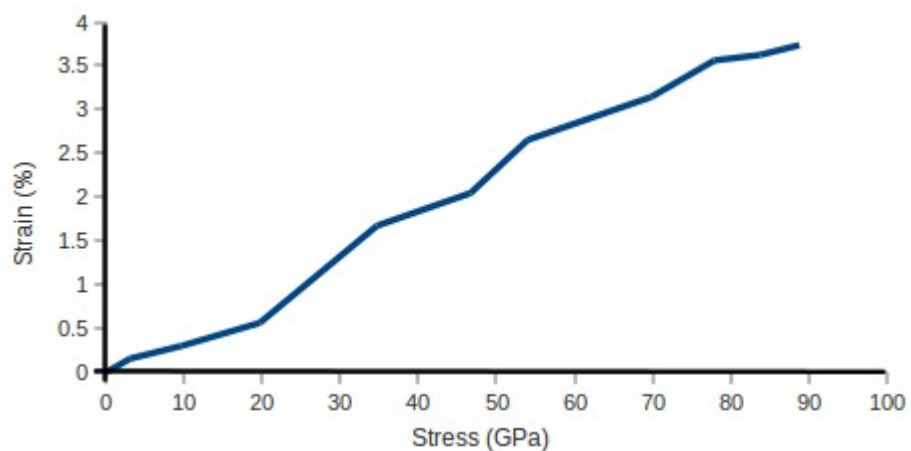


Figure 4.8c: Stress-Strain Curves of PEDOT:PSS layer on ITO coated PDMS substrate

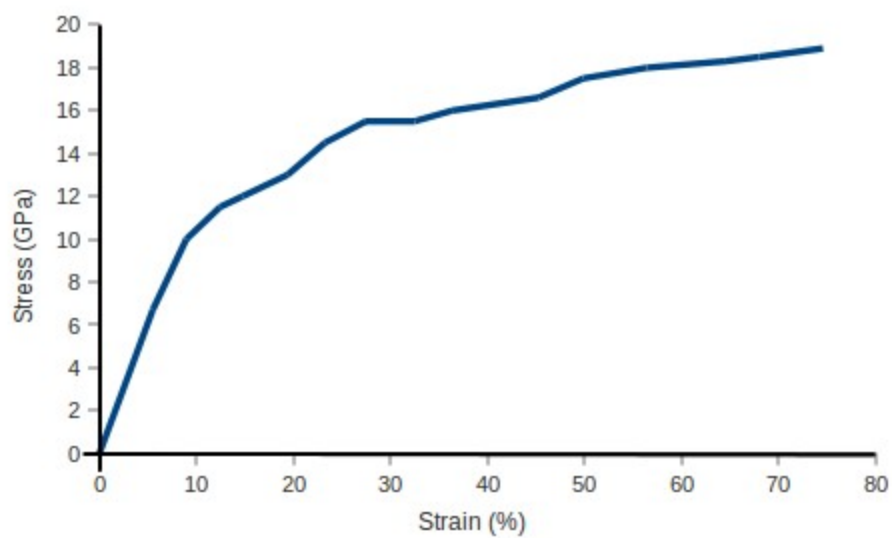


Figure 4.8d: Stress-Strain Curves of P3HT:PCBM Layer on
PEDOT:PSS/ITO coated PDMS Substrate

4.5.2 Optical Properties

The measured optical transmittance of the PDMS substrates fabricated in Aluminium molds was compared to those substrates fabricated in glass molds. The transmittance obtained from PDMS substrates that were cured at different temperatures in Aluminum molds are shown in Figure 4.9a, while those ones in glass molds are shown in Figure 4.9b. The result revealed that the transmittance of PDMS substrates is comparable to those of glass substrates if fabricated in glass molds. This is an interesting result that is relevant to fabrication of flexible organic electronic devices. High transmittance of light through flexible substrates promotes charge transport across the layers of organic electronic structures. Therefore flexible substrates with high transmittance are more relevant in to flexible organic solar cell.

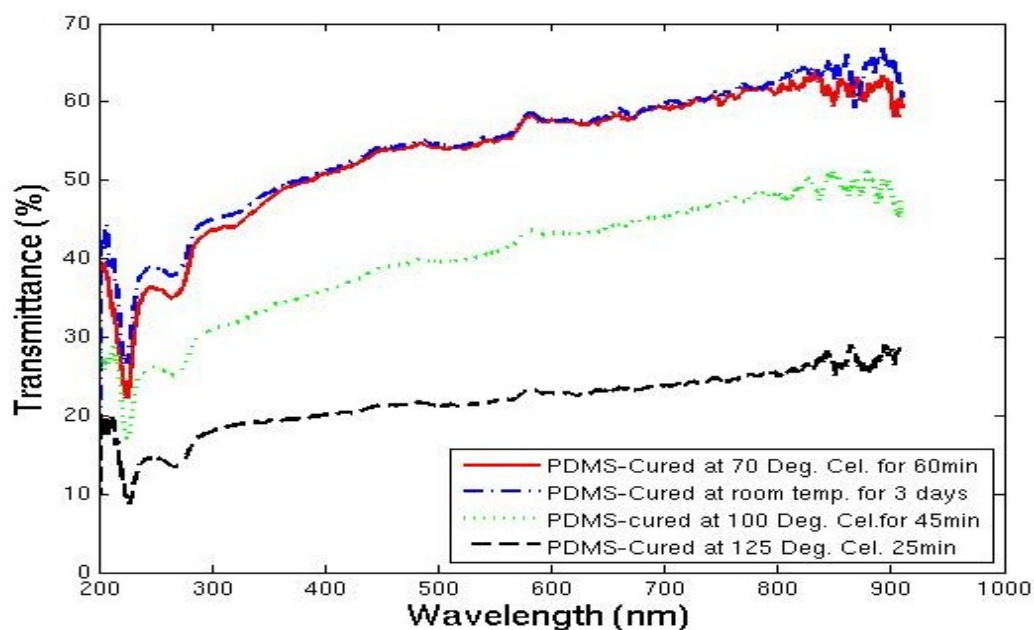


Figure 4.9a: Transmittance of PDMS cured at Various Temperature in Aluminum Mold

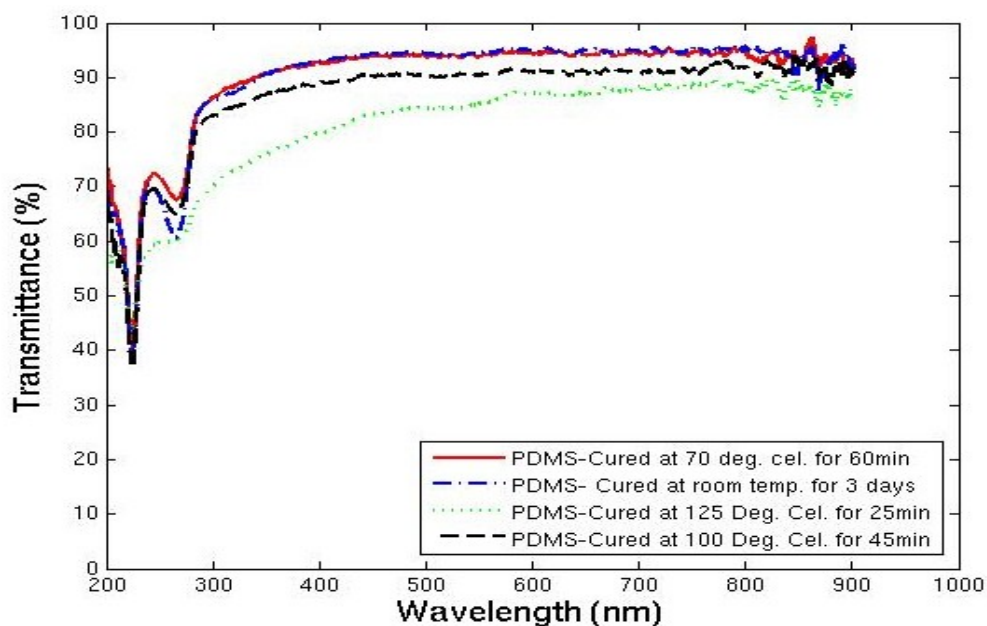


Figure 4.9b: Transmittance of PDMS cured at Various Temperature in Glass Mold

The transmittance of the as-fabricated layers of ITO on PDMS, PEDOT:PSS on ITO-coated PDMS and P3HT:PCBM on PEDOT:PSS/ITO coated PDMS are shown below in Figure 4.10 (a-c). The results is comparable to the transmittance obtained when the layers are deposited on glass substrates. Within the visible spectrum, P3HT:PCBM, PEDOT:PSS, and ITO have transmittance of about 81%, 71%, and 75% respectively.

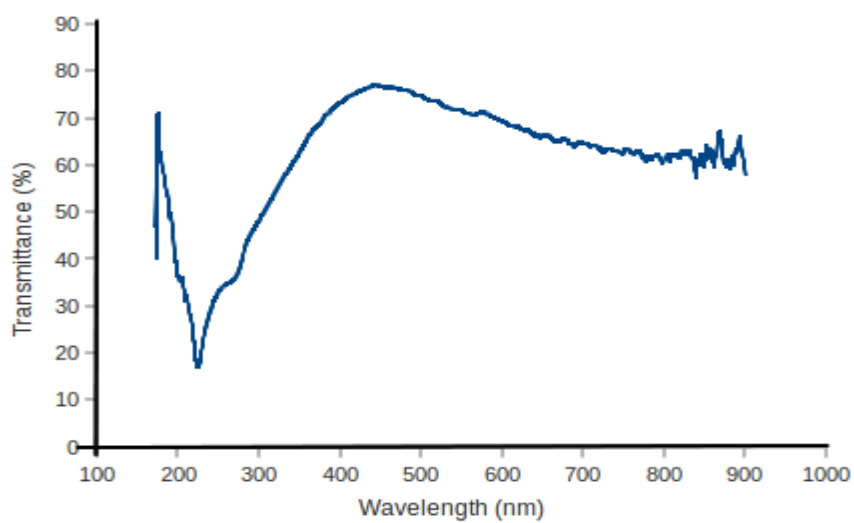


Figure 4.10a: Transmittance of as-fabricated ITO on PDMS substrate.

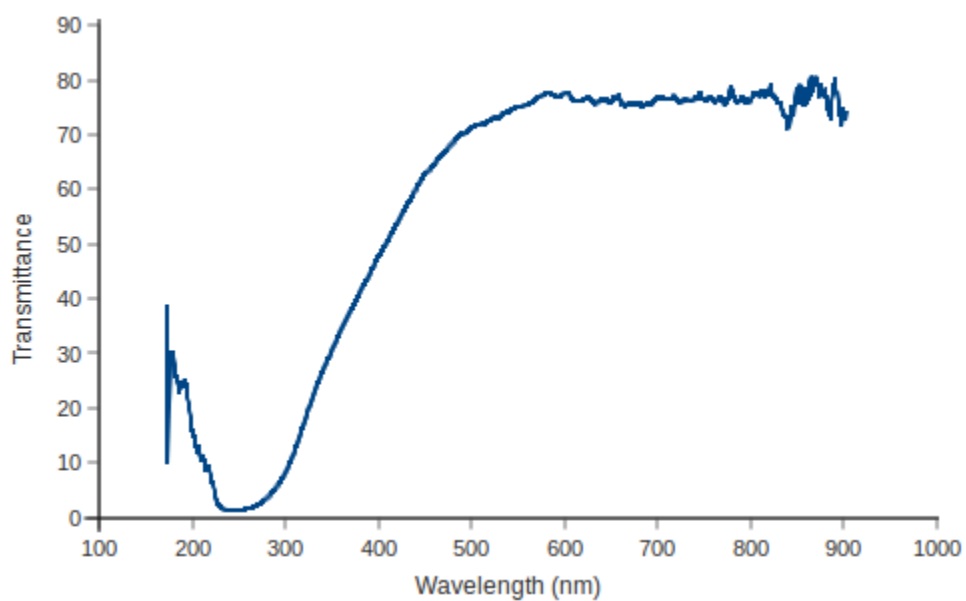


Figure 4.10b: Transmittance of PEDOT:PSS layer on ITO coated PDMS substrate

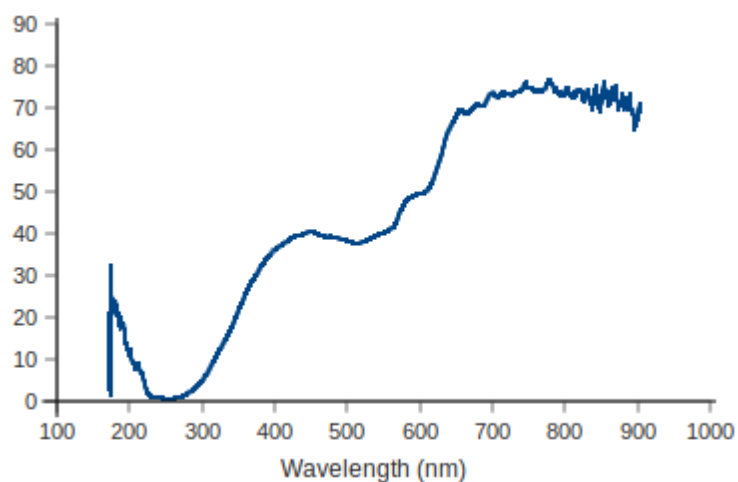


Figure 4.10c: Transmittance of P3HT:PCBM on PEDOT:PSS/ITO-coated PDMS substrate

The transmittances of the as-fabricated layers of the flexible organic solar cell were compared to the stretched layers in which different strains (20%, 50%, and 100%) were applied to the each layer. The change in the transmittance of the are shown below in Figure 4.11(a-c).

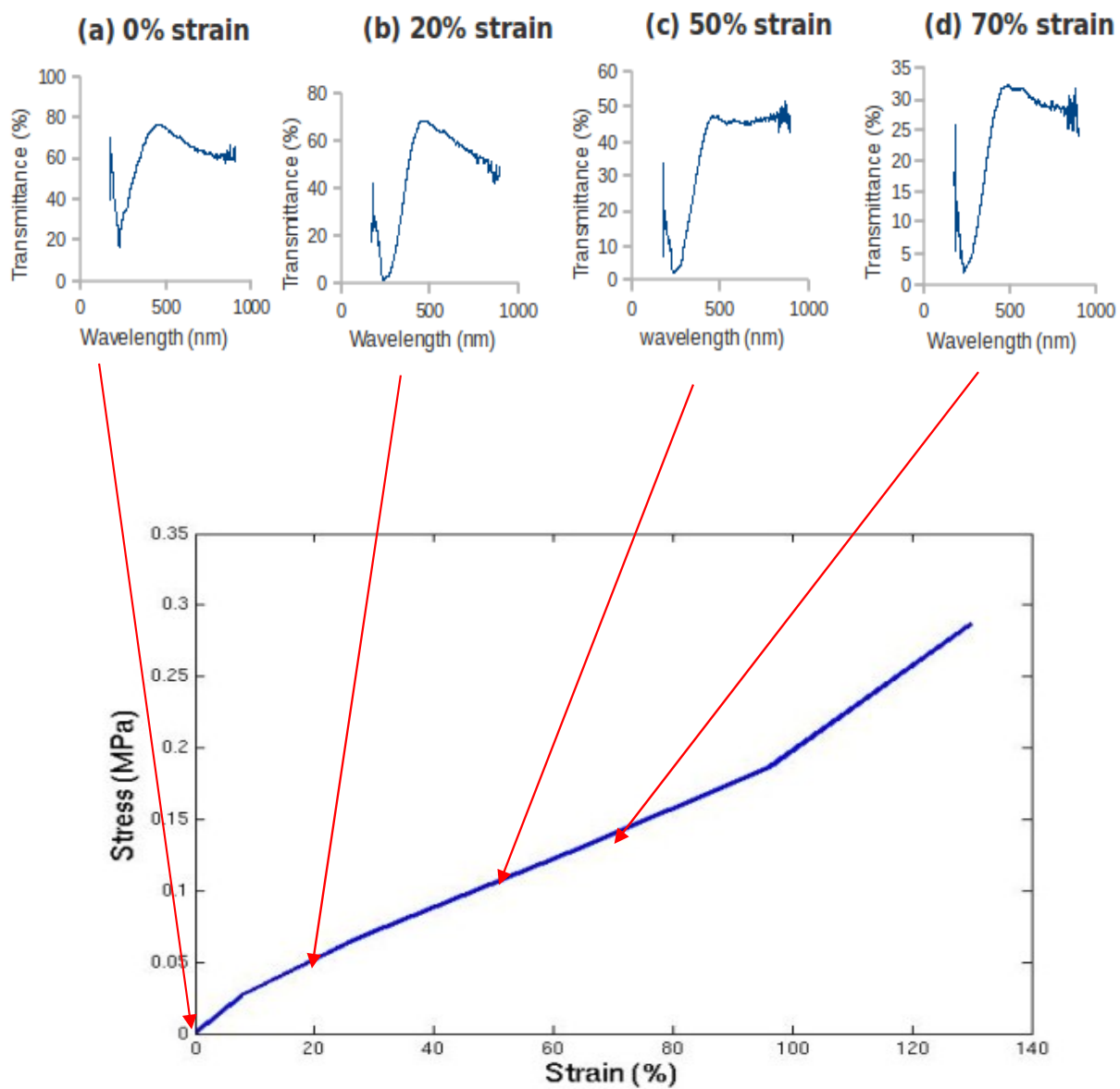


Figure 4.11a: Change in Optical Transmittance of ITO on PDMS

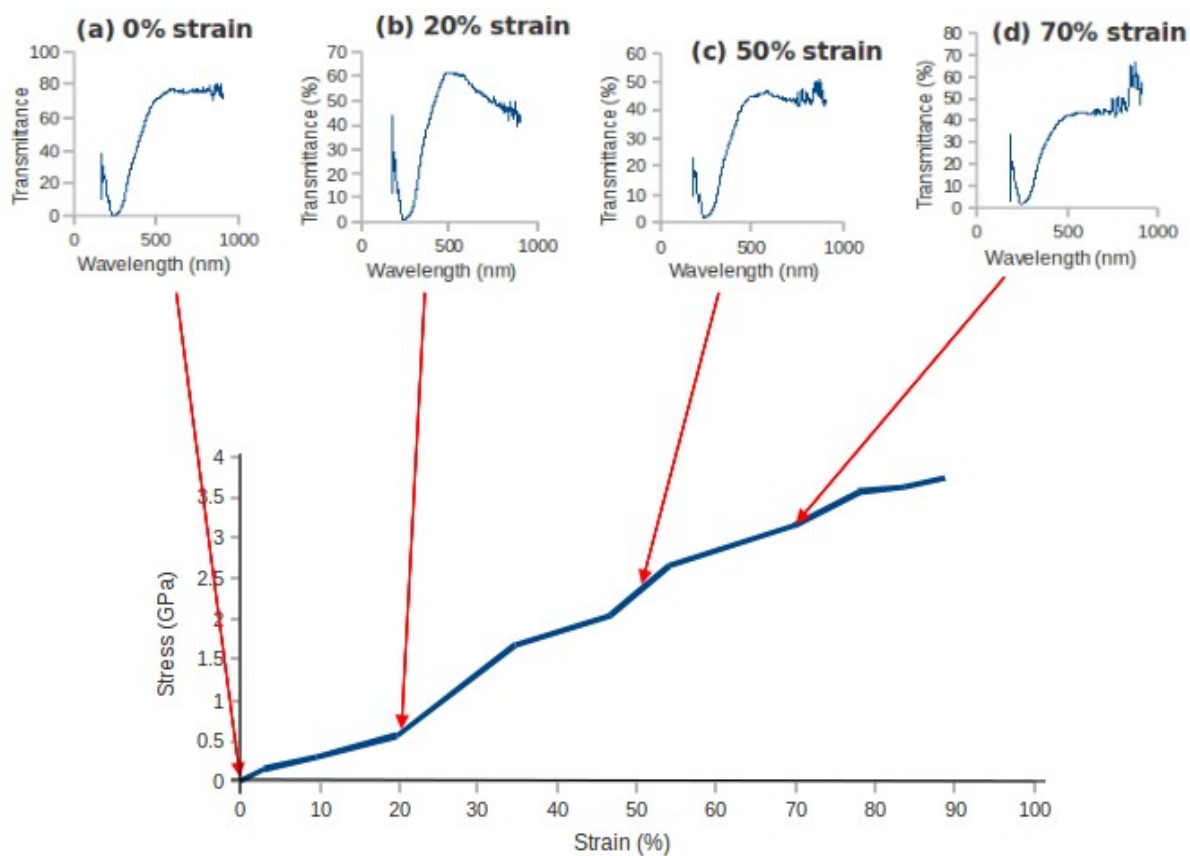


Figure 4.11a: Change in Optical Transmittance of PEDOT:PSS on ITO-coated PDMS`

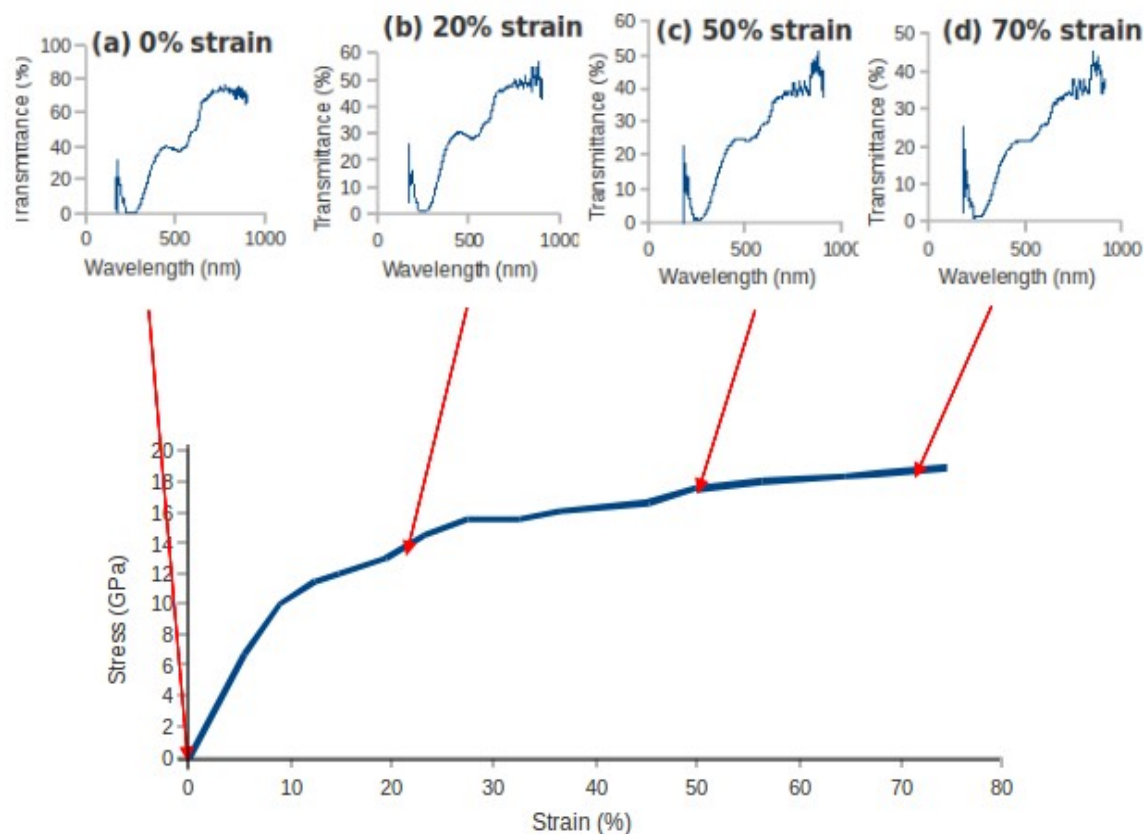


Figure 4.11a: Change in Optical Transmittance of P3HT:PCBM on PEDOT:PSS/ITO/PDMS

4.4.3 Surface Morphology of As-fabricated Layered Structures

The measured root mean squared average surface roughness values of ITO on both glass and each of the PDMS substrates that were cured at different conditions are shown in Table 4.2. The rms roughness values of ITO on PDMS is comparable to that on glass. The obtained rms roughness values for the ITO-coated substrates are within the range of 0.8-9.0nm. The thicknesses of the subsequent layers ranges from 90-150nm. This shows that each of the ITO coated PDMS substrates is considerably smooth and can be used for fabrication stretchable organic electronics, as their rms roughness values

are minimal compared to the subsequent layers to be deposited on them. AFM images of ITO on glass is shown in Figure 4.12a, while the AFM images of ITO on various PDMS substrates are shown in Figure 4.12(b-e).

Table 4.2: Values of rms Roughness of ITO on Various Substrates

ITO on Various PDMS Substrates	Roughness (nm)
ITO on glass substrate (this serves as a control)	4.65
ITO on PDMS (cured at 70°C for 60min)	1.60
ITO on PDMS (cured at 100°C for 45min)	7.93
ITO on PDMS (cured at 125°C for 25min)	0.83
ITO on PDMS (cured at Room. Temp. for 3days)	4.01

Moreover, the measured rms average roughness values of other layers of organic electronics are at nanoscale. The average roughness of PEDOT:PSS is 0.867nm. The AFM image of PEDOT:PSS layer is shown in Figure 4.12f

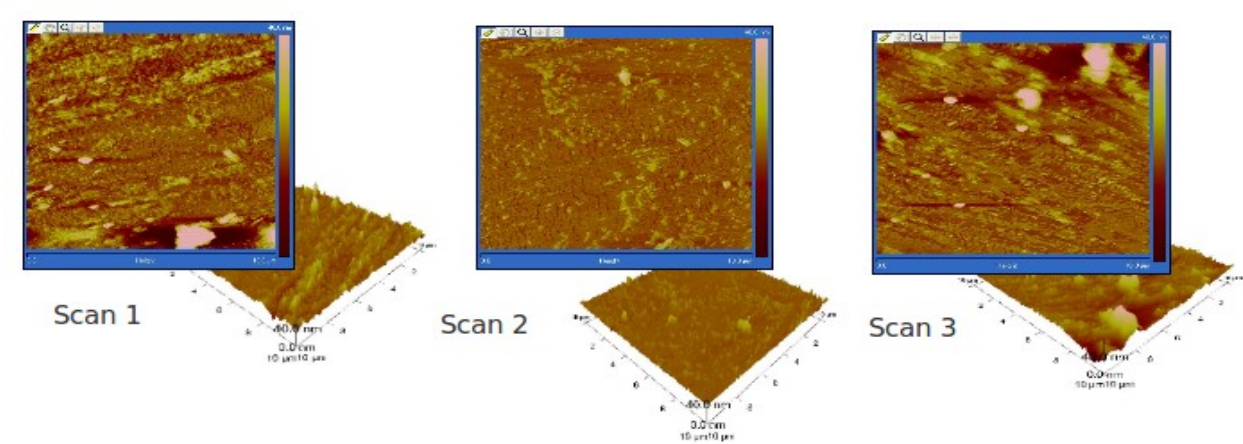


Figure 4.13a: AFM Images of ITO on Regular Glass Substrate

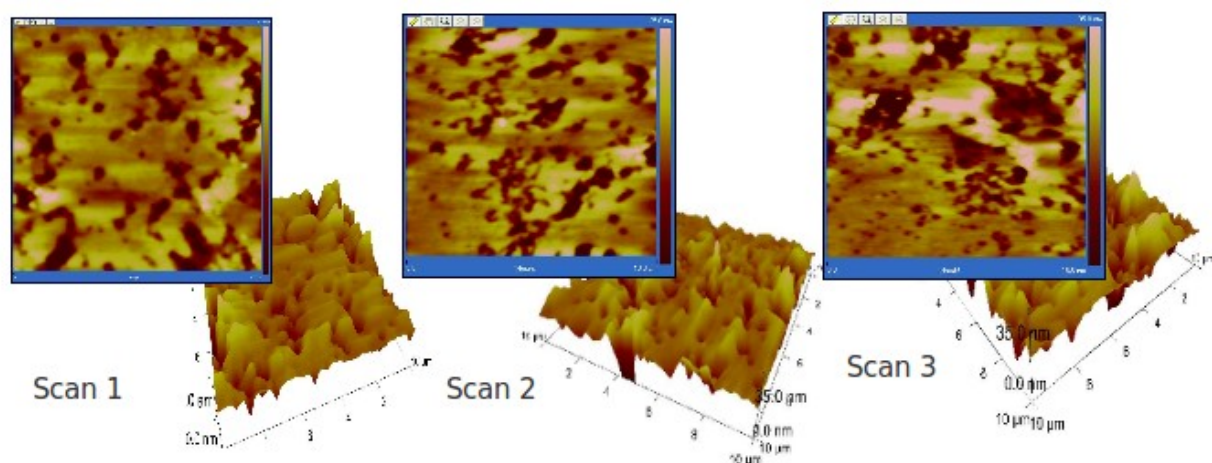


Figure 4.13c: AFM Images of ITO on PDMS (cured at 100°C for 45min)

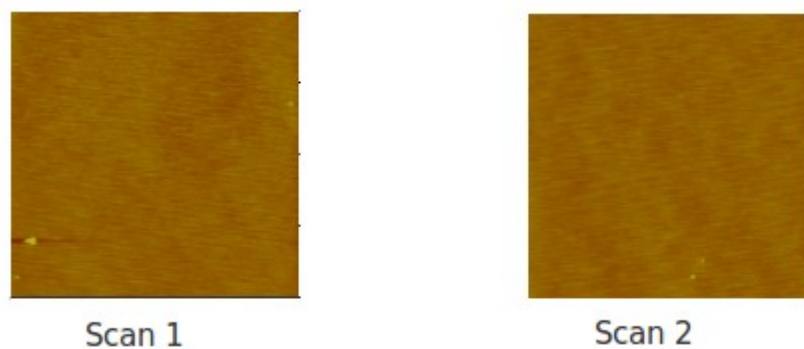


Figure 4.13d: AFM Images of ITO on PDMS (cured at 125°C for 25min)

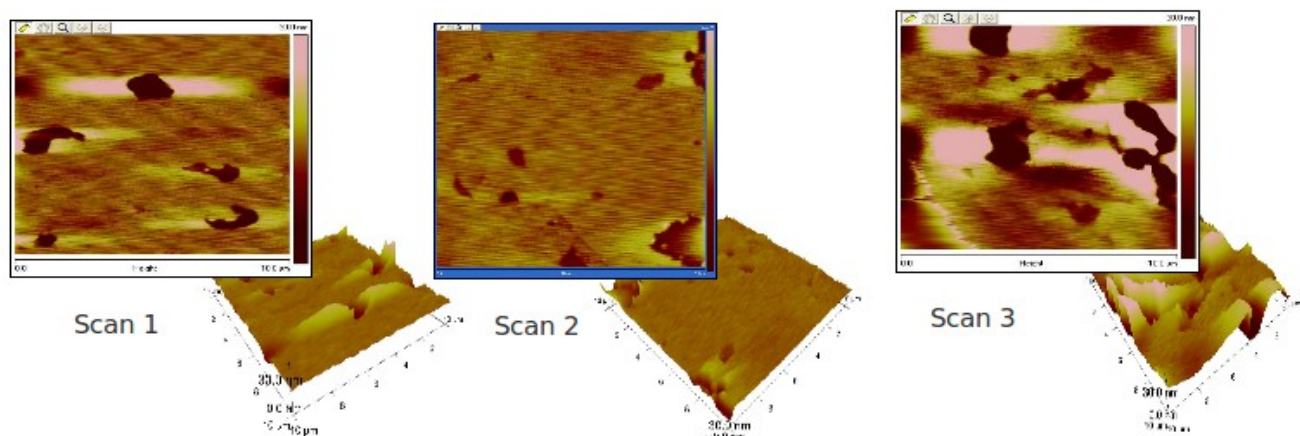


Figure 4.13e: AFM Images of ITO on PDMS (cured at Room Temp. for 3days)

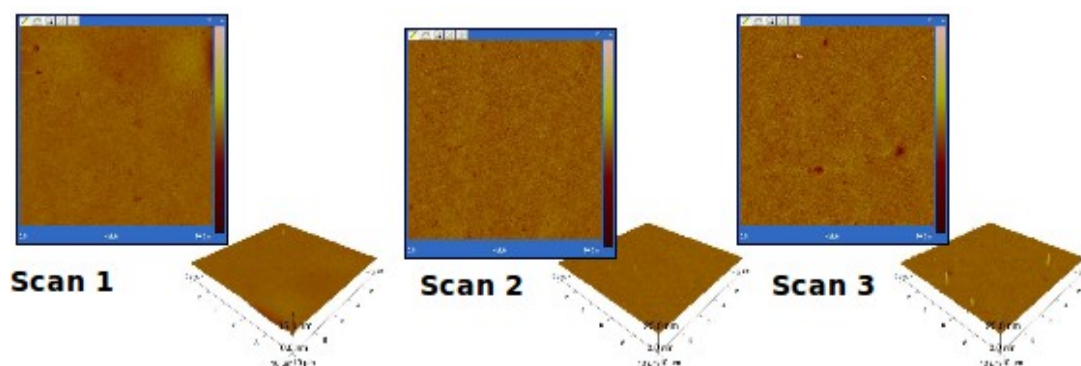


Figure 4.13f: AFM Images of PEDOT:PSS Layer on ITO-coated PDMS

4.4.4 Change in Grain Structures of Layers of The Structures

The observed images of optical microscopy of grains of the layered structures of stretchable organic electronics are shown below in Figure 4.13(a-c). The largest grains are observed at 0% strain. At 0% strain, the layers are referred to as-fabricated layers. The grains reduce in size as the applied strain increases. Grains sizes reduce very fast in ITO layer as the applied strain increases. The result shows that fracture begins to occur first in ITO layer followed by Aluminium cathode before any observable fracture begin to occur in PEDOT:PSS. This confirms the results obtained from finite element simulations in chapter 3 of this thesis. For high performance stretchable organic solar cells, both front and back electrodes need to be optimized. By optimizing the mechanical response of the layers to tensile stress, we can know the threshold of the applied stress before damage begins to occur.

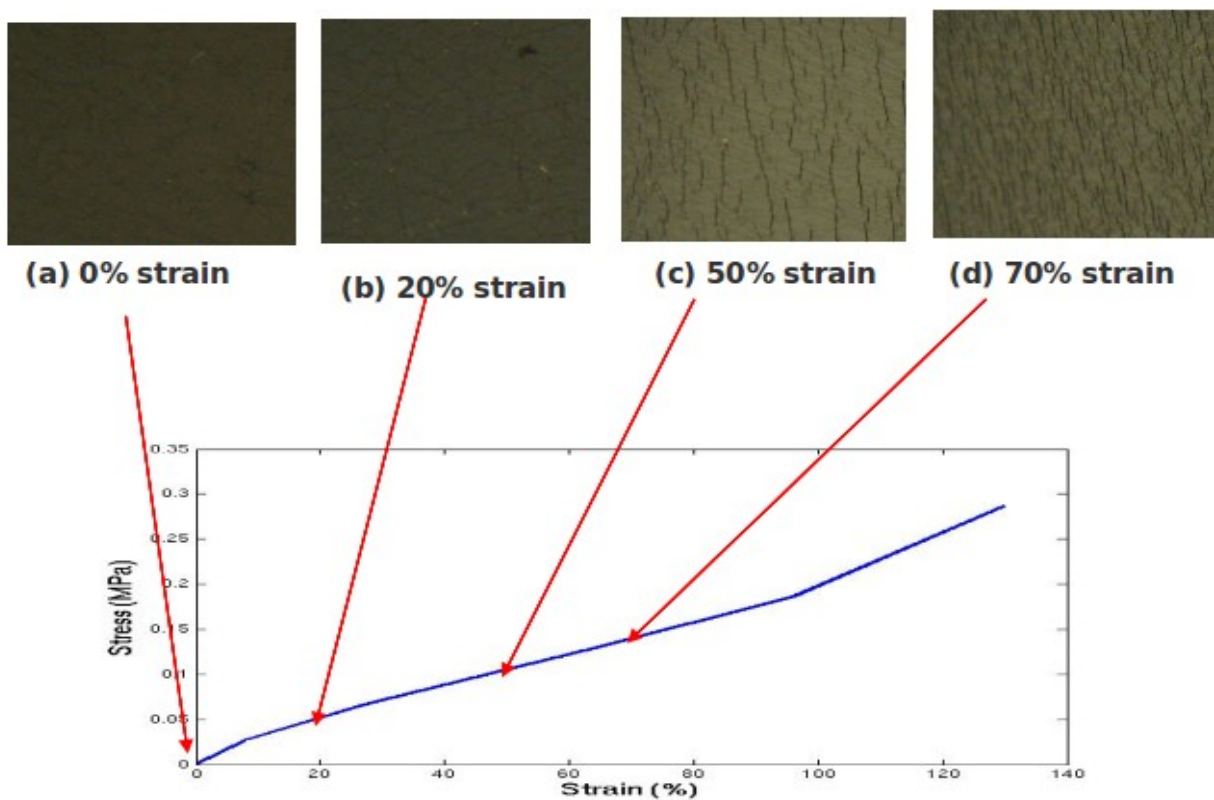


Figure 4.13a: Change in Grain Structure of ITO on PDMS Substrate

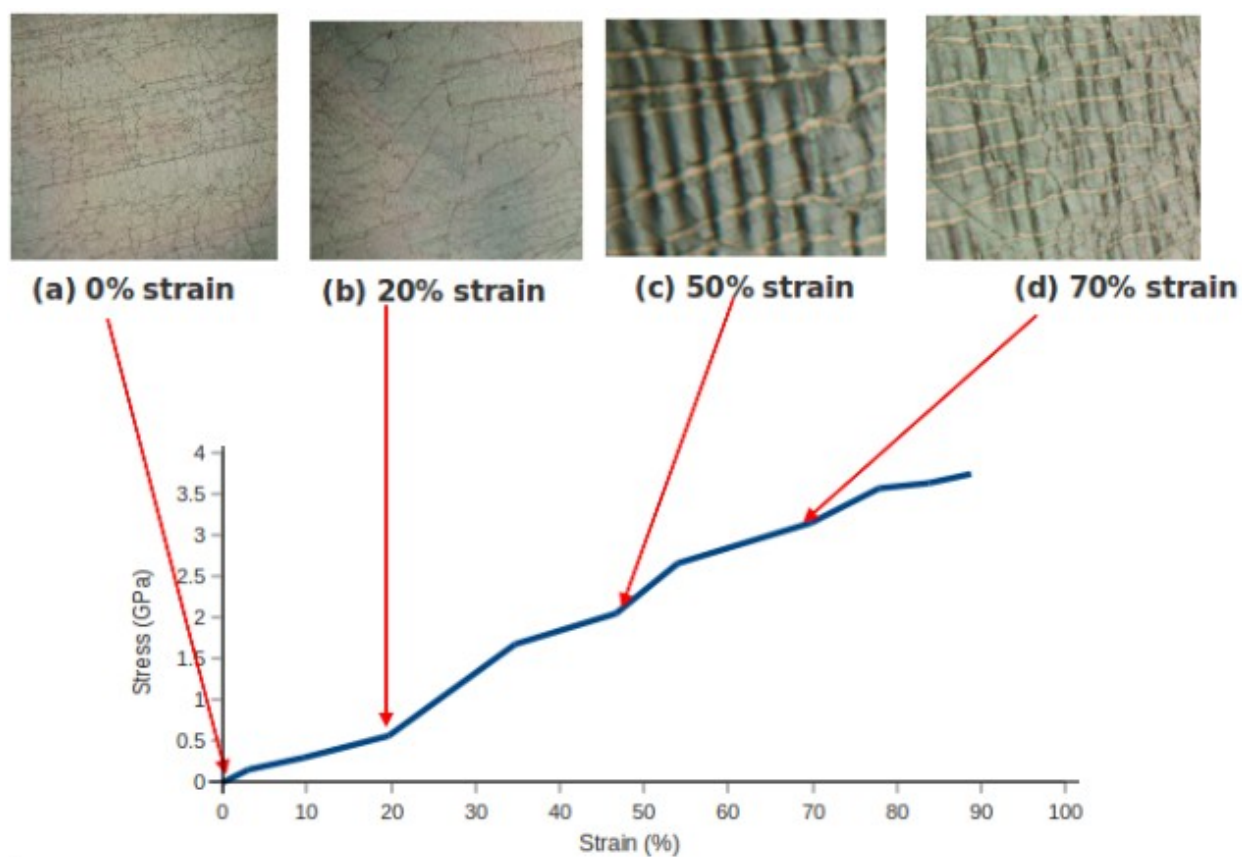


Figure 4.13b: Change in Grain Structure of PEDOT:PSS on ITO-coated PDMS Substrate

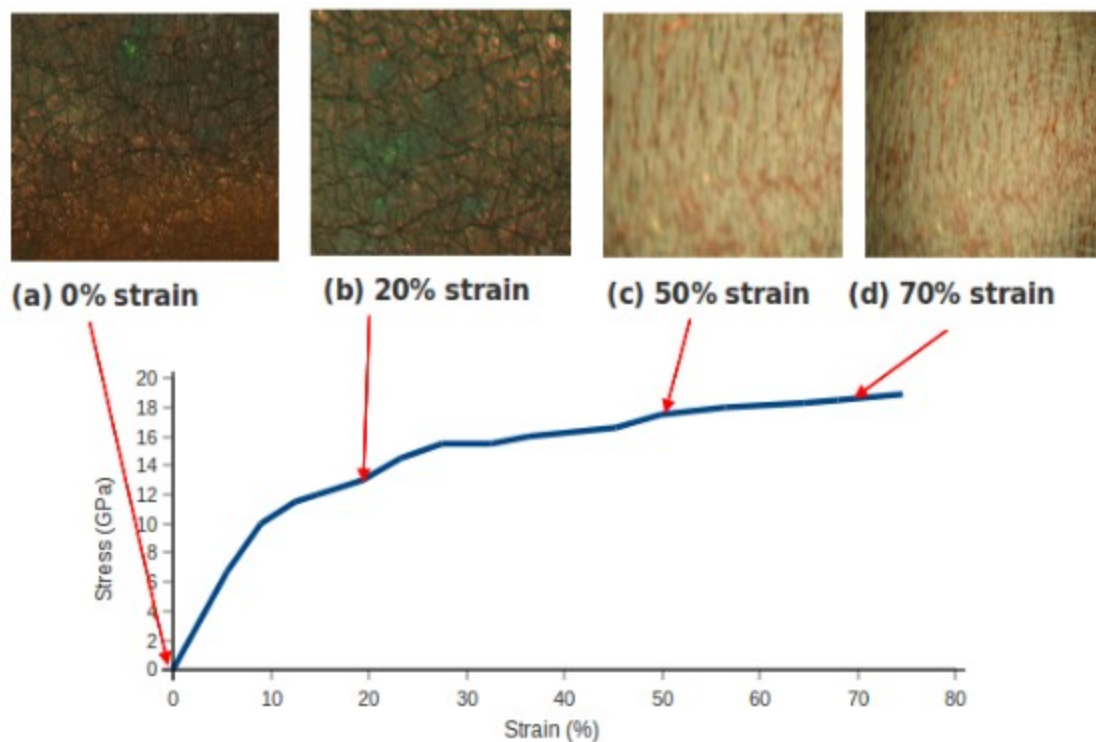


Figure 4.13c: Change in Grain Structure of P3HT:PCBM on PEDOT:PSS/ITO/PDMS

4.4.5 Interfacial Adhesion Forces and Energies

Measured interfacial adhesion forces of the layered structures are presented in Table 4.3. These forces were measured using atomic force microscopy (AFM) as described earlier.

Table 4.3: Comparison of Interfacial Adhesion Forces of The Layered Structures

Interface	Force (nN)
PEDOT:PSS/ITO	7.5
P3HT:PCBM/PEDOT:PSS	187
P3HT:PCBM/Al	50

The interfacial adhesion energies of the layered structure were calculated using equations 3.1 and 3.2 in Chapter 3. The results obtained are presented below in Table 4.4 From the results, P3HT:PCBM/PEDOT:PSS interface has the highest

Table 4.4: Comparison of Interfacial Adhesion Energies of The Layered Structures

Interface	Energy (J/m²)
PEDOT:PSS/ITO	1.4
P3HT:PCBM/PEDOT:PSS	40
P3HT:PCBM/Al	12

interfacial adhesion force and energy of 187nN and 40J/m² respectively. This is followed by P3HT:PCBM/Al, which has force and energy of 50nN and 12J/m² respectively. The strong adhesion force between P3HT:PCBM and PEDOT:PSS promotes charge carrier transport, which will improve the performance of the final device.

CHAPTER 5

CONCLUSION

5.1 Summary and Concluding Remarks

We have studied the responses of optical properties and mechanical failure of flexible organic electronics structures using analytical, numerical, and experimental techniques. To understand how dust particles influence the performance of organic electronics, analytical modelling and finite element simulation of adhesion and contact around dust particles were studied. The analytical modelling shows that the heights of the dust particles reduces the contact lengths and interfacial adhesion of layered structures of flexible organic electronics. The Young's modulus of the layers also reduces the adhesion and contact length of the layered structure. The finite element simulation of contact around dust particles confirmed the results obtained from analytical modelling.

We have achieved optical transmittance of 85-95% for stretchable PDMS substrates that were fabricated in glass molds. This is comparable to the optical transmittance of regular glass substrates. The transmittance of the PDMS substrates fabricated in glass molds is more than the transmittance obtained from PDMS substrates fabricated in Aluminium molds. Based on this study, glass molds are better to fabricate substrates that are relevant to stretchable organic electronics.

Increasing the applied strain reduces the transmittance of the layers of flexible organic electronics structures. There is also a gradual reduction in the grains of the layers as the applied strain increases. The energy release rate increases with increase in the length of the crack propagated across the layers of the structures. Also, the energy release rate is a measure of Young's modulus of the layers. A layer with the lowest Young's modulus has the highest energy release rate.

Finally, the interfacial adhesion force and energy between the active and the hole-injection layers (P3HT:PCBM/PEDOT:PSS) are higher compared to other layers of the structures.

5.2 Future Work

We strongly recommend that further study should be carried out on the effects of stretching on electrical properties of the layers of stretchable organic electronics. We also encourage that working device of stretchable organic solar cells should be fabricated.